

CO Emission and Absorption-line Survey of the M87 Nucleus Using Archival ALMA Imaging

BENJAMIN D. BOIZELLE ¹, XUEYI LI ^{2,3}, NICHOLAS LEVAR ¹, SAM NORCROSS ¹, BENJAMIN J. DERIEG ^{1,4},
JARED R. DAVIDSON ¹, KAVIN SIAW ⁵ AND JONELLE L. WALSH ⁶

¹Department of Physics and Astronomy, N284 ESC, Brigham Young University, Provo, UT, 84602, USA

²Department of Physics & Astronomy, Macalester College, 1600 Grand Avenue, Saint Paul, MN 55105, USA

³Department of Physics and Astronomy, University of Delaware, 104 The Green Newark, DE, 19716, USA

⁴Department of Physics and Astronomy, 201 James Fletcher Bldg. University of Utah, Salt Lake City, UT, 84112, USA

⁵Department of Physics, 10 East 2nd South, ROM 118, Brigham Young University – Idaho, Rexburg, ID, 83460, USA

⁶George P. and Cynthia Woods Mitchell Institute for Fundamental Physics and Astronomy, 4242 TAMU, Texas A&M University, College Station, TX, 77843-4242, USA

ABSTRACT

We present an M87 molecular line search from archival Atacama Large Millimeter/sub-millimeter Array (ALMA) imaging, covering the circumnuclear disk (CND) as well as ionized gas filaments and dusty cloud regions. We find no evidence for CO emission in the central \sim kpc and place an upper limit of $M_{\text{H}_2} < 2.3 \times 10^5 M_{\odot}$ in the atomic gas CND, a factor of $20\times$ lower than previous surveys. During this search, we discovered extragalactic CO absorption lines in the $J = 1-0$, $2-1$, and $3-2$ transitions against the bright (Jy-scale) active nucleus. These CO lines are narrow ($\sim 5 \text{ km s}^{-1}$) and blueshifted with respect to the galaxy's systemic velocity by -75 to -84 km s^{-1} . This CO absorber appears to be kinematically distinct from outflowing atomic gas seen in absorption. Assuming a diffuse molecular phase, low integrated opacities ranging from $\tau_{\text{CO}} \sim 0.02 - 0.06$ and column density $N_{\text{CO}} = 1.16 \times 10^{15} \text{ cm}^{-2}$ translate to $N_{\text{H}_2} \sim (1 - 2) \times 10^{20} \text{ cm}^{-2}$. CO excitation temperatures spanning $T_{\text{ex}} \sim 8 \text{ K}$ to $\sim 30 \text{ K}$ do not follow local thermodynamic equilibrium (LTE) expectations, and non-LTE *radex* radiative transfer modeling suggests the CO absorber has a number density $n_{\text{H}_2} \sim 5000 \text{ cm}^{-3}$. Taken together, the observed CO absorption lines are most consistent with a thin, pressure-confined filament seen slightly off-center from the M87 nucleus. We also use these ALMA data to explore the impact of residual telluric lines and atmospheric variability on the identification and classification of narrow extragalactic lines. Additionally, we demonstrate how bandpass calibration limitations may introduce broad but very low S/N absorption and emission signatures near such a bright continuum source.

Keywords: Active Galactic Nuclei (16) — Galaxy Nuclei (609) — Interstellar Medium (847) — Quasar Absorption Line Spectroscopy (1317) — AGN Host Galaxies (2017) — Radio Active Galactic Nuclei (2134)

1. INTRODUCTION

Ongoing gas accretion onto supermassive black holes (BHs; with masses $M_{\text{BH}} \sim 10^5 - 10^{10} M_{\odot}$) powers active galactic nuclei (AGN) at the centers of galaxies. In extreme cases, highly efficient central engines are visible across the observable universe. A wide range of AGN phenomena – including broad and/or narrow emission lines, a very hot accretion disk, and large-scale jets of relativistic plasma – are explained in the AGN standard model primarily by different viewing angles and accretion rates (e.g., C. Tadhunter 2008; J. R. Trump et al. 2011; S. Bianchi et al. 2012). A subset of these AGN are radio bright with collimated jet features, typically classified as either type I (centrally dominant or edge-darkened continuum emission) or type II (edge-brightened Fanaroff-Riley galaxies (FR; B. L. Fanaroff & J. M. Riley 1974).

M87 (NGC 4486) is one of the most well-studied luminous early-type galaxies (ETGs; classified as cD0-1 pec; G. de Vaucouleurs et al. 1991), in large part due to its close proximity in the Virgo cluster and as the brightest galaxy of the Virgo A subgroup. This FR I galaxy is also well studied due to its central narrow-lined, low-ionized nuclear emission-line region (LINER Type 2; L. C. Ho et al. 1997; M. A. Dopita et al. 1997). The active nucleus is bright across mm to radio wavelengths (with central flux density $S_{\nu} \gtrsim 1 \text{ Jy}$) and launches a jet seen primarily on the approaching side across radio to X-ray wavelengths (e.g., H. L. Marshall et al. 2002; J. Y. Kim et al. 2018), connecting to radio lobes that extend out to a projected $\sim 3 \text{ kpc}$ (M. Chiaberge et al. 1999). M87 garnered significant additional attention during the Event Horizon Telescope (EHT) very large baseline interferometry (VLBI) campaigns that imaged its BH shadow on $\sim 25 \mu\text{as}$ scales and connected gas accretion and magnetic

field structures very close to the BH to the jet launching region (EHT Collaboration et al. 2019, 2021a,b).

Modeling of both the EHT and stellar kinematics return a consistent \dot{M}_{BH} ranging between $(5.4-6.5) \times 10^9 M_{\odot}$ (K. Gebhardt & J. Thomas 2009; EHT Collaboration et al. 2019; E. R. Liepold et al. 2023; D. A. Simon et al. 2024). Earlier gas-dynamical modeling efforts had preferred a BH mass that was half that of stellar-dynamical modeling results (R. J. Harms et al. 1994; F. Macchetto et al. 1997; J. L. Walsh et al. 2013); recent work, however, has brought the gaseous results into better agreement (J. Osorno et al. 2023). The mass accretion rate of M87 is very low, between $\dot{M}_{\text{BH}} < 10^{-3} - 10^{-2} M_{\odot} \text{ yr}^{-1}$ or an Eddington fraction $\dot{M}_{\text{BH}}/\dot{M}_{\text{Edd}} \lesssim 1.5 \times 10^{-4} - 1.5 \times 10^{-3}$ (C. Y. Kuo et al. 2014; K. Inayoshi et al. 2020). Together with many other radio galaxies, M87 lies in a transition region between cold, thin disk accretion and radiatively inefficient accretion flows.

Early ground-based and Hubble Space Telescope (HST) imaging revealed filaments of ionized gas extending out several kpc from the M87 nucleus (W. B. Sparks et al. 1993; H. C. Ford et al. 1994; R. W. Pogge et al. 2000). It is unclear if this gas is related to known merger activity (A. Longobardi et al. 2015), or even if the gas in the central few kpc is infalling towards the BH (e.g., in chaotic cold-mode accretion, or CCA; M. Gaspari et al. 2013) or is being disturbed by rising bubbles or the radio jet (e.g., V. Olivares et al. 2019). In some massive elliptical or cD galaxies like M87, spectral energy distribution (SED) fitting (F. Yuan & R. Narayan 2014) suggests hot-mode accretion dominates most of the time, even if a gaseous circumnuclear disk (CND) is clearly detected.

Many FR I galaxies host morphologically regular, geometrically thin disks with relatively small radii (generally a few $\times 100$ pc; S. de Koff et al. 2000; L. Saripalli 2012). These CNDs are often identified by dusty disks or lanes, and molecular line surveys have revealed modest cospatial H_2 mass reservoirs (with typical $M_{\text{H}_2} \sim 10^7 - 10^8 M_{\odot}$; e.g., B. Ocaña Flaquer et al. 2010; I. Prandoni et al. 2010; B. D. Boizelle et al. 2017, 2021; I. Ruffa et al. 2019). Unfortunately, the bright optical nucleus and jet of M87 prevent any definitive conclusions about dust absorption on the smallest scales (down to a projected radius $R \sim 0''.1$ or ~ 10 pc from the galaxy center). On larger scales, its filamentary gas appears to connect to an ionized-gas CND with well-ordered rotation out to $R \sim 0''.5$ (< 50 pc; W. B. Sparks et al. 1993; H. C. Ford et al. 1994; J. L. Walsh et al. 2013; A. Boselli et al. 2019; J. Osorno et al. 2023). Atomic gas line-of-sight (LOS) speeds (v_{LOS}) for this rotation reach roughly $\pm 500 \text{ km s}^{-1}$ from the galaxy's systemic velocity $v_{\text{sys}} \equiv cz_{\text{obs}} = 1284 \pm 5 \text{ km s}^{-1}$ (from stellar absorption-line fits with a heliocentric $z_{\text{obs}} = 0.004283$; M. Cappellari et al. 2011) within an angular distance of $R \lesssim 0''.1$ from the nucleus.

Despite the mostly ordered central velocity field, maps of the atomic emission-line dispersion σ_{LOS} show asymmetries in the northwest direction that suggest a bi-conical outflow (with intrinsic speeds reaching out to $\sim 400 \text{ km s}^{-1}$ along a position angle $\text{PA} \sim -45^\circ$; W. B. Sparks et al. 1993; A.

Boselli et al. 2019; J. Osorno et al. 2023). Further support for an outflow comes from UV/optical absorption lines detected against the bright nucleus, although this may reveal a kinematically distinct component. These atomic tracers show blueshifted absorption lines with $v_{\text{LOS}} - v_{\text{sys}} \sim -131 \pm 19 \text{ km s}^{-1}$ and moderate intrinsic FWHM $\lesssim 300 \text{ km s}^{-1}$ (Z. I. Tsvetanov et al. 1999b; B. M. Sabra et al. 2003). Absorption-line measurements as well as modeling of the central X-ray spectrum both support hydrogen column densities in the $N_{\text{H}} \sim 10^{19} - 10^{20} \text{ cm}^{-2}$ range (A. S. Wilson & Y. Yang 2002; T. Di Matteo et al. 2003; B. M. Sabra et al. 2003).

Within the central few kpc of M87 (out to at least $\sim 40''$), molecular gas is best traced in the optical by discrete, low-extinction filaments and clouds. Similar dusty features are observed in the inner $\sim \text{kpc}$ of most luminous elliptical galaxies (W. G. Mathews & F. Brighenti 2003; P. Temi et al. 2018; G. R. Tremblay et al. 2018; V. Olivares et al. 2019), often following ionized atomic emission-line filaments (e.g., W. B. Sparks et al. 1993; L. Ferrarese et al. 2006; J. P. Madrid et al. 2007; A. Boselli et al. 2019; T. R. Taylor et al. 2020). For M87, evidence for the corresponding thermal dust continuum is ambiguous and global SED fits are often interpreted as showing no evidence for diffuse dust and limited support for circumnuclear dust (M. Baes et al. 2010). However, a couple of elevated SED points have been tied to a small, cold dust component (with characteristic temperature $T_{\text{dust}} \sim 35 \text{ K}$ and mass $M_{\text{dust}} \sim 6 \times 10^4 M_{\odot}$; H. S. P. Müller et al. 2005). Also, mid-IR spectroscopy of the nucleus is better fit with the addition of a warmer low-mass dust component ($T_{\text{dust}} \sim 45 - 65 \text{ K}$ and $M_{\text{dust}} < 200 M_{\odot}$; E. S. Perlman et al. 2007).

The expected, accompanying molecular gas remains elusive. Single-dish mm/sub-mm imaging of this target did not detect global ^{12}CO (hereafter CO) emission in the $J = 1 - 0$ transition across a velocity range of a few hundred km s^{-1} , first with an initial 1σ line flux upper limit $S_{\text{CO}(1-0)}\Delta\nu < 20 \text{ Jy km s}^{-1}$ (J. H. Bieging et al. 1981; W. Jaffe 1987; J. Braine & T. Wiklind 1993) and later on a 3σ upper limit of $10.2 \text{ Jy km s}^{-1}$ (F. Combes et al. 2007; P. Salomé & F. Combes 2008). From interferometric observations with the Submillimeter Array (SMA), J. C. Tan et al. (2008) reported a tentative $S_{\text{CO}(2-1)}\Delta\nu \approx 8.8 \pm 2.2(\text{stat}) \pm 1.8(\text{sys}) \text{ Jy km s}^{-1}$ detection (with separate 1σ statistical and systematic uncertainties) in an ~ 80 pc-diameter aperture about the nucleus. If correct, the corresponding total H_2 mass $M_{\text{H}_2} \lesssim 5 \times 10^6 M_{\odot}$ could be detected using the Atacama Large Millimeter/submillimeter Array (ALMA), which provides an order-of-magnitude improvement in both angular resolution and limiting sensitivity over previous mm-wavelength interferometers.

In this paper, we present the first ALMA mm/sub-mm wavelength molecular line search of the M87 nucleus. This paper is structured as follows. In Section 2, we introduce archival HST and ALMA data sets and imaging processes. Section 3 describes the CO emission-line search and CO absorption-line detection. We constrain molecular gas properties in Section 4 and conclude in Section 5. In the extensive appendices, we provide more in-depth analysis concerning extragalactic spectral line identification with ALMA,

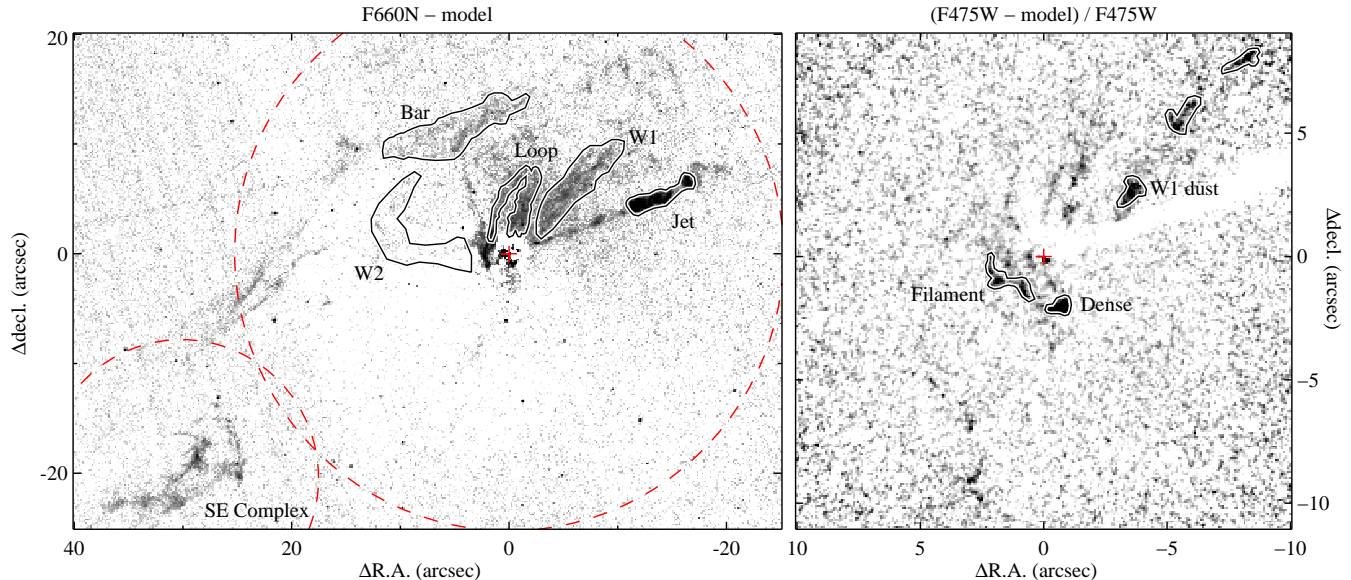


Figure 1. HST imaging of M87 after subtracting a stellar continuum model. Narrowband residual data (*left panel*) reveal $H\alpha+[N II]$ emission-line filaments above the low pattern noise that are centered on the nucleus (labelled with a +) and stretch out a few kpc. The most extended ALMA 12-m field of view (FoV) for imaging centered on the nucleus (half-power beam width HPBW $\sim 50''$ in Band 3) and the FoV covering the southeast complex (HPBW $\sim 25''$ in Band 6; A. Simionescu et al. 2018) are overlain (dashed circles). Broadband fractional difference data (*right*) reveal dusty clumps and filaments. In the emission-line filament region W1, dust is identified in three main clumps. Outlined regions shown here isolate the most obvious atomic gas emission or dust obscuration and are used in CO emission-line searches.

including the impact of atmospheric (ozone) variability and the possibility of spurious broad line detection due to band-pass calibration limitations.

Throughout, we assume a standard Λ CDM cosmology with $H_0 = 67.8 \text{ km s}^{-1} \text{ Mpc}^{-1}$ along with $\Omega_m = 0.308$ and $\Omega_\Lambda = 0.692$ (Planck Collaboration et al. 2016). We adopt a distance modulus $m-M = 31.11 \pm 0.08 \text{ mag}$ for M87 from surface brightness fluctuation methods (corresponding to a luminosity distance $D_L \sim 16.7 \pm 0.6 \text{ Mpc}$; J. P. Blakeslee et al. 2009). After correcting the observed redshift $z_{\text{obs}} = 0.004283$ for infall towards the Virgo cluster ($z_{\text{corr}} \sim 0.0032$; J. R. Mould et al. 2000), this results in an angular size scale of $80.5 \text{ pc arcsec}^{-1}$. When comparing to the literature, we corrected measurements (or upper limits) to this D_L . We employed the optical velocity definition and referenced kinematic quantities in the barycentric frame by default.

2. DATA

2.1. Optical Imaging

To create integration regions for this ALMA CO line search, we employed pipeline-calibrated HST images retrieved from the Mikulski Archive for Space Telescopes (DOI: [10.17909/wmbg-9051](https://doi.org/10.17909/wmbg-9051)). To isolate dust features, we used drizzled Wide Field Camera 3 (WFC3/UVIS; L. Dreschel 2022) F475W imaging from program GO-14256 (PI: Biretta). To map out filamentary $H\alpha+[N II]$ emission, we used a series of Advanced Camera for Surveys (ACS; J. E. Ryon 2022) F660N polarized images from program GO-

12271 (PI: Sparks) that we aligned before combining into a single Stokes I image. In each case, we modeled and subtracted the stellar continuum using a concentric Multi-Gaussian Expansion (MGE; E. Emsellem et al. 1994) using GALFIT (C. Y. Peng et al. 2002). Following J. R. Davidson et al. (2024), we iteratively expanded a pixel mask containing non-stellar features (gas and dust, the optical jet, and central AGN) to avoid contaminating the stellar fit. Figure 1 shows the final gas emission and dust absorption maps. In Section 3.1, we describe the regions created for the CO emission-line search.

2.2. Archival ALMA Imaging

We obtained archival ALMA 12-m imaging from eleven single-pointing data sets taken between 2013 December 1 and 2018 September 25 whose phase centers coincided with the M87 nucleus (see Appendix A and Table A1 for additional details). In this nearly five-year window, one semi-pass program (2016.1.000415.S; PI: Marti-Vidal) was not included due to pipeline calibration difficulties arising from changing polarization calibrators between Execution Blocks (EBs; for the continuum analysis, see C. Goddi et al. 2021). Another program (2013.1.00862.S; PI: Simionescu) was centered $\sim 40''$ south-east of the nucleus to image CO(2–1) in a dust and gas complex (hereafter the SE cloud; A. Simionescu et al. 2018), and the field of view does not cover the M87 nucleus.

We also retrieved and analyzed ALMA Compact Array (ACA) 7-m observations in programs 2019.1.00807.S and 2021.1.01398.S. Due to large average FWHM of the syn-

thesized beam $\bar{\theta}_{\text{FWHM}} \gtrsim 5''$ and poorer limiting sensitivity compared to the ALMA 12-m data, these 7-m observations are only used for an analysis of the peak SED and to construct a light curve of the bright nucleus. We briefly discuss the ACA data sets, their calibration processes, and results in Appendix B.

2.2.1. ALMA Data Properties

The majority of the programs listed in Table A1 were explicitly designed to probe nuclear continuum properties, although not all of these programs were obtained in time division mode (TDM). These heterogeneous data cover Bands 3, 4, 6, and 7 with θ_{FWHM} ranging from $\sim 0''.03$ to $2''.3$. The chosen spectral setups resulted in spectral resolutions from ~ 1 to 63 MHz (after online Hanning smoothing). Both TDM-only and frequency division mode (FDM) data included dual and full polarization setups. For continuum-focused programs, a few redshifted atomic or molecular transitions (including low- J CO) coincidentally lie within the spectral ranges, albeit at coarse spectral resolution (~ 20 – 100 km s $^{-1}$) at the native binning. Primary spectral windows (spws) for CO-line focused programs typically have velocity resolutions of ~ 1 – 3 km s $^{-1}$. Calibrator observations of M87 were not included due to generally short integrations (10 s to a few min; e.g., see also A. Doi et al. 2013).

2.2.2. Calibration Processes

In general, we applied standard pipeline calibrations to the 12-m data using the appropriate Common Astronomy Software Application (CASA; J. P. McMullin et al. 2007) pipeline version for each data set in order to construct Measurement Sets (MSs). Below, we discuss limited improvements to the standard pipeline calibration processes. Appendix C and E.3 contain additional discussion of the bandpass calibration.

In adjacent or overlapping spws, peak continuum spectra show mismatches at the 1–3% level, which is roughly consistent with relative flux calibration errors (L. Francis et al. 2020a). For projects 2015.1.00030.S and 2016.1.00021.S, these slight discrepancies complicated the uv -plane continuum subtraction for channel ranges with overlapping spws, so we manually re-scaled their flux calibrator `fluxdensity` Stokes I levels in the `setjy` task for individual spws by up to 2% to ensure more continuous flux densities in image-plane spectral cubes. Residual mismatches at the $\sim 0.1\%$ level impacted the search for very broad absorption or emission (see Figure C2 and Appendix E.2).

We applied phase (and usually amplitude) self-calibration with final solution intervals that were per integration (per scan). In two cases, amplitude self-calibration was not adopted when the multi-frequency synthesis (MFS) image peak/rms dynamic range (DR) decreased noticeably compared to the corresponding phase-only products. DRs spanned several hundred up to ~ 9000 and the highest DRs $\gtrsim 5000$ obtained in Band 3 far exceeded the more typical ~ 100 without improved phase solutions (A. M. S. Richards et al.

2022; G. Privon et al. 2024). For certain other ALMA programs with bright continuum sources, higher DRs have been achieved with more careful, per-scan analysis (e.g., S. Kumugi et al. 2022), especially when using brighter bandpass calibrators. The CO data have spectral dynamical ranges (SDRs) that exceed ~ 2000 per native (unbinned) channel in Band 3, although the bandpass stability limit imposes an effective SDR < 1000 limit over large frequency ranges (see Appendix E.3).

Three programs (2016.1.01154.V, 2017.1.00841.V, and 2017.1.00842.V) were obtained as a part of EHT+ALMA VLBI campaigns and most of their MSs coincidentally cover the redshifted CO(2–1) line. From the ALMA archive, the available .V datasets only contain columns and calibration tables pertaining to the phased (APP) observing mode. As is shown in Figure C2, APP-mode spectra show a characteristic scalloping pattern due to sets of 16 native channels (with individual binning $\Delta\nu_{\text{obs}} = 7.81$ MHz) being used for coarse frequency-dependent phase solutions. We adopted the APP-mode results since other projects covered redshifted CO(2–1) and because reconstructing the ALMA interferometric-mode calibration tables is beyond the scope of this archival project (for a guide, see C. Goddi et al. 2019). Without interferometric-mode calibration tables, phase self-calibration is not possible, and the peak (core) flux densities reported in Table A1 are lower by about 30% (EHT MWL Science Working Group et al. 2021, 2024). The scalloping spectral behavior prevents their inclusion in studies of broader line features ($\Delta\nu \gtrsim 50$ km s $^{-1}$), although some .V program data do reveal narrow absorption near redshifted $\nu_{\text{CO}(2-1)}$.

2.2.3. Manual Flagging

For dual polarization data obtained during ALMA Early Science, or for full polarization data when that was still a non-standard observing mode, calibration scripts from the archive often included manual flagging of the science target as well as the flux and bandpass calibrators. We manually flagged a limited number of additional visibilities based on high antenna temperature, amplitude disagreement, and poor bandpass calibration near spw edges. For the MS from member Observing Unit Set A001/X12f/X20f (hereafter X20f and likewise for other member OUS), the pipeline script manually flagged a moderately strong and variable atmospheric line in the bandpass calibrator as extragalactic in origin. This introduced a spurious and deep absorption feature in the peak continuum spectrum of M87 that was coincidentally very close to redshifted $\nu_{\text{CO}(2-1)}$. Removing these manually-flagged channels, re-calibrating the raw visibilities, and re-imaging the MS resulted in more consistent spectral behavior. Appendix D contains more discussion about atmospheric line identification and variability.

2.2.4. MFS and Spectral Imaging

As a part of the self-calibration loops, we imaged each MS into a Stokes I MFS map using Briggs weighting (with robust parameter $r = 0.5$; D. S. Briggs 1995) in the CASA `tclean`

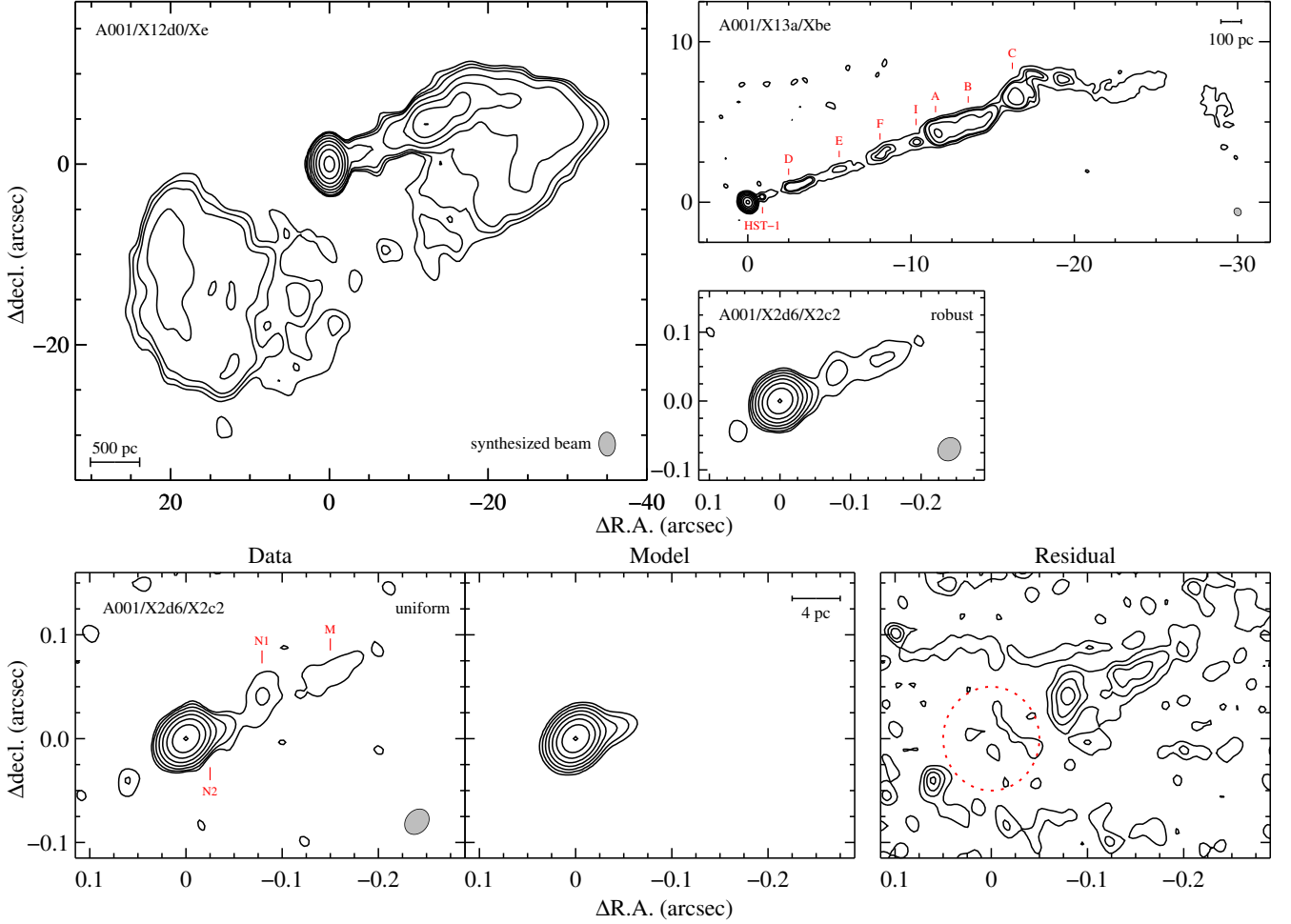


Figure 2. MFS imaging of M87 from ALMA data sets in Band 3 (*top panels*) and Band 6 (*middle right, bottom*) with the corresponding member OUS in each panel. Some of these data sets are sensitive to the large-scale radio jet and lobes spanning a projected 3 kpc while others resolve the jet into individual clumps down to ~ 2 pc from the core. The highest-resolution ALMA imaging is shown alongside a two-component *CASA imfit* model and residual map (*bottom*) that accounts for the central point source and an offset, semi-resolved Gaussian component (observed FWHM $\sim 50 \times 19$ mas) to fit the blended N2 clump. Logarithmically-spaced continuum contours highlight high peak/rms dynamic range (with intensity contours reaching down to a DR ~ 2000) while residual contours at 1, 3, 5, and $7 \times$ rms show no additional continuum features in the central $R < 0''.05$ (~ 4 pc; dashed circle) integration region. The excess feature to the southeast (at $7 \times$ rms) is an imaging artifact and not part of the counter-jet.

deconvolution process. This weighting approach balanced sensitivity and angular resolution considerations. Imaging results are given in Table A1 while Figure 2 shows MFS imaging for a representative sample of this archival project. Additional MFS imaging details and brief continuum analysis are found in Appendices A and B. A more detailed analysis of the nuclear and extended continuum properties is beyond the scope of this paper but is covered in recent ALMA studies of the inner accretion flow and jet behavior (e.g., R.-S. Lu et al. 2023) as well as core and jet polarization (e.g., C. Goddi et al. 2021; EHT Collaboration et al. 2021b,a; EHT MWL Science Working Group et al. 2021). Recent radio interferometric and VLBI studies have revealed detailed jet motion and internal structure (e.g., K. Hada et al. 2016, 2017; K. Hada 2017; A. Pasetto et al. 2021).

High spectral resolution ALMA imaging of AGN have also revealed both Galactic and extragalactic narrow molecular absorption lines (with typical FWHM $\lesssim 20$ km s $^{-1}$; e.g., A. Klitsch et al. 2019; T. Rose et al. 2019a). To that end, we first imaged each spw (or set of overlapping spws) using *tclean* with Briggs ($r = 0.5$) weighting at the native channel binning given in Table A1, resulting in 72 continuum-dominated spectral cubes with a common restoring beam for each spectral setup. Peak flux densities are plotted in Figure C2 across all unflagged frequencies for the entire sample. Absolute flux calibration uncertainties for MFS images and spectral cubes is about 5% in Band 3 and 10% in Bands 6 and 7 (E. Fomalont et al. 2014; L. Francis et al. 2020a; G. Privon et al. 2024). For most spws in the archival sample, channels are coarsely binned ($\Delta v \sim 20 - 100$ km s $^{-1}$). Only four

projects (2012.1.00661.S, 2013.1.00073.S, 2015.1.00030.S, and 2016.1.00021.S) have sufficiently fine FDM channels ($\Delta\nu_{\text{obs}} \sim 0.6\text{--}3 \text{ km s}^{-1}$) to enable detection of narrow molecular lines.

Lastly, we subtracted the continuum for MSs containing CO transitions using the `uvcontsub` task (with `fitorder = 1`) with three distinct fitting regions. In the first and second cases, we excluded channels corresponding to either $|v_{\text{LOS}} - v_{\text{sys}}| < 500 \text{ km s}^{-1}$ to probe more standard velocity ranges for extragalactic gas or $< 1000 \text{ km s}^{-1}$ for higher-amplitude rotation or outflow scenarios. Given the truncated CO(3–2) velocity coverage in program 2012.1.00661.S, for the second case we only excluded the range $-1000 < v_{\text{LOS}} - v_{\text{sys}} < 400 \text{ km s}^{-1}$ when subtracting the Band 7 continuum. In a third case for CO(1–0) only, we excluded the ranges $100 < |v_{\text{LOS}} - v_{\text{sys}}| < 2200 \text{ km s}^{-1}$ to test for possible broad emission-line features that may originate from a pc-scale molecular CNL. In this final case, including channels where $|v_{\text{LOS}} - v_{\text{sys}}| < 100 \text{ km s}^{-1}$ helped to anchor the continuum subtraction as the integrated emission is minimal near v_{sys} (e.g., B. D. Boizelle et al. 2017; M. D. Smith et al. 2021). We imaged the continuum-subtracted data into spectral cubes at both the native frequency spacing and at more coarse binning ($\sim 20\text{--}40 \text{ km s}^{-1}$) to increase the signal-to-noise ratio (S/N). In Sections 3 and 4, we explore relatively narrow emission and absorption-line results derived using the first `uvcontsub` case. In Appendix E, we explore the second and third `uvcontsub` cases that produce very faint (and likely spurious) spectral deficits or excesses near redshifted CO transitions.

3. SPECTRAL LINE PROPERTIES

Here, we focus on a spectral line search for extragalactic CO near the redshift of M87. ALMA spectra extracted against and around the M87 nucleus are remarkably featureless, confirming previous mm-wavelength studies in finding no strong extragalactic molecular lines in the inner $\sim 20''$ ($\sim 1.6 \text{ kpc}$; e.g., J. Braine & T. Wiklind 1993; J. C. Tan et al. 2008). Integrated line profiles and peak continuum spectra in spws covering redshifted CO result primarily in $S_{\text{CO}}\Delta\nu$ upper limits and low CO opacities. Additional dense gas tracers (e.g., SiO, CS, and HCN) are covered in certain data sets, but because of the expected low relative abundance of isotopologues or more exotic molecules (A. Crocker et al. 2012) and spectral setups without sufficiently fine FDM binning, these ALMA data do not allow for a broader line search. The ALMA 12-m spectra also show no evidence for Galactic CO(1–0) emission or absorption more directly about the M87 nucleus, even in spectra with binning $\Delta\nu_{\text{obs}} < 3 \text{ MHz}$ that could resolve narrow Galactic lines (whose line FWHM are often $\lesssim 10 \text{ km s}^{-1}$; R. D. Davies & E. R. Cummings 1975; M. R. Rugel et al. 2018).

A detailed mm/sub-mm line search is somewhat complicated by atmospheric lines that were not fully removed during calibration (J. Shangguan et al. 2020). The residual impact is typically over a narrow frequency range and at the percent level or less, but it does affect extragalactic CO(2–1)

detection for M87. In Appendix D, we employ atmospheric transmission models to confirm the location and strength of telluric lines to avoid missing or misclassifying extragalactic lines.

3.1. CO Emission-line Constraints

For any detectable molecular gas accompanying the CNL or individual filamentary features, we expected CO emission line speeds to be similar to those of the cospatial atomic gas. Within the CNL, atomic gas speeds reach about $|v_{\text{LOS}} - v_{\text{sys}}| < 500 \text{ km s}^{-1}$. For filamentary structures out to a couple kpc, the gas speeds span $\pm 400 \text{ km s}^{-1}$ (A. Boselli et al. 2019; J. Osorno et al. 2023). To conduct an efficient emission-line search within M87, we extracted profiles from the X5 and Xa1 spectral cubes that excluded channels with $|v_{\text{LOS}} - v_{\text{sys}}| < 500 \text{ km s}^{-1}$ in the continuum subtraction. Visibilities were imaged into 20 km s^{-1} channels to better match the observed CO widths of other resolved cloud structures (e.g., the SE cloud; A. Simionescu et al. 2018).

In Figure 1, we trace broad regions of diffuse ionized atomic gas emission and higher H α /H β decrement (W1, W2, bar, and loop regions; W. B. Sparks et al. 2004; J. Osorno et al. 2023) as well as more compact regions that cover higher dust opacities (south of the nucleus and in a filament in atomic emission-line region W1; T. R. Taylor et al. 2020). A final region in the jet (covering clumps A, B, and C; Figure 2) explores the higher-pressure, shocked ISM (G. V. Bicknell & M. C. Begelman 1996). From the F475W residual image, the dense dusty clump has an estimated intrinsic (deconvolved) width of $\sim 30 \text{ pc}$ while the neighboring dusty filaments (and those in the W1 and loop regions) appear to have intrinsic diameters ranging from $\sim 10 \text{ pc}$ down to perhaps just 1–2 pc. Another dusty filament appears to span from the dense cloud to the west side of the loop region and comes close to the nucleus ($R \lesssim 0''.5$ separation; EHT MWL Science Working Group et al. 2024).

In Figure 3 and Table 1, we present integrated CO(1–0) line profiles and fluxes for the intermediate resolution Xa1 data set ($\bar{\theta}_{\text{FWHM}} \sim 0''.21$). These line profiles reveal no unambiguous CO emission in any region, and the higher-resolution X5 data yields poorer constraints due to the larger number of beams in each integration area. Where there is cospatial atomic gas seen in the F660N filter, we integrated line profiles over the range of atomic gas v_{LOS} observed in (or around) these regions with an additional $\pm 100 \text{ km s}^{-1}$ buffer. In dust-dominated regions seen primarily in the F475W filter, line profiles were integrated over a $\sim 300 \text{ km s}^{-1}$ range centered on v_{sys} . To encompass the entire atomic gas CNL, we integrated over a circular aperture with a radius $R = 0''.5$ ($\sim 40 \text{ pc}$). An additional annulus integration between $0''.2 < R < 0''.5$ avoided larger nuclear residuals while still including most of the observed ionized gas emission (J. Osorno et al. 2023). For comparison, we include the central SMA CO line

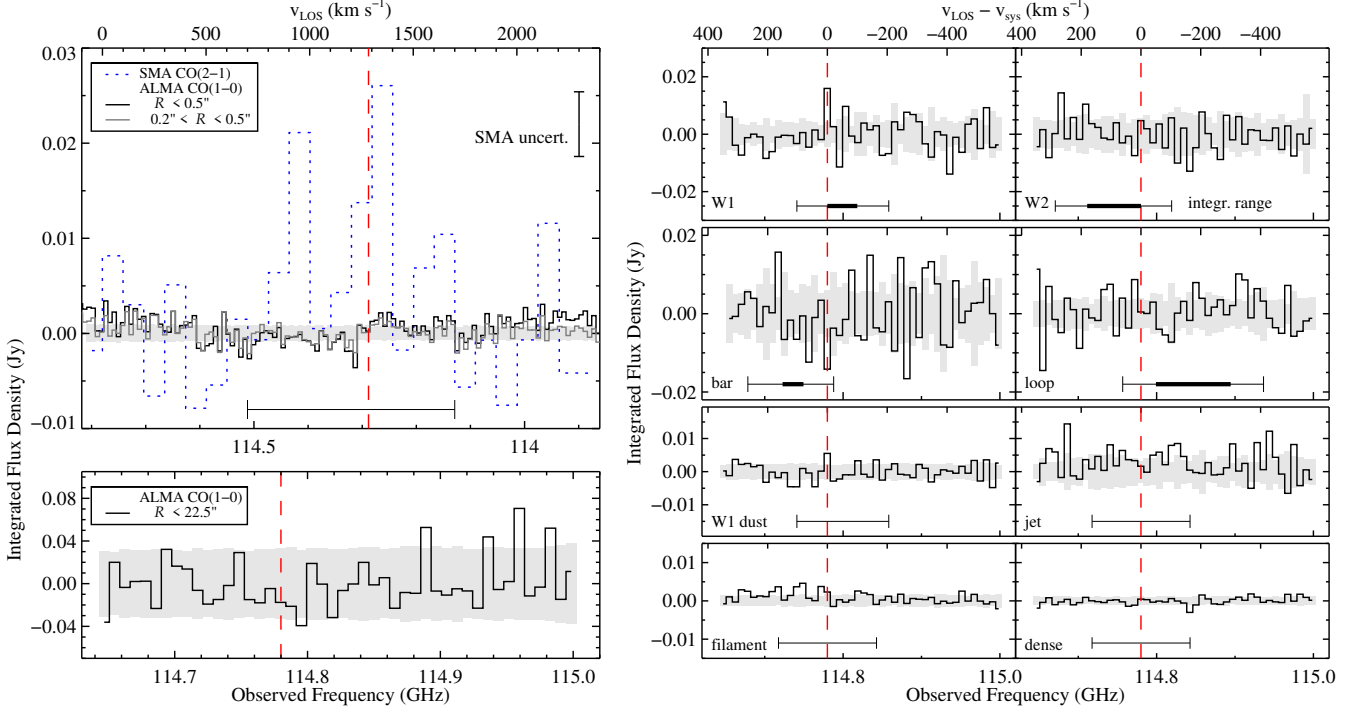


Figure 3. CO(1–0) line profiles and uncertainty ranges extracted from the Xa1 continuum-subtracted spectral cube. Those centered on the nucleus include a circular aperture or annulus covering the CND extent with wide velocity extent (*top left panel*) as well as a global CO(1–0) line profile out to a projected radius $R < 0.5 \times \text{HPBW}$ (*bottom left*). In the nuclear spectrum with a circular aperture, a hint of central CO(1–0) absorption is still detected in the bin covering $v_{\text{LOS}} - v_{\text{sys}} \sim -80 \text{ km s}^{-1}$. The SMA CO(2–1) profile is included for comparison (J. C. Tan et al. 2008). The remaining spectra (*right panels*) were extracted using regions outlined in Figure 1. Integration ranges (horizontal lines) are shown below the line profiles. For regions with filamentary or disk-like atomic gas emission, the approximate range of atomic gas velocities are included (thick bars). The redshifted $\nu_{\text{CO}(1-0)}$ is shown in each panel (for $z_{\text{obs}} = 0.004283$; dashed lines).

profile, recovered from J. C. Tan et al. (2008) using PlotDigitizer⁷.

To estimate uncertainties, we followed a Monte Carlo (MC) resampling technique that iteratively shifted each region by a random amount before re-integrating (without overlapping any defined regions; B. D. Boizelle et al. 2017). After 200 iterations, we adopted the standard deviation of the “blank” flux densities in each channel as a good proxy for the true uncertainty spectrum (for a more comprehensive approach, see T. Tsukui et al. 2023). In some cases, the spread in “blank” flux densities is slightly higher (by at most 10%) due to the impact of the primary beam correction further from the ALMA phase center, but this does not materially affect the analysis.

Based on the estimated noise spectra, the highest S/N candidate for CO emission is in the outer jet feature with an integrated $S_{\text{CO}(1-0)}\Delta v \approx 1.19 \pm 0.36 \text{ Jy km s}^{-1}$ that barely exceeds the 3σ threshold. However, a channel-by-channel inspection of the integration over the velocity range shows no clear features. The dust filament and loop regions show positive features near v_{sys} at a 2σ – 3σ confidence, but the bulk of the signal being contained in 1–2 channels is not altogether

convincing. Channel inspection did not reveal any likely discrete sources at the corresponding velocities (or elsewhere). A global CO(1–0) line profile integrated over the inner $\sim 2 \text{ kpc}$ returns only an upper limit $S_{\text{CO}(1-0)}\Delta v < 4.8 \text{ Jy km s}^{-1}$ over the entire $\pm 500 \text{ km s}^{-1}$ range.

The nuclear and annulus spectra also show no support for CO(1–0) emission. From typical rms uncertainties of $0.68 \text{ mJy beam}^{-1}$ in a 20 km s^{-1} channel, we estimated nuclear $S_{\text{CO}(1-0)}\Delta v < 0.109 \text{ Jy km s}^{-1}$ (1σ uncertainty) in a broad $|v_{\text{LOS}} - v_{\text{sys}}| < 500 \text{ km s}^{-1}$ range to match the extraction region and velocity range of the previous SMA CO(2–1) study (J. C. Tan et al. 2008). The annulus region spectrum is better behaved than the composite nuclear spectrum, which shows excesses at large velocity offsets ($|v_{\text{LOS}} - v_{\text{sys}}| \gtrsim 800 \text{ km s}^{-1}$) due to higher continuum residuals directly at the nucleus location. In Appendix E, we discuss the anomalous spectral behavior when excluding an even broader channel range in the `uvcontsub` process.

3.2. CO Absorption-line Properties

Despite the lack of any CO detection in emission, close inspection of the peak continuum spectra in Figure 4 reveals CO(1–0), CO(2–1), and CO(3–2) absorption features across 6 data sets with blueshifts corresponding to $-84 < v_{\text{LOS}} - v_{\text{sys}} < -75 \text{ km s}^{-1}$. Only one CO spw with nar-

⁷ <https://plotdigitizer.com>

Table 1. M87 CO(1–0) Emission-line Constraints

Region Name	Area (N_{beam})	rms (mJy)	Peak ν_{obs} (GHz)	Peak Excess (Jy km s ⁻¹)	ν_{obs} Range (GHz)	min, max($v_{\text{LOS}} - v_{\text{sys}}$) (km s ⁻¹)	Range Excess (Jy km s ⁻¹)
(1)	(2)	(3)	(4)	(5)	(6)	(7)	(8)
Atomic Gas Regions							
W1	433.5	4.85	114.780	0.380 (0.113)	114.741–114.858	–205.2, +102.1	<0.414
W2	515.2	5.60	114.678	0.295 (0.109)	114.670–114.819	–102.8, +286.8	0.639 (0.519)
bar	595.5	7.57	114.834	0.383 (0.129)	114.678–114.788	–20.9, +266.3	<0.633
loop	253.3	4.46	114.741	0.230 (0.073)	114.756–114.889	–409.7, +61.1	0.883 (0.464)
jet	150.0	4.23	114.827	0.276 (0.105)	114.741–114.858	–205.2, +102.1	1.193 (0.355)
Dust Regions							
W1 dust	45.9	2.32	114.741–114.858	–205.2, +102.1	<0.191
filament	20.9	1.44	114.717–114.842	–164.3, +163.6	0.502 (0.123)
dense	10.1	1.00	114.717–114.842	–164.3, +163.6	<0.085
Nuclear Regions							
nucleus	12.9	0.69	114.585–114.976	–514.0, +510.6	<0.109
annulus	10.8	0.68	114.585–114.976	–514.0, +510.6	<0.085

NOTE—Tentative CO(1–0) emission (or upper limits) near the center of M87 from the Xa1 spectral cube with 20 km s⁻¹ binning and typical rms \sim 0.4 mJy beam⁻¹ per channel. Regions listed in col. (1) are shown in Figure 1 with corresponding beam-unit areas in col. (2). Col. (3) is the average rms per channel within each integration region. Cols. (4) and (5) give frequencies and integrated fluxes for the single channel with the highest flux density ($S/N \gtrsim 3$) in each region. Cols. (6) and (7) give the frequency ranges and velocity endpoints corresponding to ± 100 km s⁻¹ from the observed spread of atomic gas v_{LOS} in each region or ± 150 km s⁻¹ about v_{sys} for the dust-dominated regions. Col. (8) reports the possible CO fluxes (or upper limits) in these regions. Note that the peak excess in the integrated CO profile in Figure 3 does not always fall within the velocity integration ranges. Estimated 1σ uncertainties were calculated by MC resampling of the background noise using the same region shapes.

row $\Delta\nu_{\text{obs}} \lesssim 1$ MHz from the X1b0 data set returns a non-detection. Its more complicated spectral response shown in Figure C2 is ameliorated by using just the lowest-rms data from the second EB. However, the more selective spectrum still appears featureless (see Figure 4) due to a sensitivity limit that exceeds the expected peak opacity τ_0 in the common spectral definition:

$$\tau_\nu = -\ln\left(\frac{T_\nu}{T_{\nu,\text{cont}}}\right). \quad (1)$$

Here, the peak continuum spectrum $T_\nu \propto S_\nu/\theta_{\text{maj}}\theta_{\text{min}}$ is measured in K units and $T_{\nu,\text{cont}}$ is the fitted linear continuum level about the CO line feature. For the most confident cases, the measured $\tau_0 \lesssim 0.004$ values are much lower than for CO absorption lines observed in other ETGs (typically $\tau_0 \sim 0.1$ – 0.2 but it may approach unity; B. D. Boizelle et al. 2017; I. Ruffa et al. 2019; A. Klitsch et al. 2019; T. Rose et al. 2019a,b, 2020; S. Kameno et al. 2020). No other potential extragalactic CO or dense gas absorption lines are seen at a consistent $v_{\text{LOS}} - v_{\text{sys}}$ across multiple data sets or transitions, including at the same $v_{\text{LOS}} - v_{\text{sys}} \sim -131$ km s⁻¹ for the atomic-gas absorber.

From these opacity spectra, we also calculated upper limits of the integrated line opacity

$$\tau_{\text{CO}} = \int \tau_\nu d\nu \quad (2)$$

for CO absorption in km s⁻¹ units. Across these three transitions, the $\tau_{\text{CO}} \sim 0.02$ – 0.05 km s⁻¹ range (with a median

$S/N \sim 4$) are very low and better match the bottom end of the τ_{CO} distribution for diffuse Galactic clouds (e.g., H. S. Liszt & R. Lucas 1998; H. S. Liszt & J. Pety 2012; H. Liszt et al. 2019).

CO(2–1) absorption lines are detected less confidently than are CO(1–0), with an extreme case from the X20d data that only partially detects $\tau_{0,\text{CO}(2-1)}$ with $S/N \sim 1.4$. What is measured may be ~ 20 – 30% lower due to difficulty in fully removing the neighboring ozone line contamination (see Appendix D). Two APP-mode programs cover the redshifted CO(2–1) frequency, but these peak spectra display frequency-dependent fluctuations due to phasing all elements together into a single array. Some of the .V program spectra appear to show CO(2–1) absorption, but we only utilize spectral fits to the most regular Xb data set from program 2016.1.01154.V when calculating CO absorber properties.

To better characterize these line properties, we fit each CO absorption feature with a Gaussian line profile and a linear continuum to recover the line centroid (ν_{LOS} , v_{LOS}), line width (σ_{LOS}), and peak opacity (τ_0). For results, see Figure 4 and Table 2). These fits incorporated Hanning smoothing⁸ to

⁸ In frequency space, Hanning smoothing operates as a convolution of the FDM data before on-line channel averaging. The triangular kernel consists of three channels with a central and side amplitude of 0.50 and 0.25, respectively. Native frequency binning is found in Table A1 and finely-binned FDM data have frequency resolutions up to $2\times$ larger due to Hanning smoothing. For those with the narrowest $\Delta\nu_{\text{obs}} < 1$ MHz, the intrinsic line widths are $\sim 7\%$ lower than the blurred values; for those with $\Delta\nu_{\text{obs}} > 5$ MHz, there is no change.

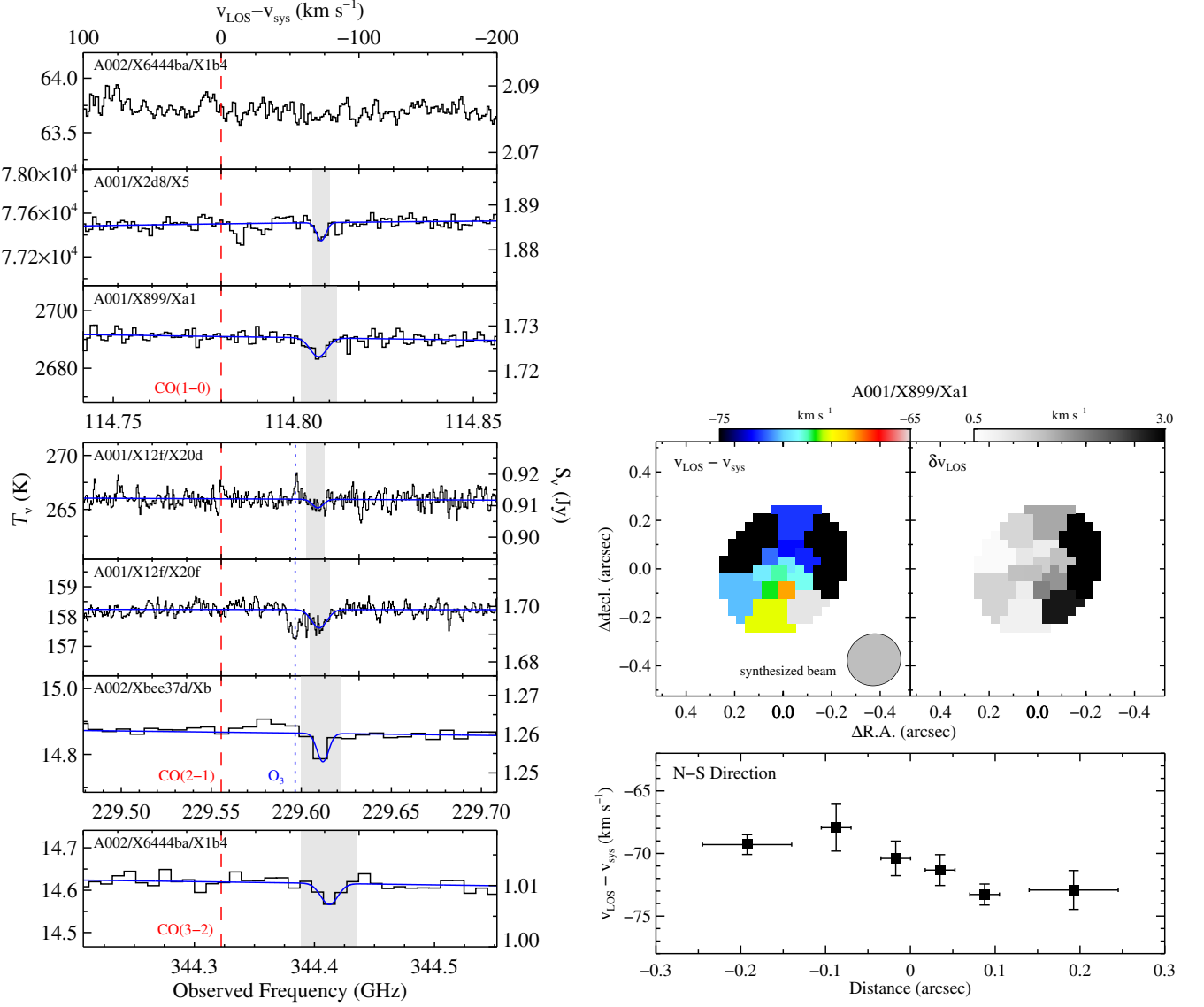


Figure 4. CO absorption lines detected against the bright M87 nucleus. Taken together, the peak continuum spectra at the native channel binning (*left panels*) provide unambiguous support for narrow, blueshifted CO absorption near the M87 redshift ($z_{\text{obs}} = 0.004283$; red dashed lines). The X1b0 spectrum using data from only the higher-S/N second EB was still too noisy to confidently identify faint CO(1–0) with peak opacity $\tau_0 \lesssim 0.003$. Gaussian fits (blue solid lines) show centroids across $-75 < v_{\text{LOS}} - v_{\text{sys}} < -84 \text{ km s}^{-1}$ with narrow intrinsic line widths ($\sim 4\text{--}6 \text{ km s}^{-1}$). For the CO(2–1) transition, an atmospheric ozone line nearly overlaps with the (shaded) regions used to calculate integrated opacities. Spatial binning and Gaussian refitting of spectra extracted from the Xa1 continuum cube enabled determination of $v_{\text{LOS}} - v_{\text{sys}}$ values and velocity uncertainties δv_{LOS} across ~ 2 beam widths (*top right*; $\bar{\theta}_{\text{FWHM}} \sim 0''.22$). This limits a possible velocity gradient to be $\lesssim 3 \text{ km s}^{-1}$ across $\sim 10 \text{ pc}$ (*bottom right*).

recover intrinsic σ_{LOS} . We estimated parameter uncertainties by an MC resampling technique that adds random noise to the best-fitting model spectrum before refitting. The noise was drawn from a normal distribution with a standard deviation equal to that of line-free portions of each spectrum. During this process, we also explored channelization effects by randomly shifting the bin centers by a uniform fraction of a channel width when constructing the model spectrum. These frequency shifts were also drawn from a normal distribution with standard deviation equal to a quarter of the corresponding $\Delta\nu_{\text{obs}}$ value in Table A1. This final step helps to pro-

vide more realistic line width uncertainties in cases where the measured width $\sigma_{\text{LOS}} \lesssim \Delta\nu_{\text{obs}}$. Incorporating Hanning smoothing also better accounts for correlated spectral noise, although it cannot explain apparently coherent spectra features over frequency ranges $\gtrsim 3\Delta\nu_{\text{obs}}$ (e.g., see the X5 spectrum in Figure 4). Broader uncertainties on τ_{CO} were also determined in this way. We note that bandpass calibration limitations are liable to introduce larger pattern noise (at the $\sim 0.1\%$ level and within the model fitting region), creating low-level structure in the spectral response that is not represented in the linear $T_{\nu, \text{cont}}$ fit. This appears most clearly in the

Table 2. M87 Narrow CO Absorption-line Properties

Member	rms	ν_{LOS}	$\nu_{\text{LOS}} - \nu_{\text{sys}}$	σ_{LOS}	τ_0	τ_{CO}	
OUS	(mJy beam ⁻¹)	(GHz)	(km s ⁻¹)	(MHz)	(km s ⁻¹)	(km s ⁻¹)	
(1)	(2)	(3)	(4)	(5)	(6)	(7)	(8)
CO(1–0)							
A002/X6444ba/X1b0	2.61	< 0.056	
A001/X2d8/X5	0.91	114.808 (0.000287)	−78.45 (0.75)	1.204 (0.317)	3.13 (0.82)	0.002286 (0.000785)	0.0220 (0.0059)
A001/X899/Xa1	1.15	114.807 (0.000468)	−76.38 (1.22)	2.275 (0.526)	5.92 (1.37)	0.002483 (0.000735)	0.0361 (0.0068)
CO(2–1)							
A001/X12f/X20d	2.38	229.609 (0.001600)	−75.29 (2.08)	3.012 (1.977)	3.92 (2.57)	0.002989 (0.002185)	0.0325 (0.0078)
A001/X12f/X20f	1.89	229.610 (0.000533)	−76.31 (0.69)	4.259 (0.527)	5.54 (0.69)	0.003904 (0.000677)	0.0438 (0.0053)
A002/Xbee37d/Xb	0.85	229.612 (0.001210)	−78.94 (1.57)	3.211 (1.340)	4.18 (1.73)	0.005798 (0.003290)	0.0461 (0.0109)
CO(3–2)							
A002/X6444ba/X1b4	0.95	344.412 (0.003276)	−83.58 (2.84)	7.119 (3.592)	6.17 (3.11)	0.003418 (0.002263)	0.0574 (0.0174)

NOTE—CO absorption-line properties measured from the M87 peak continuum spectra. Col. (2) gives the typical rms noise per channel. Cols. (3) to (6) are best-fit velocity and line width parameter values from Gaussian fitting with the σ_{LOS} values being intrinsic widths before any online Hanning smoothing. Cols. (7) and (8) report the peak and integrated CO opacities after continuum fitting and normalization. Uncertainties in these fitted Gaussian parameters and opacities (in parentheses) were estimated using a Monte Carlo resampling technique.

CO(3–2) spectrum (see Figure C2). However, we do not attempt to quantify bandpass calibration effects on τ_0 and τ_{CO} values.

The ratio of centroid frequencies (or weighted-average $\bar{\nu}$ when multiple observations exist) are broadly consistent with expectations using standard error propagation:

$$\frac{\bar{\nu}_{\text{CO}(3-2)}}{\bar{\nu}_{\text{CO}(1-0)}} - 3 = (-8.96 \pm 2.67) \times 10^{-5}$$

$$\frac{\bar{\nu}_{\text{CO}(2-1)}}{\bar{\nu}_{\text{CO}(1-0)}} - 2 = (-4.15 \pm 0.58) \times 10^{-5}.$$

Deviations from the expected zero values are likely due to low-S/N CO(2–1) detection and an anomalously high $\nu_{\text{CO}(3-2)}$ value. We note that including the APP-mode value in Table 2 when calculating $\bar{\nu}_{\text{CO}(2-1)}$ does not contribute appreciably to the measured $\bar{\nu}_{\text{CO}(2-1)}/\bar{\nu}_{\text{CO}(1-0)} - 2$ offset from zero. In velocity units, these fits give consistent (intrinsic) line widths of $\sim 3\text{--}6$ km s⁻¹ and typical $\nu_{\text{LOS}} - \nu_{\text{sys}} \sim -75$ to -79 km s⁻¹, although the CO(3–2) feature has a more blueshifted central velocity that is discrepant by $\sim 3\sigma$ from the weighted-average CO(1–0) and CO(2–1) centroid values.

For use later when constraining molecular gas properties, we also constructed final weighted-average peak opacities $\bar{\tau}_{0,\text{CO}(1-0)} = 0.00239 \pm 0.00054$ and $\bar{\tau}_{0,\text{CO}(2-1)} = 0.00390 \pm 0.00063$. If ignoring the APP-mode results from the Xb data set, $\bar{\tau}_{0,\text{CO}(2-1)}$ only changes by $\sim 2\%$. The integrated opacity $\bar{\tau}_{\text{CO}(1-0)} = 0.0281 \pm 0.0045$ km s⁻¹ is moderately lower than measured for $\tau_{\text{CO}(3-2)}$ while the latter is formally consistent with $\bar{\tau}_{\text{CO}(2-1)} = 0.0410 \pm 0.0041$ km s⁻¹.

The core continuum source at the center of M87 is very compact, with the brightest component having a radial size of ~ 25 μas (0.002 pc; EHT Collaboration et al. 2019) that is expected to probe a very narrow line of sight through the

CO absorber. At high resolution (e.g., V. A. Acciari et al. 2009), this very compact core brightness may account for only $\sim 25\text{--}45\%$ of the integrated flux density that remains unresolved in these ALMA data after extrapolating the synchrotron core and jet behavior from 3.5 mm (with spectral index $\alpha \sim -0.6$ for $S_\nu \propto \nu^\alpha$; see Figure B1 and R.-S. Lu et al. 2023). As discussed in Appendix A.1, the next brightest compact synchrotron source (the N2 clump) lies < 2 pc in projection from the nucleus with an integrated mm-wavelength core-to-N2 flux density ratio of ~ 25 . On smaller scales at radio wavelengths, the synchrotron jet core-to-jet flux density ratio approaches ~ 100 (e.g., C. C. Cheung et al. 2007; R. C. Walker et al. 2018).

The question is whether the continuum emission from the approaching synchrotron jet emission (oriented at a PA $\sim -65^\circ$ from the core) probes sufficiently distinct lines of sight through the absorbing cloud to be sensitive to a possible velocity gradient. We attempted to answer this by refitting the CO(1–0) detection from the Xa1 data across the central beam area ($\bar{\theta}_{\text{FWHM}} \sim 0''.2$ or ~ 15 pc). Spectra in adjacent spatial pixels were combined together using Voronoi tessellation (M. Cappellari & Y. Copin 2003) prior to refitting to achieve roughly uniform continuum S/N per bin. Figure 4 shows the velocity gradient to be no more than 3 km s⁻¹ across ~ 10 pc, with the putative gradient being oriented in a mostly N–S direction. Individual uncertainties were estimated using the same MC resampling approach. The other CO(1–0) continuum cube from the X5 data set had much higher angular resolution but insufficient S/N in binned spectra to measure opacities within the central beam areas.

3.3. Temperature and Column Densities

The relative level occupation defines an excitation temperature T_{ex} for two different transitions. Given the higher con-

confidence in the lower- J τ_{CO} , we first solved column density equations that relate integrated CO(2–1) and CO(1–0) opacities with a common T_{ex}^{21} (B. Godard et al. 2010; T. Rose et al. 2019a) by

$$\frac{\tau_{\text{CO}(2-1)}}{\tau_{\text{CO}(1-0)}} \left[\frac{\nu_{\text{CO}(2-1)}}{\nu_{\text{CO}(1-0)}} \right]^3 \frac{g_1 A_{10}}{g_2 A_{21}} = \frac{1 - e^{-h\nu_{\text{CO}(2-1)}/kT_{\text{ex}}^{21}}}{e^{h\nu_{\text{CO}(1-0)}/kT_{\text{ex}}^{21}} - 1}. \quad (3)$$

A similar equation relates a common T_{ex}^{32} for adjacent CO(3–2) and CO(2–1) transitions. Here, $g_u = 2J_u + 1$ is the upper-level degeneracy for that radiative transition and A_{ul} is the corresponding Einstein coefficient for spontaneous decay⁹. This assumes a single-zone system in local thermodynamic equilibrium (LTE) where adjacent transitions (e.g., $J = 0 \rightarrow 1$ and $1 \rightarrow 2$) originate under the same conditions. We have ignored beam filling factors and also considered the impact of the CMB background to be negligible at this redshift and for the measured T_{ex}^{21} and T_{ex}^{32} values. Individual τ_{CO} have lower S/N, so we employed weighted average $\bar{\tau}_{\text{CO}}$ values to recover more confident T_{ex} .

In Figure 5, we compare measured opacity ratios with theoretical values assuming the absorbing medium is in LTE with equivalent $T_{\text{ex}}^{32} = T_{\text{ex}}^{21}$. However, the relatively large depth of the CO(3–2) feature as evidenced by $\tau_{\text{CO}(3-2)}/\bar{\tau}_{\text{CO}(2-1)} \approx \bar{\tau}_{\text{CO}(2-1)}/\bar{\tau}_{\text{CO}(1-0)}$ is not consistent with LTE expectations. This may indicate an elevated $J = 2$ population, possibly arising from absorption-line contributions by gas in distinct spatial or energetic regions. Unfortunately, neither $\tau_{\text{CO}(3-2)}$ or $\bar{\tau}_{\text{CO}(2-1)}$ values are as reliable as is $\bar{\tau}_{\text{CO}(1-0)}$, and we do not attempt any reconciliation in the LTE framework. In Section 4.2.3, we use radiative transfer modeling to better account for possible deviations from LTE.

To determine a total column density N_{CO} , we primarily considered CO(1–0) absorption and an excitation temperature for the lowest- J transitions:

$$N_{\text{CO}} = Q_{\text{rot}} \left(\frac{8\pi\nu_{ul}^3}{c^3} \right) \frac{g_0}{g_1} \frac{1}{A_{10}} \frac{1}{1 - e^{-h\nu_{\text{CO}(1-0)}/kT_{\text{ex}}^{21}}} \tau_{\text{CO}(1-0)}. \quad (4)$$

This relationship assumes detailed balancing and the temperature-dependent ¹²CO rotational partition function Q_{rot} (J. Mangum & Y. Shirley 2015). Assuming LTE, the kinetic temperature $T_K = T_{\text{ex}}$. Here, we used $\bar{\tau}_{\text{CO}(1-0)}$ for more confident N_{CO} determination.

We recovered more reliable error bars in a series of trials by drawing individual τ_{CO} randomly from normal distributions centered on their measured value with standard deviations equal to their 1σ uncertainties in Table 2. After calculating weighted-average opacities at each iteration, we used the best-fit T_{ex} to find a new Q_{rot} and N_{CO} . After 10^5 iterations, we used the 15.9 to 84.1 (0.14 to 99.87) percentile levels of the T_{ex}^{21} distribution to find a median $T_{\text{ex}}^{21} = 7.77^{+1.34}_{-1.94} \text{ (}^{+14.88}_{-2.90}\text{) K}$ and $N_{\text{CO}}/10^{15} \text{ cm}^{-2} = 1.16^{+0.21}_{-0.28} \text{ (}^{+3.55}_{-0.47}\text{)}$ with 1σ (3σ) error bars.

Calculated separately, we find higher median $T_{\text{ex}}^{32} = 28.6^{+26.7}_{-14.9}$ K (1σ) with $N_{\text{CO}} \sim 10^{16} \text{ cm}^{-2}$ that are much less confident due to a relatively larger $\tau_{\text{CO}(3-2)}$ uncertainty.

4. DISCUSSION

4.1. CO Emission

Similar cool-core BCGs frequently host rotation-dominated CNDs and/or extended filaments with CO-derived total molecular gas masses $M_{\text{H}_2} \sim 10^8 M_{\odot}$ (V. Olivares et al. 2019; J. Baek et al. 2022). CO surveys have found a positive correlation between integrated H α luminosity $L_{\text{H}\alpha}$ and total M_{H_2} for cool-core galaxies (e.g., A. C. Edge 2001; P. Salomé & F. Combes 2003; F. A. Pulido et al. 2018). Among these massive elliptical galaxies, M87 has a low but confident¹⁰ $L_{\text{H}\alpha} \sim (0.8 - 1.1) \times 10^{40} \text{ erg s}^{-1}$ that would be consistent with a global $M_{\text{H}_2} \sim (0.8 - 9) \times 10^8 M_{\odot}$. However, previous low- J CO observations of M87 placed a much more strict $M_{\text{H}_2} \lesssim (5 - 10) \times 10^6 M_{\odot}$ on the nuclear molecular gas using both small and large apertures ($R \sim 0''.5$ to $\sim 23''$; P. Salomé & F. Combes 2008; J. C. Tan et al. 2008) and $< 10^8 M_{\odot}$ globally (W. Jaffe 1987). Similar upper limits from this ALMA CO search suggest that M87 is either a clear outlier in the $L_{\text{H}\alpha} - M_{\text{H}_2}$ correlation for cool-core galaxies or that there is much wider scatter in this correlation.

Figure 3 demonstrates that these archival ALMA data do not support any CO emission-line detection from dusty clumps or atomic gas filaments. In the nucleus ($R < 0''.5$) we find a limiting $S_{\text{CO}(2-1)}\Delta\nu < 0.109 \text{ Jy km s}^{-1}$ with a 20% lower value for the annulus region. A standard CO(1–0)-to- H_2 conversion factor $\alpha_{\text{CO}} = 3.1 M_{\odot} \text{ pc}^{-2} (\text{K km s}^{-1})^{-1}$ (K. M. Sandstrom et al. 2013) results in $M_{\text{H}_2} < 2.3 \times 10^5 M_{\odot}$ that is $\sim 20\times$ lower than any previous upper limit. Both this M_{H_2} limit and the corresponding (deprojected) surface mass density $\bar{\Sigma}_{\text{H}_2} < 45 M_{\odot} \text{ pc}^{-2}$ averaged over the atomic CND extent are lower than for many CO-detected molecular CNDs in other massive elliptical galaxies (B. D. Boizelle et al. 2017; I. Ruffa et al. 2019; M. D. Smith et al. 2021). Integrated line profiles for the larger-scale W1, W2, bar, and loop regions have individual detection thresholds at the $\sim 0.4\text{--}0.6 \text{ Jy km s}^{-1}$ level that translates to $M_{\text{H}_2} \lesssim (0.8 - 1.3) \times 10^6 M_{\odot}$. All together, these regions give a total $M_{\text{H}_2} \lesssim 3 \times 10^6 M_{\odot}$ that is similar to a global $< 4 \times 10^6 M_{\odot}$ limit when using a circular aperture with 2 kpc radius.

In these CO line profiles, the single-channel ($\Delta\nu = 20 \text{ km s}^{-1}$) excess in the W1 and bar regions and an integrated excess ($\Delta\nu = 100 \text{ km s}^{-1}$) in the jet region over clumps A–C may hint at CO emission. However, the low estimated S/N ~ 3 and a lack of clear compact or diffuse CO emission at the corresponding locations and frequencies disfavor that interpretation. For broad detection, the only possible candidate is the dust filament found $1''.5\text{--}2''.5$ to the southeast of

¹⁰ Not all cool-core galaxies host CNDs that could contribute to the global $L_{\text{H}\alpha}$. For M87, atomic CND contributions to the global $L_{\text{H}\alpha}$ are only $1.7 \times 10^{39} \text{ erg s}^{-1}$ (W. B. Sparks et al. 1993; J. L. Walsh et al. 2013; J. Osorno et al. 2023).

⁹ Obtained from Splatalogue: <https://splatalogue.online/#/advanced>

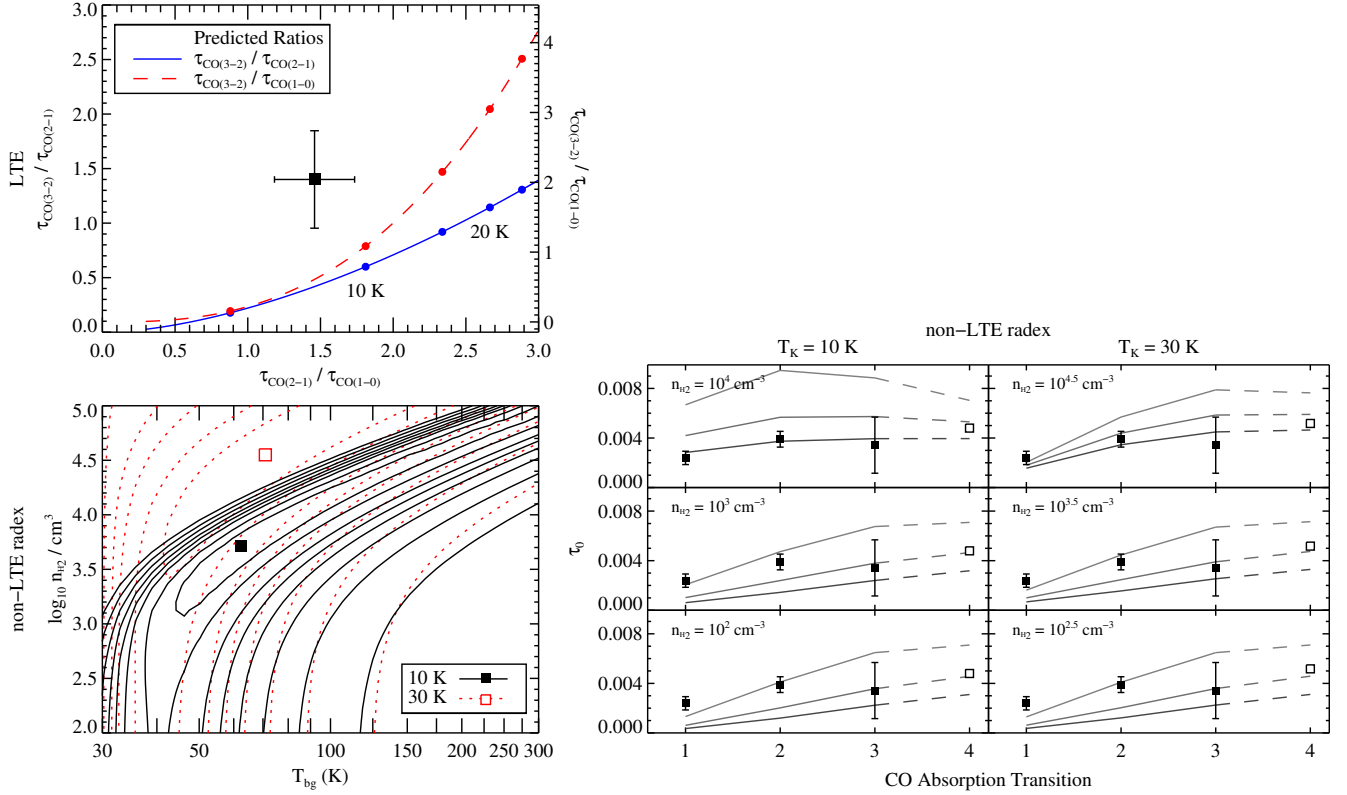


Figure 5. Comparison between observed and predicted absorption-line opacities for the M87 CO absorber. Integrated opacity ratios (*top left panel*) do not agree with LTE predictions (circles showing T_{ex} separated by 5 K). Non-LTE *radex* modeling (F. F. S. van der Tak et al. 2007) for cold gas ($T_K \leq 30$ K) using the measured absorption-line FWHM ≈ 10 km s $^{-1}$ and $N_{\text{CO}} \approx 10^{15}$ cm $^{-2}$ better reproduces the observed peak opacities (*bottom left, right*). Best-fit *radex* results for $T_K = 10$ K suggest a typical $n_{\text{H}_2} \sim 5000$ cm $^{-3}$ embedded in a hotter background temperature $T_{\text{bg}} \sim 60$ K. Inner $\Delta\chi^2 = \chi^2 - \min(\chi^2)$ contours are at the 1, 2, and 3 σ level while the remainder are arbitrarily (linearly) spaced. For comparison, the measured and *radex* model τ_0 are shown (*right*) for a range of input n_{H_2} and T_K . These plots include predicted $\tau_{0,\text{CO}(4-3)}$ for the best-fitting n_{H_2} and T_{bg} for each T_K .

the nucleus, although the integrated line profile only reaches S/N ~ 4 in the $0 < v_{\text{LOS}} - v_{\text{sys}} < 320$ km s $^{-1}$ range. Again, a channel-by-channel inspection of this region does not show any potential features above the $4 \times \text{rms}$ threshold.

The dense and filament regions adjacent to the nucleus in projection provide some additional constraints on possible CO emission. Assuming close proximity to the M87 mid-plane, this dust should obscure only half of the stellar light along those lines of sight (for more details, see L. Ferrarese et al. 1996; S. Viaene et al. 2017; B. D. Boizelle et al. 2019). Observed fractional deficits in the F475W data correspond to peak *intrinsic* $A_{\text{F475W}} = 0.75$ mag and 0.25–0.4 mag for the dense and filamentary regions, respectively (with A_{F475W} decreasing by up to half if this dust lies significantly closer to us than the midplane). Since the M87 dust-to-gas ratio is estimated to be close to MW values (W. B. Sparks et al. 1993), an expected $A_V/A_{\text{F475W}} \sim 0.84$ (J. A. Cardelli et al. 1989) and standard dust-to-extinction correlations (B. T. Draine et al. 2014) return a peak dust surface mass density $\Sigma_{\text{dust}} \sim 0.1 M_{\odot}$ pc $^{-2}$ for the dense cloud. Taking an intrinsic (deconvolved) radius (~ 4 pc) for the obscuration as a proxy for the cloud size and a standard dust-to-gas mass of ~ 0.015 (K. M. Sand-

strom et al. 2013), the expected $\Sigma_{\text{H}_2} \lesssim 7 M_{\odot}$ pc $^{-2}$ and a total $M_{\text{H}_2} \lesssim 3500 M_{\odot}$ is consistent with ALMA CO imaging non-detection. Assuming the same α_{CO} value, the corresponding integrated $S_{\text{CO}(1-0)}\Delta v$ would be about $60 \times$ lower than the upper limit found for the dense dust aperture.

Unfortunately, new ALMA 12-m CO imaging would likely result in CO(1–0) detection from either the known dusty regions or the CND. To achieve just a $3 \times$ improvement in noise (rms ~ 0.225 mJy beam $^{-1}$ in a 20 km s $^{-1}$ channel) over the Xa1 results, the ALMA Observing Tool (OT; K. Immer et al. 2024) suggests a needed on-source (total) time of 8 hrs (12.5 hrs). Further improvement with SDR $\gtrsim 3000$ over a 20 km s $^{-1}$ channel is likely beyond the current ALMA Band 3 capabilities. Unless the CND molecular gas $M_{\text{H}_2} \gtrsim 10^5 M_{\odot}$, future ALMA CO line surveys of M87 will likely not detect any molecular gas in emission.

4.2. CO Absorption

Here, we discuss the properties of extragalactic CO absorption seen against the M87 nucleus. Based on both CO opacities and kinematics, this CO absorption appears more consistent with a narrow filament instead of a gravitationally bound

cloud. We place the observed kinematics, density estimates, and temperature in context with circumnuclear gas seen both in absorption and emission in other luminous ETGs.

4.2.1. Kinematics

In other radio galaxies, CO absorption signatures appear to arise from chance alignment of dense CND molecular clouds and the bright nucleus, especially for higher disk inclination angles (e.g., B. D. Boizelle et al. 2017; T. Rose et al. 2019a; I. Ruffa et al. 2019). Absorption-line centroids tend to be close to v_{sys} (within $\pm 50 \text{ km s}^{-1}$) as clouds oriented along the disk minor axis have little if any projected motion. The weighted-average $\bar{v}_{\text{LOS}} - v_{\text{sys}} = -77.21 \pm 0.44 \text{ km s}^{-1}$ for the lower- J CO transitions are therefore not fully consistent with clouds in low-ellipticity orbits. Also, these ALMA observations provide no convincing support for a molecular phase of the atomic gas disk that is oriented more face-on ($i \sim 25^\circ$; J. Osorno et al. 2023), making disk obscuration implausible.

The primary UV/optical absorption lines that are connected to a central outflow are slightly more blueshifted ($v_{\text{LOS}} - v_{\text{sys}} \sim -131 \pm 19 \text{ km s}^{-1}$) and much broader (FWHM $\lesssim 300 \text{ km s}^{-1}$; Z. I. Tsvetanov et al. 1999a; B. M. Sabra et al. 2003) than is the CO absorption. However, these atomic gas velocities were shifted upwards by up to $\sim 60 \text{ km s}^{-1}$ to match Galactic atomic absorption-line centroids (e.g., for S I or N II) with the primary H I centroid at $cz_{\text{obs}} \sim -10 \text{ km s}^{-1}$ (R. D. Davies & E. R. Cummings 1975). Additionally, two faint optical absorption-line systems were reported at $v_{\text{LOS}} \sim 980$ and 1300 km s^{-1} (D. Carter & C. R. Jenkins 1992; D. Carter et al. 1997). While higher spectral resolution UV/optical data exists (e.g., R. Sankrit et al. 1999), they do not have sufficient sensitivity to better characterize the absorption-line profiles.

At least some of these atomic absorption lines are tied to a central outflow (B. M. Sabra et al. 2003). In AGN winds, velocity centroids and widths for broader absorbers may change significantly on \sim year timescales (J. S. Kaastra et al. 2014). Very narrow absorption-line properties do not typically show intrinsic v_{LOS} or σ_{LOS} variability (i.e., changes above a few km s^{-1} over several-year timescales; e.g., T. Misawa et al. 2014; C. J. Grier et al. 2016; T. Misawa et al. 2019; T. Rose et al. 2019b), likely due to greater physical distances from the AGN. Another possibility for M87 is that the gaseous absorption arises from a filamentary flow that appears to wrap about the nucleus (W. B. Sparks et al. 1993; J. Osorno et al. 2023). In any case, atomic and molecular absorption-line velocities and line widths would be expected to be more similar if entrained in the same gaseous outflow (M. Margulis & R. L. Snell 1989).

On kpc scales, cool-core BCGs often host multiple molecular gas clumps and filaments whose gas velocities range between about $\pm 200 \text{ km s}^{-1}$ from the BCG rest frame. Outside of strongly rotationally-broadened regions like the nucleus, CO emission FWHM are typically $30\text{--}60 \text{ km s}^{-1}$ (V. Olivares et al. 2019; J. Baek et al. 2022; S. Ganguly et al. 2023). A good example is Abell 1644-S, whose arching CO emission spans $\sim 15 \text{ kpc}$ with speeds shifting from about

-140 to $+30 \text{ km s}^{-1}$ relative to its v_{sys} , possibly connecting down to an atomic gas CND. In the most isolated regions, moderate-resolution CO imaging shows narrow emission-line FWHM $\sim 20 \text{ km s}^{-1}$ with minimal velocity gradients (J. Baek et al. 2022), although beam smearing of adjacent clouds likely still appreciably broadens the line intrinsic FWHM. In cool-core BCGs, such patchy and filamentary multi-phase gas structures are typical of chaotic cooling of the galactic and circumgalactic medium that feeds episodic accretion with much higher $\dot{M}_{\text{BH}}/\dot{M}_{\text{Edd}}$ (e.g., I. V. Babyk et al. 2019; M. Gaspari et al. 2020; T. Pasini et al. 2021).

For M87 specifically, A. Simionescu et al. (2018) used ALMA imaging to map out CO emission from the dense SE molecular cloud that is embedded within a broader filamentary atomic gas complex $\sim 40''$ from the nucleus with projected $v_{\text{LOS}} - v_{\text{sys}} \sim -129 \text{ km s}^{-1}$. The SE cloud shows a modest gradient of at least a couple $\times 10 \text{ km s}^{-1}$ across the brightest emission-line clump that extends over a projected $\sim 150 \text{ pc}$. At an angular resolution of $\theta_{\text{FWHM}} \sim 1.''4 \times 0.''7$ (average $\sim 85 \text{ pc}$), the gas cloud with $S_{\text{CO}(2-1)}\Delta v = 0.56 \pm 0.06 \text{ Jy km s}^{-1}$ and $v_{\text{LOS}} - v_{\text{sys}} \sim -129 \text{ km s}^{-1}$ is resolved into a spherical clump with a diameter of $\sim 100 \text{ pc}$ and $\sigma_{\text{LOS}} \sim 30 \text{ km s}^{-1}$ together with a smaller, filamentary component with a narrower line width. The latter better matches the observed line widths and low velocity gradient from the CO absorption shown in Figure 4. Based on the relative distribution of ionized gas and X-ray emission, those authors argue the SE cloud is falling into M87 from behind, with the observed molecular gas surviving passage through the moderately cool-core X-ray gas in this part of the Virgo cluster (R. Shibata et al. 2001; W. Forman et al. 2007) only to be destroyed at closer radii either by shocks or by relativistic particles associated with the radio lobes.

We first explore the gravitationally bound cloud scenario. Assuming Galactic cloud size-line width correlations apply (Larson’s relations; e.g., P. M. Solomon et al. 1987; R. Shetty et al. 2012; T. Wong et al. 2022), the fitted CO absorption-line $\bar{\sigma}_{\text{LOS}} = 4.65 \pm 0.47 \text{ km s}^{-1}$ suggests a radius $r_{\text{cloud}} \sim 30\text{--}40 \text{ pc}$. Infrequently, extragalactic CO imaging resolves emission-line clouds in CNDs (e.g., D. Utomo et al. 2015; E. Rosolowsky et al. 2021) but these studies tend to be sensitive only to more turbulent giant molecular clouds. For other luminous ETGs, gas-dynamical modeling of ALMA CO imaging even suggests higher typical intrinsic turbulent velocity dispersions ($\sim 5\text{--}15 \text{ km s}^{-1}$; e.g., A. J. Barth et al. 2016; B. D. Boizelle et al. 2019; E. V. North et al. 2019; however, c.f. T. A. Davis et al. 2017). Scaling Larson’s relation to fit these extragalactic clouds could give r_{cloud} as low as $\sim 5 \text{ pc}$. For a virialized cloud with $\alpha_{\text{vir}} \equiv 5\sigma^2/\pi GR\Sigma = 1$, the upper r_{cloud} size and measured $\bar{\sigma}_{\text{LOS}}$ would suggest a gas surface mass density $\Sigma_{\text{H}_2} \gtrsim 100 M_{\odot} \text{ pc}^{-2}$ that is implausibly high based on CO non-detection discussed in Section 4.1.

More likely, this CO absorption originates in a foreground filament. Simulations suggest that accreting clouds like those composing the SE complex or the dense dusty clump are preferentially drawn into narrow filaments by magnetic fields that thread massive galaxies (e.g., M. Fournier et al. 2024).

In Galactic systems, resolved filamentary structures seen in emission have typical line widths $\lesssim 1 \text{ km s}^{-1}$ and narrow core widths $r_c \lesssim 0.1 \text{ pc}$ (wherein the n_{H_2} is uniform; e.g., D. Arzoumanian et al. 2011; E. W. Koch & E. W. Rosolowsky 2015; G. V. Panopoulou et al. 2016; A. Rivera-Ingraham et al. 2016; R. Indebetouw et al. 2020). For the measured $\bar{\sigma}_{\text{LOS}}$, filament size-emission-line width relations would be consistent with an effective $r_c \sim 0.5 \text{ pc}$ or more, which is at the very upper limit for Galactic filaments. However, the environment surrounding the M87 nucleus is very different than for MW filaments. We note that within and around radio galaxies, even wider filaments reaching $\sim \text{kpc}$ scales have been observed (F. Yusef-Zadeh et al. 2022).

4.2.2. Column Densities and Masses

The estimated $N_{\text{CO}} \sim 10^{15} \text{ cm}^{-2}$ is below the detection threshold for many extragalactic ALMA programs, although it is reached by certain Galactic line surveys (e.g., H. S. Liszt & R. Lucas 1998). A standard CO/H₂ abundance ratio of 3.2×10^{-4} (U. J. Sofia et al. 2004; A. D. Bolatto et al. 2013) would result in a very low $N_{\text{H}_2} \sim 1.5 \times 10^{18} \text{ cm}^{-2}$. That conversion factor is typically applied to systems with peak $N_{\text{H}_2} \gtrsim 10^{21} \text{ cm}^{-2}$ while such a low N_{CO} better comports with more diffuse Galactic lines of sight that have CO/H₂ abundances of $\sim 2 \times 10^{-6}$ (H. Liszt et al. 2019) to $\sim 8 \times 10^{-7}$ (J. L. Pineda et al. 2010) due to easier CO destruction. These ratios result in our preferred range $N_{\text{H}_2}/10^{20} \text{ cm}^{-2} = 0.92^{+0.68}_{-0.36} - 2.3^{+1.7}_{-0.9}$ that matches an estimated total $N_{\text{H}} \sim (2-5) \times 10^{20} \text{ cm}^{-2}$ towards the M87 nucleus from X-ray spectroscopy (e.g., A. S. Wilson & Y. Yang 2002; T. Di Matteo et al. 2003). The corresponding $\Sigma_{\text{H}_2} \sim 0.7-2 M_{\odot} \text{ pc}^{-2}$ is far below the $\gtrsim 10^{2.3} M_{\odot} \text{ pc}^{-2}$ threshold needed to reconcile the measured $\bar{\sigma}_{\text{LOS}}$ with a larger ($r_{\text{cloud}} = 30 \text{ pc}$) virialized system. This column density range is also much lower than typical Galactic filament peak N_{H_2} (D. Arzoumanian et al. 2011, 2018; V. Könyves et al. 2020) but better matches properties of extragalactic filamentary structures (e.g., R. Sancisi et al. 2008; W. J. G. de Blok et al. 2014). Also, it is consistent with estimated N_{H_2} ranges for a filamentary obscurer that matches the intrinsic extinction of the dense and filament regions (see Section 4.1), especially if the nucleus probes a line of sight for N_{CO} that is slightly offset from the peak dust obscuration.

The physical state (n_{H_2} , T_K) of the absorber remains uncertain. For a single cloud centered on the nucleus, this preferred N_{H_2} range and a broad $r_{\text{cloud}} \sim 5-30 \text{ pc}$ would correspond to a line-of-sight average $\bar{n}_{\text{H}_2} \sim 0.5-7.5 \text{ cm}^{-3}$ with a total $M_{\text{H}_2} \sim 200-3000 M_{\odot}$. For comparison, the more compact SE cloud region has an estimated $\bar{n}_{\text{H}_2} \sim 50 \text{ cm}^{-3}$. Adopting typical cloud radial density profiles and small core sizes ($\sim 0.1 \text{ pc}$; e.g., T. Csengeri et al. 2017; P. J. André et al. 2022) relative to the outer $r_{\text{cloud}} = 5-30 \text{ pc}$, the expected central densities of $100-1500 \text{ cm}^{-3}$ would be lower than both typical dense gas cores and the CO(1-0) critical density (as opacity $\tau \ll 1$; N. Z. Scoville 2013). A compact $r_c \lesssim 0.1 \text{ pc}$ would suggest a line-of-sight $\bar{n}_{\text{H}_2} \gtrsim 60-150 \text{ cm}^{-3}$.

Instead, the CO absorption may arise from chance alignment with a filament. By calculating \bar{n}_{H_2} through the cen-

ter of a Plummer filament model with total N_{H_2} above (A. Rivera-Ingraham et al. 2016), the peak H₂ densities should reach *at least* $1000-2500 \text{ cm}^{-3}$, which is consistent with simulations of filament formation (P. Hennebelle 2013). If $r_c \sim 0.1 \text{ pc}$, the corresponding linear mass $M_{\text{H}_2}/\ell \sim 0.5-1 M_{\odot} \text{ pc}^{-1}$ would be at the very bottom of the linear mass distribution for Galactic systems associated with star formation (R. Sancisi et al. 2008), although it does match better more diffuse extragalactic filaments associated with accretion (e.g., W. J. G. de Blok et al. 2014). If positioned off-center from the M87 nucleus, such a filament would allow for higher peak n_{H_2} and M_{H_2}/ℓ values.

Simulations suggest CO is created (or persists in an equilibrium state) for gas with $n_{\text{H}_2} \gtrsim 1000 \text{ cm}^{-3}$ where dust, H₂, and line self-shielding prevents CO dissociation (C. Safraneck-Shrader et al. 2017), in better agreement with the filament scenario. However, the low $N_{\text{H}_2} \sim 10^{20} \text{ cm}^{-2}$ and estimated $A_V \sim 0.04-0.10 \text{ mag}$ suggests more limited shielding against interstellar radiation (N. Y. Gnedin & B. T. Draine 2014). Similar to the SE complex, the CO-absorbing gas may be physically located far from the nucleus and evolving (further) towards atomic gas dominance. The low molecular gas fraction inferred from this A_V range ($f_{\text{H}_2} \sim 0.1$; T. P. Snow & B. J. McCall 2006) would make C II and not C I or CO the dominant reservoir of gas-phase carbon (M. Gerin et al. 2024). Far-IR spectroscopy centered about the M87 nucleus does reveal faint [C II] $158 \mu\text{m}$ and [O I] $63 \mu\text{m}$ fine-structure lines (J. R. Brauher et al. 2008), but the $\sim 1.7'$ aperture diameter (and possible $1'$ offset from the nucleus) prevents any clear connection to any specific gaseous structure. Adding neutral atomic gas with an estimated $N(\text{H}) = 2N(\text{H}_2) \times (1-f_{\text{H}_2})/f_{\text{H}_2} \sim (2-4) \times 10^{21} \text{ cm}^{-2} \sim 15-30 M_{\odot} \text{ pc}^{-2}$ would lower α_{vir} but likely not enable the gas cloud to be gravitationally bound.

Instead, interactions with the hot interstellar medium or an envelope of warm, partially ionized gas may provide pressure support to the CO absorber. In the first case for an isothermal X-ray-emitting distribution, the lower-bound electron density $n_e \sim 0.5 \text{ cm}^{-3}$ and temperature $kT_e \sim 1.5-2 \text{ keV}$ ($T_e/10^6 \text{ K} \sim 15-25$; W. B. Sparks et al. 2004; W. Forman et al. 2007) give rise to a pressure $P \gtrsim (1-2) \times 10^{-9} \text{ dynes cm}^{-2}$. In the second case, warm ionized gas with $T_e \sim 10^4 \text{ K}$ and higher $n_e \sim 1600 \text{ cm}^{-3}$ (H. C. Ford & H. Butcher 1979) would provide similar external pressure (see also T. M. Heckman et al. 1989). For comparison, the cloud or filament scenarios with their corresponding \bar{n}_{H_2} and a low $T_K \sim 25-50 \text{ K}$ results in internal $P \ll 10^{-10} \text{ dynes cm}^{-2}$, leading to pressure confinement of the diffuse molecular gas.

4.2.3. Molecular Gas Sensitivity and Temperature

The measured $T_{\text{ex}}^{21} \sim 8 \pm 2 \text{ K}$ is similar to excitation temperatures found for certain extragalactic and diffuse Galactic molecular gas (e.g., H. Liszt & R. Lucas 2004; J. Roman-Duval et al. 2010). Some massive galaxies have diffuse obscurers with $T_{\text{ex}} \sim 20-40 \text{ K}$ (F. P. Israel 1992; J. Lim et al. 2017; T. Rose et al. 2019a,b) while outflow CO line ratios or warmer molecular tracers suggest $T_{\text{ex}} \sim 30-100 \text{ K}$ and

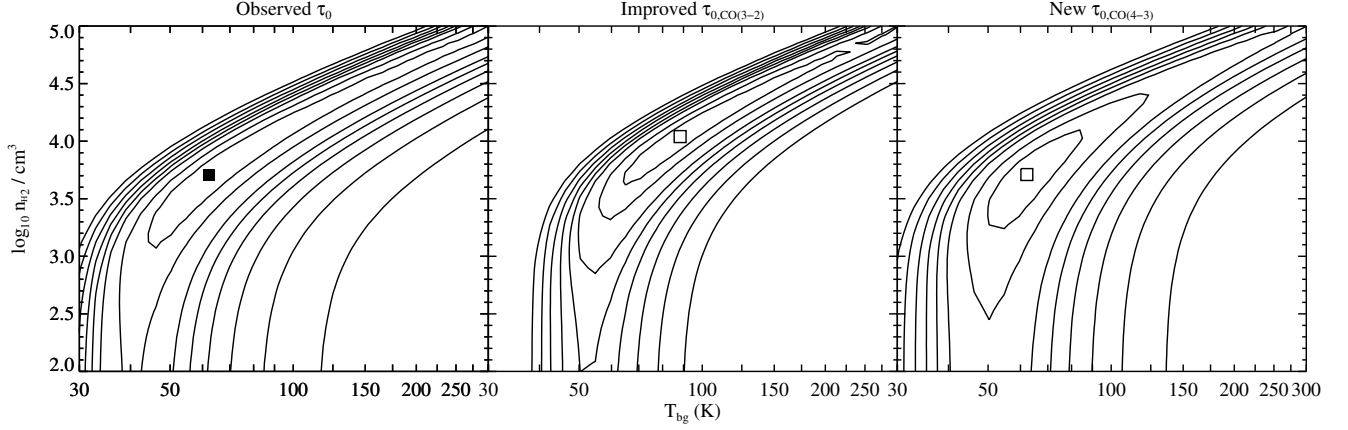


Figure 6. *radex* radiative transfer modeling results (with $T_K = 10$ K, CO FWHM = 10 km s^{-1}) applied to measured (Table 2; *left panel*) or augmented peak opacities, including an improved $\tau_{0,\text{CO}(3-2)}$ (*middle*) or a new $\tau_{0,\text{CO}(4-3)}$ value (*right*). New τ_0 are assumed to reach S/N ~ 3.4 , and the $\tau_{0,\text{CO}(4-3)}$ value is predicted for the best-fitting n_{H_2} and T_{bg} (*left*; see also Figure 5). Inner $\Delta\chi^2$ contours are at the 1, 2, and 3σ level while the remainder are arbitrarily (but linearly) spaced. Either of these new data sets would close the confidence interval, although CO(4–3) observations have the potential to provide the tightest constraints on n_{H_2} and T_{bg} .

$T_K \sim 400$ K, respectively (K. M. Dasyra et al. 2016; F. H. Cashman et al. 2021; I. Ruffa et al. 2022). Because of the intense interstellar radiation field and cosmic ray environment, the CO absorber is likely to be out of LTE. Indeed, both the measured $\tau_{\text{CO}(3-2)}$ and inferred $T_{\text{ex}}^{32} \sim 30 \pm 20$ K are elevated over LTE predictions from lower- J CO measurements.

To probe more realistic cloud conditions, we employed the one-dimensional non-LTE radiative transfer code *radex* (G. J. Ferland et al. 1998; F. F. S. van der Tak et al. 2007) to reproduce the observed peak opacities $\bar{\tau}_{0,\text{CO}(1-0)}$, $\bar{\tau}_{0,\text{CO}(2-1)}$, and $\tau_{0,\text{CO}(3-2)}$. Radiative transfer modeling typically relies on multiple molecular line tracers and/or isotopologues to probe dense gas conditions. In this case, however, the very low opacity $\tau_{0,\text{CO}} \ll 1$ simplifies the analysis and allows ^{12}CO to trace the entire cloud. To be consistent with observations, we adopted $N_{\text{CO}} = 10^{15} \text{ cm}^{-2}$ from LTE measurements and fixed the CO line FWHM = 10 km s^{-1} . The level of gas turbulence is not known, but we assumed a cold gas distribution and tested $T_K = 10$ K and 30 K in turn. During *radex* modeling, we explored $n_{\text{H}_2} = 10^2 - 10^5 \text{ cm}^{-3}$ and background temperature $T_{\text{bg}} = 30 - 300$ K. In Figure 5, we compare measured and *radex* model τ_0 values and present χ^2 contours over these two variables. These results show strong preference for a very cold $T_K = 10$ K with best-fitting $n_{\text{H}_2} \sim 5100 \text{ cm}^{-3}$ and $T_{\text{bg}} \sim 62$ K. While the 1σ contours do not close for reasonable n_{H_2} and T_{bg} values, they provide $n_{\text{H}_2} > 1100 \text{ cm}^{-3}$ and $T_{\text{bg}} > 45$ K lower limits. A warmer $T_K = 30$ K gives much higher best-fit $n_{\text{H}_2} \approx 3.5 \times 10^4 \text{ cm}^{-3}$ and $T_{\text{bg}} \sim 71$ K with $7\times$ higher χ^2 ; still, lower-bound parameter limits are similar to the $T_K = 10$ K case. Based on these *radex* bounds, the current CO absorption-line data appear more consistent with central $n_{\text{H}_2} > 1000 \text{ cm}^{-3}$ for a thin filament ($r_c < 0.1$ pc) instead of a more diffuse filament or spherical cloud.

Additional higher-frequency ALMA 12-m imaging would likely break the degeneracy between n_{H_2} and T_{bg} . We tested two cases: one that improved the existing $\tau_{0,\text{CO}(3-2)}$ measure-

ment and the other that obtained new Band 8 imaging to detect $\tau_{0,\text{CO}(4-3)}$. In both cases, we assumed that the new peak opacity reached the same fractional precision as the Xa1 $\tau_{0,\text{CO}(1-0)}$ measurement (S/N ~ 3.4). In Figure 6, these *radex* results show closed 1σ confidence intervals in both cases, although adding in the CO(4–3) measurement to the values in Table 2 provides much tighter constraints. In the best case, n_{H_2} and T_{bg} could be known to within ~ 0.3 dex and 10–20 K, respectively. Using the OT, we estimate these new τ_0 measurements would require a minimum on-source (total) time of 56 min (112 min) for the Band 7 imaging while for Band 8 the require time would be up to 6.25 hrs (12.1 hrs).

5. CONCLUSION

We conducted a CO line search of M87 using archival ALMA 12-m imaging, focusing on the CND and the dusty clouds and filaments seen in optical imaging in the inner \sim kpc. Despite the deep ALMA imaging and multiple spws containing redshifted CO transitions, we did not clearly identify any CO emission. Over the atomic gas CND, the upper limit $M_{\text{H}_2} < 2.3 \times 10^5 M_\odot$ is $\sim 20\times$ lower than achieved in previous CO surveys. In other regions containing atomic gas filaments and dust, we placed upper limits of $M_{\text{H}_2} \lesssim 10^5 - 10^6 M_\odot$ with a global $< 4 \times 10^6 M_\odot$ limit for a circular aperture with $R < 2$ kpc. In narrow gaseous regions, potential CO emission-line signatures in extracted line profiles do not arise from compact sources.

During this search, we confidently detected molecular gas in absorption against the bright nucleus in the CO(1–0), CO(2–1), and CO(3–2) transitions. The absorber has very low opacity with average peak $\bar{\tau}_{0,\text{CO}(1-0)} = 0.00239 \pm 0.00054$ and integrated $\bar{\tau}_{\text{CO}(1-0)} = 0.0281 \pm 0.0045 \text{ km s}^{-1}$. Measured opacities are slightly higher values for the higher- J absorption lines. Line fitting showed a consistently narrow, slightly blueshifted feature with average $\bar{v}_{\text{LOS}} - v_{\text{sys}} \sim -77.2 \pm 0.4 \text{ km s}^{-1}$ and $\bar{\sigma}_{\text{LOS}} \sim 4.7 \pm 0.5 \text{ km s}^{-1}$. From

multiple low-S/N CO absorption lines we calculated column densities $N_{\text{CO}} = (1.16_{-0.28}^{+0.21}) \times 10^{15} \text{ cm}^{-2}$ and $N_{\text{H}_2}/10^{20} \text{ cm}^{-2} = 0.92_{-0.36}^{+0.68} - 2.3_{-0.9}^{+1.7}$ (1σ uncertainties) assuming the gas is in a diffuse molecular phase. These molecular absorption features appear inconsistent with blueshifted atomic gas absorption detected in UV/optical spectroscopy at a relative speed of about -130 km s^{-1} with line FWHM $\lesssim 300 \text{ km s}^{-1}$, and we disfavor interpreting this CO absorber as arising from molecular gas entrained in an outflow.

Instead, the CO absorption-line properties are more consistent with an optically thin ($A_V < 0.5 \text{ mag}$) dusty cloud or filament in a chance alignment with the AGN core, like those seen close in projection to the nucleus. Based on opacity measurements, LTE relations suggest the molecular gas is cold with excitation temperatures $T_{\text{ex}}^{21} = 7.77_{-1.94}^{+1.34} \text{ K}$ (1σ) and $T_{\text{ex}}^{32} \sim 30 \text{ K}$, hinting at a $J = 2$ population that is elevated over LTE predictions. Non-LTE radiative transfer modeling finds much better agreement with the observed τ_0 values. The `radex` output prefers low kinematic temperature $T_k \sim 10 \text{ K}$ and more dense $n_{\text{H}_2} \sim 5000 \text{ cm}^{-3}$, surrounded by a hotter background radiation field with $T_{\text{bg}} \sim 60 \text{ K}$. This (uniform) n_{H_2} estimate better matches expectations for a thin, pressure-confined filament, perhaps viewed slightly offset from the compact core location.

ACKNOWLEDGMENTS

We thank the anonymous reviewer for helpful suggestions. We also thank Aaron Barth, Andrew Baker, Jeremy Darling, and Luis Ho for advice and encouragement. We are grateful for advice from Ivan Marti-Vidal, Ciriaco Goddi, and Hiroshi Nagai, together with the ALMA NAASC, in dealing

with APP-mode ALMA data sets and bandpass calibration limitations.

Partial support for this work was provided by the NSF through award SOSPADA-003 from the NRAO. XL, NL, BJD, and JD thank the Brigham Young University College of Computational, Mathematical, and Physical Sciences and the Department of Physics and Astronomy for additional research funding.

This research is based, in part, on observations made with the NASA/ESA Hubble Space Telescope obtained from the Space Telescope Science Institute, which is operated by the Association of Universities for Research in Astronomy, Inc., under NASA contract NAS 5-26555. These observations are associated with programs GO-12271 and GO-14256. This paper makes use of the following ALMA data in ADS/JAO.ALMA# codes: 2011.0.00001.CAL, 2012.1.00661.S, 2013.1.00073.S, 2013.1.01022.S, 2015.1.00030.S, 2015.1.01170.S, 2015.1.01352.S, 2016.1.00021.S, 2016.1.01154.V, 2017.1.00608.S, 2017.1.00841.V, 2017.1.00842.V, 2019.1.00807.S, and 2021.1.01398.S. ALMA is a partnership of ESO (representing its member states), NSF (USA) and NINS (Japan), together with NRC (Canada), NSTC and ASIAA (Taiwan), and KASI (Republic of Korea), in cooperation with the Republic of Chile. The Joint ALMA Observatory is operated by ESO, AUI/NRAO and NAOJ. The National Radio Astronomy Observatory is a facility of the National Science Foundation operated under cooperative agreement by Associated Universities, Inc.

Facilities: HST (ACS,WFC3), ALMA, ACA

Software: CASA (J. P. McMullin et al. 2007), GALFIT (C. Y. Peng et al. 2002), `radex` (F. F. S. van der Tak et al. 2007), ALMA OT (K. Immer et al. 2024), PlotDigitizer (Porbital 2024)

APPENDIX

A. CONTINUUM PROPERTIES

A.1. MFS imaging

Representative ALMA 12-m MFS imaging in Figure 2 have average synthesized beam FWHM ranging from $\sim 2''.3$ in a more compact configuration to just ~ 32 (~ 24) mas using robust (uniform) weighting of the configuration 8/7 data, which is the most extended ALMA configuration applied to the M87 nucleus to date. In compact configurations, these mm-wavelength images capture the approaching jet and the double radio lobes, albeit with significantly less sensitivity to fainter features observed in traditional radio bands. On the smallest scales, Band 6 data partially resolve the central continuum to reveal a collimated jet that is prominent in both lower-frequency VLBI and HST imaging (e.g., see M. J. Reid et al. 1989; J. A. Biretta et al. 1999; R. C. Walker et al. 2018). Intermediate-resolution data resolve previously identified clumps in the approaching jet, including features A–F and I. At high resolution, Band 6 imaging isolates features M (sometimes referred to as L) and N1 that lie closer to the nucleus. The N2 clump seen in VLBI data is only detected by ALMA as a slight elongation from the core when using uniform weighting. Notably, the highest-resolution ALMA data do not reveal (or are not sufficiently sensitive to detect) diffuse non-thermal emission beyond M that leads into the superluminal HST-1 clump at a distance of $\sim 1''$ (M. Giroletti et al. 2012; J. Park et al. 2019).

We fit the highest-resolution Band 6 MFS image in the X2c2 data set (with uniform weighting; $\theta_{\text{maj}} \times \theta_{\text{min}} = 27 \times 21 \text{ mas}$, averaging to $\sim 2 \text{ pc}$) using the `CASA imfit` task. In addition to the nuclear source, this image-plane fit included an additional,

Table A1. M87 ALMA 12-m Observations and Imaging Properties

Obs. Date	Member OUS	ν_{obs} (GHz)	$\Delta\nu_{\text{obs}}$ (MHz)	Baselines (km)	$\theta_{\text{maj}} \times \theta_{\text{min}}$ θ_{PA}	MRS (arcsec)	Time (hrs)	Peak S_{ν} (Jy)	MFS rms (mJy beam $^{-1}$)	PWV (mm)	Pol.
(1)	(2)	(3)	(4)	(5)	(6)	(7)	(8)	(9)	(10)	(11)	(12)
2012.1.00661.S (PI: Vlahakis)											
2014 7 Mar	A002/X6444ba /X1b0	99.90–101.89	15.63	0.015–0.423	$2''.03 \times 1''.42$ 60.2°	12.5	1.71	2.10	1.81	1.41	XX YY
		101.78–103.76	15.63								
		111.92–113.91	15.63								
2014 28 Jan	A002/X6444ba /X1b4	113.85–115.72	0.49	0.015–0.347	$1''.16 \times 0''.60$ -83.7°	6.04	1.89	1.01	0.104	0.97	XX YY
		331.50–333.48	15.63								
		333.30–335.29	15.63								
		343.41–345.28	9.77								
		345.30–347.29	15.63								
2013.1.00073.S (PI: Tan)											
2015 14 Jun	A001/X12f /X20f	213.00–214.99	15.63	0.021–0.784	$0''.54 \times 0''.44$ -47.8°	4.04	0.25	1.75	1.10	0.69	XX YY
		215.00–216.99	15.63								
		228.63–230.50	0.49								
2015 16 Aug	A001/X12f /X20d	230.57–232.56	15.63	0.043–1.574	$0''.27 \times 0''.22$ 14.3°	1.88	0.50	0.93	1.99	0.74	XX YY
		213.00–214.99	15.63								
		215.00–216.99	15.63								
		228.63–230.50	0.49								
		230.57–232.56	15.63								
2013.1.01022.S (PI: Asada)											
2015 19 Sep	A001/X13a /Xbe	89.51–91.48	31.25	0.041–2.070	$0''.46 \times 0''.38$ 30.0°	23.8	3.32	2.47	0.27	1.56	XX XY YX YY
		91.45–93.42	31.25								
		101.51–103.48	31.25								
		103.51–105.48	31.25								
2015.1.00030.S (PI: Vlahakis)											
2015 8 Nov	A001/X2d8 /X5	99.88–101.86	15.63	0.085–16.20	$0''.10 \times 0''.046$ -56.5°	0.97	0.66	1.96	0.51	0.96	XX YY
		101.87–103.86	15.63								
		112.28–114.16	0.98								
		113.85–115.72	0.98								
2015.1.01170.S (PI: Asada)											
2015 11 Nov	A001/X2df /X135	89.50–91.47	31.25	0.085–16.20	$0''.07 \times 0''.05$ 34.8°	0.88	2.29	1.94	0.34	1.34	XX XY YX YY
		91.44–93.41	31.25								
		101.50–103.47	31.25								
		103.50–105.47	31.25								
2015.1.01352.S (PI: Doi)											
2015 27 Oct	A001/X2d6 /X2ba	89.50–91.48	15.63	0.253–16.20	$0''.06 \times 0''.05$ 39.3°	0.90	0.034	1.75	0.69	0.97	XX YY
		91.43–93.42	15.63								
		101.50–103.48	15.63								
2015 31 Oct	A001/X2d6 /X2be	103.50–105.48	15.63	0.068–15.24	$0''.06 \times 0''.05$ -37.2°	0.72	0.36	1.72	0.35	1.81	XX YY
		136.99–138.98	15.63								
		138.93–140.91	15.63								
2015 31 Oct	A001/X2d6 /X2c2	148.99–150.98	15.63	0.068–15.24	$0''.03 \times 0''.03$ -35.1°	1.34	0.22	1.25	0.47	1.24	XX YY
		150.99–152.98	15.63								
		222.99–224.98	15.63								
		224.99–226.98	15.63								
		238.98–240.97	15.63								
		240.98–242.97	15.63								

NOTE—Properties of ALMA 12-m interferometric and phased-array (APP; .V) mode data sets that were centered on the M87 nucleus, with the project code and Principle Investigator listed above each synopsis. Cols. (1) and (2) give the UT observation date for each member OUS, respectively, while cols. (3) and (4) give the frequency coverage of each spectral window (spw) along with the associated channel binning. For FDM spws, online Hanning smoothing decreases the effective spectral resolution by a factor of up to two. Unprojected baseline ranges in col. (5) give rise to the corresponding synthesized beam parameters from the final MFS image in col. (6) and the maximum recoverable scale (MRS; adopted from the ALMA Science Archive) in col. (7). Col. (8) reports the on-source integration times, including latencies. Cols. (9) and (10) give the peak continuum flux density and rms of the MFS image at the average frequency for the four spws after applying self-calibration loops, if possible. Col. (11) gives the average precipitable water vapor (PWV; adopted from the ALMA Science Archive) over that time interval. Col. (12) reports the dual (XX YY) or cross-polarization (XY YX) setup.

Table A1. M87 ALMA 12-m Observations and Imaging Properties

Obs.	Member	ν_{obs}	$\Delta\nu_{\text{obs}}$	Baselines	$\theta_{\text{maj}} \times \theta_{\text{min}}$	MRS	Time	Peak S_{ν}	MFS rms	PWV	Pol.
Date	OUS	(GHz)	(MHz)	(km)	θ_{PA}	(arcsec)	(hrs)	(Jy)	(mJy beam $^{-1}$)	(mm)	
(1)	(2)	(3)	(4)	(5)	(6)	(7)	(8)	(9)	(10)	(11)	(12)
2016.1.00021.S (PI: Vlahakis)											
2017 15 Aug	A001/X899 /Xa1	112.00–113.99	15.63	0.021–3.64	$0''.22 \times 0''.21$ -64.8°	3.16	1.59	1.73	0.37	0.57	XX YY
		112.62–114.49	0.98								
		113.85–115.72	0.98								
		114.04–115.91	0.98								
2016.1.01154.V (PI: EHT Consortium)											
2017 5 Apr	A001/X11a7 /X3a	212.17–214.04	7.81	0.015–0.375	$2''.10 \times 1''.98$ -82.0°	12.87	1.22	1.18	1.02	0.81	XX XY YX YY
		214.17–216.04	7.81								
		226.17–228.04	7.81								
		228.17–230.04	7.81								
2017 6 Apr	A001/X11a7 /X3c	212.17–214.04	7.81	0.015–0.279	$2''.17 \times 1''.50$ -76.0°	9.95	0.89	1.14	0.54	0.69	XX XY YX YY
		214.17–216.04	7.81								
		226.17–228.04	7.81								
		228.17–230.04	7.81								
2017 11 Apr	A002/Xbee37d /Xb	212.17–214.04	7.81	0.015–0.161	$1''.18 \times 0''.80$ 70.5°	12.90	1.69	1.32	1.14	1.11	XX XY YX YY
		214.17–216.04	7.81								
		226.17–228.04	7.81								
		228.17–230.04	7.81								
2017.1.00608.S (PI: Marti-Vidal)											
2018 25 Sep	A001/X129e /X1d	211.51–213.48	31.25	0.015–1.398	$0''.41 \times 0''.26$ -53.1°	3.70	0.58	0.93	1.68	0.77	XX XY YX YY
		213.51–215.48	31.25								
		227.51–229.48	31.25								
		229.51–231.48	31.25								
2017.1.00841.V (PI: Doeleman)											
2018 20 Apr	A001/X12d1 /X25	212.17–214.04	7.81	0.015–0.418	$0''.89 \times 0''.79$ 46.1°	7.66	1.78	0.709	2.95	2.06	XX XY YX YY
		214.17–216.04	7.81								
		226.17–228.04	7.81								
		228.17–230.04	7.81								
2018 21 Apr	A001/X12d1 /X27	212.17–214.04	7.81	0.015–0.418	$0''.95 \times 0''.75$ 40.6°	7.66	1.29	0.72	3.15	2.10	XX XY YX YY
		214.17–216.04	7.81								
		226.17–228.04	7.81								
		228.17–230.04	7.81								
2018 24 Apr	A001/X12d1 /X255	212.17–214.04	7.81	0.015–0.418	$0''.88 \times 0''.82$ 11.0°	7.66	1.68	0.84	2.27	2.67	XX XY YX YY
		214.17–216.04	7.81								
		226.17–228.04	7.81								
		228.17–230.04	7.81								
2017.1.00842.V (PI: Lu)											
2018 14 Apr	A001/X12d0 /Xe	85.34–87.20	7.81	0.015–0.372	$2''.57 \times 1''.99$ 4.3°	19.39	1.51	1.38	0.73	2.88	XX XY YX YY
		87.34–89.20	7.81								
		97.40–99.26	7.81								
		99.34–101.20	7.81								

NOTE—cont.

offset elliptical Gaussian to characterize the N2 clump that is not fully separate from the nuclear light at this resolution. As is shown in Figure 2, residuals from this two-component model fit do not support any additional sources within the inner 50 mas with a background rms of ~ 0.83 mJy beam $^{-1}$. The residual noise only marginally improves after uv -plane subtraction of the central point source using the CASA `uvmodelfit` task. In the image-plane fit, the dominant source is identical to the synthesized beam while the N2 component has observed FWHM axes of 49.5×18.5 mas, appearing to be resolved only in the jet direction along a PA = -75.6° . While heavily affected by beam smearing, the N2 component centroid is offset from the nucleus by $(\Delta R.A., \Delta \text{decl.}) = (-20.0, +5.3)$ mas, which is consistent within the formal `imfit` uncertainties to its location in 22 GHz

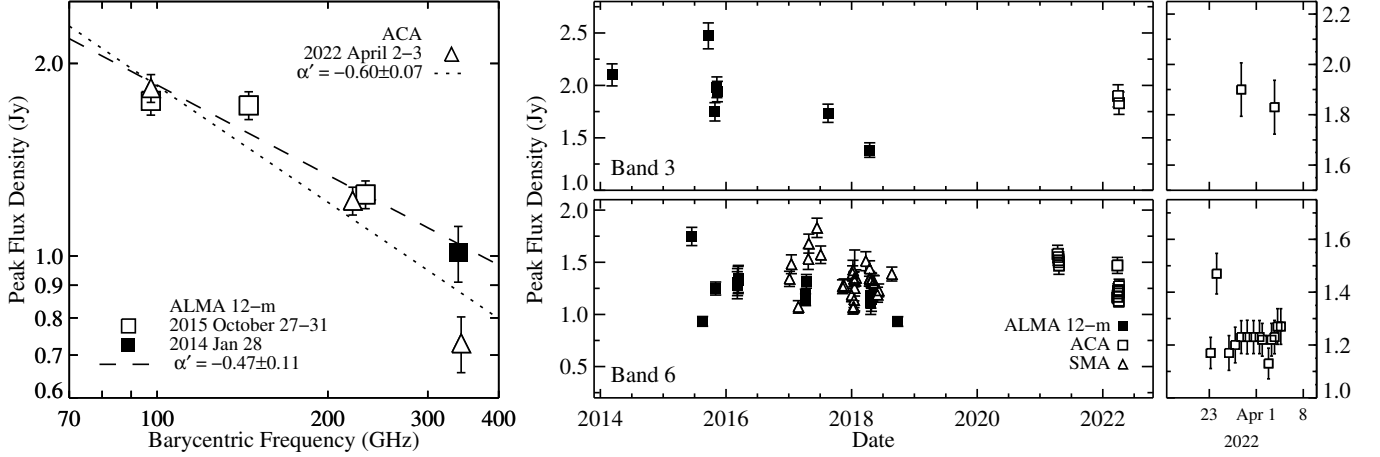


Figure B1. ALMA multi-Band peak flux densities of the M87 nucleus. The mm/sub-mm SED (*left panel*) focuses on more contemporaneous points, showing separate power-law fits to the ALMA 12-m and 7-m data points. The 12-m data were taken far enough apart that the factor of $\sim 2\times$ variability over \sim few-month to year timescales (*right panels*) somewhat dilutes its confidence. For the .V programs, peak flux densities were adopted from EHT ALMA-mode results (EHT MWL Science Working Group et al. 2021, 2024). ALMA Band 6 peak flux densities are consistent with the 1.3 mm light curve (spanning $\sim 1.2\text{--}2.3$ Jy) measured at earlier epochs using the Submillimeter Array (SMA; G. C. Bower et al. 2015).

imaging taken just a few months later (J. Park et al. 2019). The `imfit` components fitted to the core and the N2 clump have integrated flux densities of 1.220 Jy and 50.3 mJy, respectively, at 232.98 GHz.

A.2. Circumnuclear Dust

These ALMA continuum and spectral data provide additional constraints on heretofore unconfirmed circumnuclear dust. Global SED measurements are dominated by synchrotron emission for $\lambda \gtrsim 10 \mu\text{m}$, with the mid-IR nucleus SED showing some limited support for thermal continuum contributions from a small, cold dust distribution ($T_{\text{dust}} \sim 45\text{--}65$ K with an estimated total circumnuclear mass $M_{\text{dust}} < 200 M_{\odot}$; E. S. Perlman et al. 2001, 2007; M. Baes et al. 2010).

We had hoped that high-resolution mm/sub-mm wavelength continuum images would detect and disentangle the Rayleigh-Jeans tail of thermal emission from the synchrotron core and jet. Because the Band 6 `imfit` residuals shown in Figure 2 have no excess in the inner 50 mas (~ 4 pc; Figure 2) and are more smooth than the surrounding regions, we estimated an effective flux density upper limit by shifting a circular ($R = 0''.05$) aperture randomly to 100 continuum-free regions of the residual MFS image to sample the noise. The standard deviation $\delta S_{\text{ext}} = 0.75$ mJy of these extended integrations is an effective 1σ upper limit for any (resolved) thermal continuum emission (for additional discussion of practical noise recovery in ALMA imaging, refer to T. Tsukui et al. 2023). The enclosed dust mass limit

$$M_{\text{dust}} < \frac{\delta S_{\text{ext}} D_L^2}{\kappa_{\nu} B_{\nu}(T_{\text{dust}})} \quad (\text{A1})$$

assumes a standard dust absorption coefficient $\kappa_{850\mu\text{m}}$ and emissivity index $\beta = 2$ in the opacity relationship $\kappa_{\nu} = \kappa_{850\mu\text{m}}(\nu/352.7\text{GHz})^{\beta}$ (B. T. Draine 2003). For $T_{\text{dust}} = 25$ K and a standard dust-to-gas mass ratio of ~ 0.015 (K. M. Sandstrom et al. 2013), this modified black body $M_{\text{dust}} < 1.1 \times 10^4 M_{\odot}$ would correspond to a total gas mass $M_{\text{gas}} \lesssim 7.5 \times 10^5 M_{\odot}$. A hotter $T_{\text{dust}} \sim 100$ K that follows the upper dust temperature distribution in ETGs (T. Kokusho et al. 2019) would result in $M_{\text{dust}} < 2.3 \times 10^3 M_{\odot}$ and $M_{\text{gas}} < 1.5 \times 10^5 M_{\odot}$. In either case, this M_{dust} upper limit is not more constraining than is the SED fitting of mid-IR flux densities while the M_{gas} limit abuts against CO(1–0)-derived upper limits presented in Section 4.1.

Higher-frequency ALMA continuum imaging would better probe thermal emission as thermal S_{ext} increases with frequency roughly as ν^5 . In addition, the synchrotron nucleus intensity decreases towards higher frequencies with a spectral index $\alpha \sim -0.6$ (see Appendix B), further reducing δS_{ext} . DR limitations would dilute improvements due to higher S_{ext} and lower peak S_{ν} , with standard Bands 7 and 8 DR ~ 400 and 250, respectively. With good observing conditions and standard self-calibration, such observations could achieve a factor of $2\times$ higher DR in practice (G. Privon et al. 2024). Extreme DR imaging (~ 85000 in Band 3 and ~ 2500 in Band 7; S. Komugi et al. 2022) has been demonstrated with ALMA, although even in this best case and for the higher $S_{\text{ext, Band 7}}$ we estimate a maximal $\delta S_{\text{ext, Band 7}} \lesssim 0.5$ mJy would only probe $6\times$ lower M_{dust} than above.

Table A2. M87 ACA 7-m Observations and Imaging Properties

Obs. Date	Member OUS	$\bar{\nu}_{\text{obs}}$ GHz	$\bar{\theta}_{\text{FWHM}}$ (arcsec)	Time (min)	Peak S_{ν} (Jy)	MFS rms (mJy)	PWV (mm)	
(1)	(2)	(3)	(4)	(5)	(6)	(7)	(8)	
2019.1.00807.S (PI: Ramakrishnan)								
2021	Apr 11	A001/X1527/X2bc	221.10	6''94	7.55	1.58	83.1	1.62
	Apr 15	A001/X1527/X2bf	221.10	6''95	7.55	1.55	80.4	1.14
	Apr 17	A001/X1527/X2c2	221.10	6''96	7.55	1.52	79.7	0.69
	Apr 18	A001/X1527/X2c5	221.10	6''77	7.55	1.50	80.3	0.81
	Apr 19	A001/X1527/X2c8	221.10	8''65	7.55	1.47	85.8	0.81
2021.1.01398.S (PI: Ramakrishnan)								
2022	Mar 23	A001/X15bc/X6a5	221.10	6''05	7.55	1.17	59.1	1.00
	Mar 24	A001/X15bc/X6a8	221.10	4''69	7.55	1.47	76.8	0.26
	Mar 26	A001/X15bc/X6ae	221.10	6''95	7.55	1.20	65.8	0.81
	Mar 27	A001/X15bc/X6b1	221.10	6''03	5.02	1.23	67.4	0.76
	Mar 28	A001/X15bc/X7f8	97.50	14''68	7.55	1.90	106.1	2.16
	Mar 28	A001/X15bc/X6b4	221.97	6''34	7.55	1.23	62.2	2.11
	Mar 29	A001/X15bc/X6b7	221.10	6''64	7.55	1.23	63.8	2.27
	Mar 30	A001/X15bc/X6ba	221.10	6''31	7.55	1.23	62.4	1.19
	Mar 31	A001/X15bc/X6bd	221.10	6''72	7.55	1.23	62.9	1.36
	Apr 1	A001/X15bc/X6c0	221.10	6''76	7.55	1.22	62.0	0.30
	Apr 2	A001/X15bc/X26a	203.00	6''11	5.02	1.13	58.1	1.47
	Apr 2	A001/X15bc/X278	343.50	4''19	5.84	0.73	79.6	0.80
	Apr 2	A001/X15bc/X6c3	221.10	6''45	7.55	1.22	61.8	0.87
	Apr 3	A001/X15bc/X7fb	95.70	16''49	5.02	1.83	107.0	1.22
	Apr 3	A001/X15bc/X6c6	221.10	6''72	7.55	1.23	63.2	1.36
	Apr 4	A001/X15bc/X271	233.00	7''36	5.02	1.27	67.5	0.64

NOTE—Continuum properties of archival ACA 7-m data sets. Cols. (3) and (4) give the average frequency of the final MFS image across all spws and average synthesized beam FWHM from Briggs ($r = 0.5$) imaging. Col. (5) gives the on-source integration time while cols. (6) and (7) report the peak and rms intensities of each MFS image. Col. (8) reports average PWV conditions. Each project used the same $\Delta\nu_{\text{obs}} = 15.6$ MHz TDM channel binning with dual polarization set-up.

B. LIGHT CURVES AND SPECTRAL SLOPES

In addition to ALMA 12-m observations taken between 2014 to 2019, we retrieved additional ACA 7-m imaging in projects 2019.1.00807.S and 2021.1.01398.S that monitored the Band 3 and 6 variability of M87 around EHT campaigns in 2021 and 2022. We obtained these archival data and applied standard pipeline calibration followed by phase-only self-calibration prior to imaging into MFS images with typical limiting sensitivities of 60–80 mJy beam⁻¹. Despite the coarse angular resolution ($\bar{\theta}_{\text{FWHM}} \sim 5''$ in Band 6) relative to the 12-m data, we convolved an MFS image from project 2013.1.01022.S to match the ACA resolution and confirmed that higher beam sizes do not result in jet emission contaminating the peak flux densities reported in Table A2. To construct more complete light curves shown in Figure B1, we joined together ALMA 12 and 7-m peak flux densities with Submillimeter Array (SMA) monitoring of M87 over this time frame (EHT MWL Science Working Group et al. 2021, 2024).

From adjacent ACA observations in program 2021.1.01398.S that span ~ 100 –400 GHz, we measured an apparent mm/sub-mm spectral index $\alpha' = -0.60 \pm 0.07$ from roughly contemporaneous data taken between 2022 April 2–3. Fit errors include both rms and absolute flux scaling uncertainties. More separate ALMA 12-m imaging in programs 2012.1.00661.S and 2015.1.01352.S

were obtained in programs 2012.1.00661.S and 2015.1.01352.S between 2014 Jan 28 and 2015 October 27–31, respectively, with coverage spanning ~ 95 –340 GHz. From these data, we find a best-fit $\alpha' = -0.47 \pm 0.11$. Both spectral indices are consistent with the synchrotron origin for the radio-continuum data for the core and jet regions (e.g., J. A. Biretta et al. 1991; EHT MWL Science Working Group et al. 2021). The more contemporaneous of the ALMA 12-m peak flux densities hint at a flattening spectral slope at longer wavelengths, although we do not detect a transition to $\alpha > 0$ (seen in VLBI for $\lambda \gtrsim 3$ mm within $R < 0''.4$; M. A. Prieto et al. 2016).

At radio to mm wavelengths, the peak flux densities of the M87 nucleus can vary by over 50% over \sim few month timescales. Consistent with damped-random walk (DRW) variability, though, the typical level has remained consistent over a decade (V. A. Acciari et al. 2009; H. E. S. S. Collaboration et al. 2011; K. Hada et al. 2014; G. C. Bower et al. 2015). This strong variability at long wavelengths may introduce large uncertainties in the SED slope measured across a narrow frequency range. We tested the impact of using non-contemporaneous ALMA data by creating mock light curves in ALMA Bands 3, 6, and 7 whose variability was defined by the power spectral density (PSD) fits to other radio galaxies (from 43 GHz light curves with an average power-law PSD slope $\alpha_{\text{PSD}} = -1.4$; H.-M. Zhang et al. 2020). Following the methodology of D. Emmanoulopoulos et al. (2013), we simulated an ALMA Band 6 peak light curve spanning 2 yrs with a one-day cadence. Additional Bands 3 and 7 light curves were then created using a consistent (intrinsic) $\alpha_{\text{intr}} = -0.7$ at each time epoch. We evaluated the change in recovered α' relative to α_{intr} when the different Band measurements were separated by days to months. We added random, realistic noise drawn from a normal distribution following the absolute flux calibration uncertainties (E. Fomalont et al. 2014) to each synthetic flux density before calculating α' across these ALMA Bands. We then collected these α' for a given time separation across the entire synthetic light curve. The standard deviation of the $\alpha_{\text{intr}} - \alpha'$ values serves as a proxy for the total uncertainty $\delta\alpha'$ when using non-contemporaneous ALMA measurements. When synthetic measurements are separated by at most a few days, we find that $\delta\alpha' \sim 0.05$. When separated by a few weeks to a few months, $\delta\alpha'$ increases from ~ 0.15 to ~ 0.35 before flattening. As a result, including a peak $S_{\nu, \text{Band } 7}$ point taken over 1.5 years before the remaining closely-sampled ALMA 12-m data means the fitted $\alpha' = -0.47 \pm 0.11$ underestimates the true uncertainty by at least a factor of 2. We note that α' measured across broad radio (or radio-to-mm) frequency ranges will give more reliable spectral indices that are robust against DRW variability.

C. PEAK CONTINUUM SPECTRA

In Figure C2, we present peak flux density spectra of all member OUS listed in Table A1. The spectra show no strong molecular line features except for residual contamination from atmospheric ozone, which we discuss in Appendix D. Spectral shapes are not always consistent across all spws in a single setup or as a function of time. We attribute this to either limitations in the standard pipeline calibration process or assumptions about the calibrator spectral index.

ALMA bandpass and flux calibration typically rely on week to few-month cadence monitoring of bright AGN (with peak flux densities of ~ 0.1 –2 Jy) that are tied to Solar System standards (M. Bonato et al. 2019). For point-source AGN, mm-wavelength flux densities have a median $\sim 10\%$ variability amplitude over \sim year timescales (and larger at higher frequencies; e.g., E. M. Sadler et al. 2008; M. Bonato et al. 2019). Calibrator flux densities are updated in the ALMA Calibrator Source Catalogue (CSC) and are recorded in pipeline files for MS reconstruction. This approach does not always account for the power-law spectral index of a calibrator (reflected by the `spix` parameter in the `setjy` task) or `spix` variability. Bandpass and flux calibrators are overwhelmingly selected from radio quasars and BL Lac-type objects that show approximately flat spectral shapes as measured in L to C radio bands, although in ALMA Bands the mm/sub-mm spectral index α is often more characteristic of classical synchrotron radiation (including for some calibrators used in these programs; see Appendix B and M. Bonato et al. 2018).

In some cases, the pipeline calibration process adopted a non-zero `spix` based on a roughly contemporaneous spectral index measurement, but this was not uniform in the earlier ALMA Cycles. Within a single sideband, `spix` discrepancies led to inconsistencies in the relative flux densities in individual spws at the 1–2% level. For adjacent EBs separated by an hour, even when using the same calibrators, the inter-spw α value may change by up to $\sim 10\%$ (see Figure E6). The main outlier is the X20d data set, whose inter-spw α is much steeper than roughly contemporaneous ALMA Band 6 observations and SED slopes in Figure B1. We attribute these discrepancies to poor spw-dependent phase solutions during self-calibration. Over all spws for a given spectral setup, the typical inter-spw α after standard pipeline and self-calibration processes spans a broad range of -0.1 to -1.0 . Some of this scatter is likely attributable to the apparent flattening in peak S_{ν} for measurements where $\nu \lesssim 100$ GHz (see Figure B1 and M. A. Prieto et al. 2016). Intra-spw slopes are particularly unreliable (L. Francis et al. 2020b) due in large part to bandpass calibration limitations (see Appendix E.3).

D. ATMOSPHERIC MODELING

The deepest atmospheric absorption features (primarily water vapor) often set the frequency ranges for mm/sub-mm Bands. For Band 3, an O₂ line ($N = 1 - 1 J = 1 - 0$; $\nu_{\text{sky}} = 118.750$ GHz) limits coverage in practice to a topocentric $\nu_{\text{sky}} < 115.93$ GHz. As we demonstrate in Appendix E.3, this impacts the continuum subtraction reliability near CO(1–0) and may contribute to the spurious broad absorption or emission-line features. Pipeline calibration does correct for most of the H₂O and O₂ transmission drop. However, the spw nearest the broad H₂O feature centered at $\nu_{\text{sky}} = 325.15$ GHz in the X1b4 data set does show some residual spectral curvature due to water vapor in the first EB when the relative humidity decreases rapidly after the initial calibration scans.

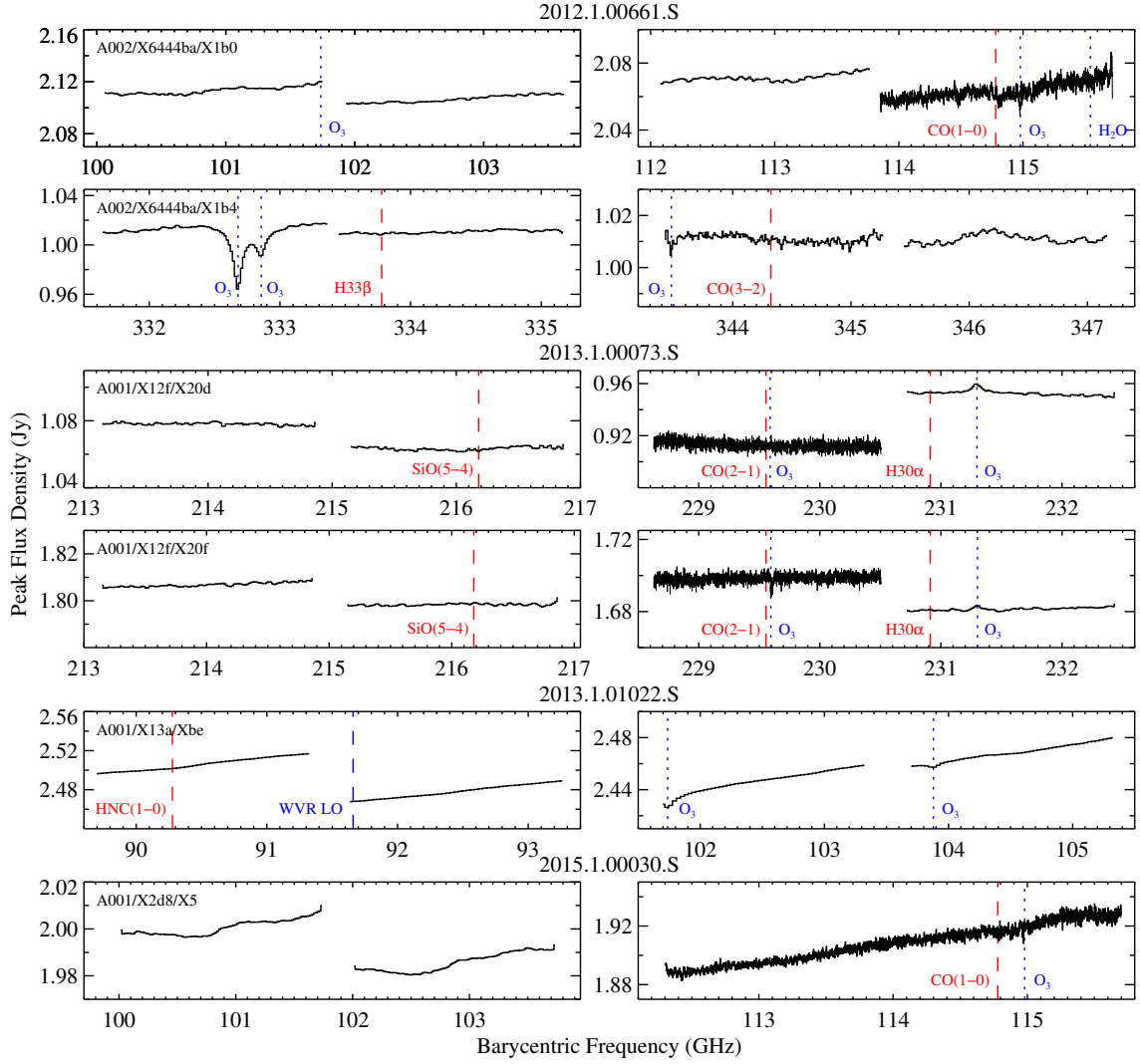


Figure C2. Peak flux density spectra of the M87 nucleus at the native channel binning after standard pipeline and self-calibration processes. Flux calibration was adjusted for overlapping spws in programs 2015.1.00030.S and 2016.1.00021.S only to ensure continuous peak flux densities. The frequencies of atmospheric ozone and water vapor transitions (vertical dotted blue lines; shifted to the barycentric frame), harmonics of the WVR local oscillator (LO; P. C. Cortes et al. 2024), and extragalactic molecular gas and hydrogen recombination transitions (dashed red lines; redshifted by $z_{\text{obs}} = 0.004283$) are also shown. The characteristic scalloped pattern in the .V panels is an artifact of phasing the 12-m antennae in APP mode.

From the continuum spectral cubes, we identified several absorption and emission features that could not be matched to Galactic or extragalactic lines but that did coincide with various telluric ozone (O_3) transitions in the topocentric frame. T. Hunter et al. (2018) demonstrated that the coarse TDM atmospheric calibration used for these ALMA 12-m data may over/undercorrect for atmospheric ozone, resulting in either positive or negative residuals. These lines have been further studied by the PHANGS-ALMA team in Band 6 around redshifted CO(2–1) in their total-power array imaging, primarily as a function of elevation or airmass (A. Usero et al. 2019; A. K. Leroy et al. 2021) while assuming that atmospheric conditions (e.g., relative humidity, ambient temperature, and O_3 concentration) are stable over 1–2 EBs (1–2 hours). Here, we focus on atmospheric variability on such short timescales as well as the impact of calibrator offset on the correction of telluric line features. Since the O_3 transitions do not generally interfere with most of the extragalactic line transitions at the redshift of M87, we did not attempt to mitigate their impact by constructing T_{sys} spectra in FDM mode during manual calibration (as suggested by T. Hunter et al. 2018). In Figure C2 and elsewhere, we indicate the frequencies of the ozone and water vapor transitions that have CDMS/JPL logarithmic intensities¹¹ (H. M. Pickett et al. 1998; H. S. P. Müller et al. 2005) brighter than the limiting -5.3 for which ozone lines have been

¹¹ Identified using the Splatalogue database for astronomical spectroscopy <https://splatalogue.online/>

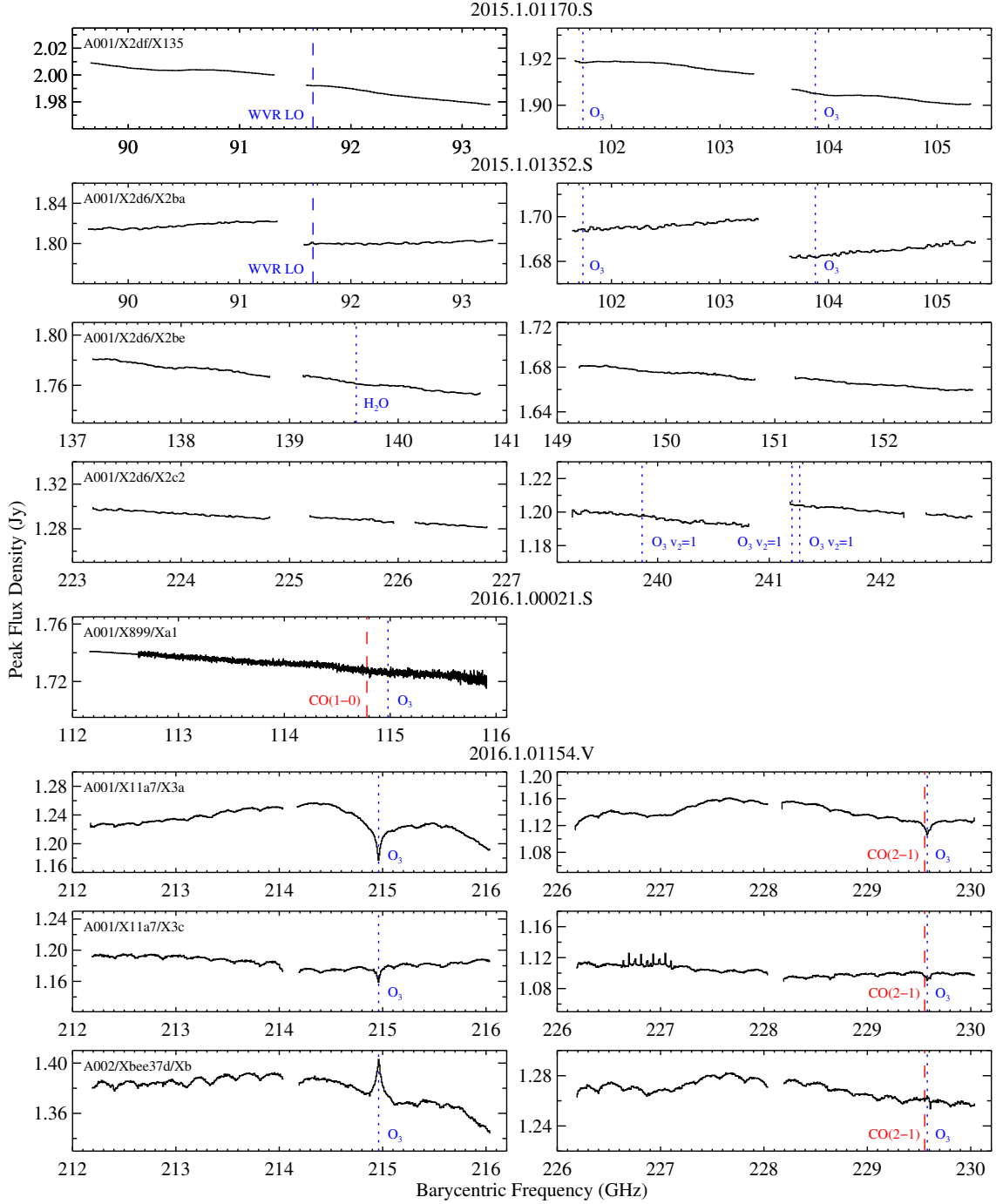


Figure C2. cont.

detected in our ALMA 12-m data. Telluric lines are detected with continuum absorption depths down to a fraction of a percent in data sets with high SDR.

To aid in identifying and characterizing faint ozone features, we employed the `am` atmospheric modeling tool (S. Paine 2018) to calculate an atmospheric transmission curve for each continuum spectrum. This approach adopts column densities for select molecules and approximates the vertical structure with layers of varying pressure and temperature. Without detailed conditions above the Atacama plateau, we borrowed the realistic `am` manual model for Mauna Kea at nearly the same altitude after adjusting for the average PWV, target elevation, and ground-layer temperature for each MS. Using the same spectral ranges and binning, we constructed final transmission curves for each spw and shifted them to barycentric frame to more easily compare to S_ν plots in

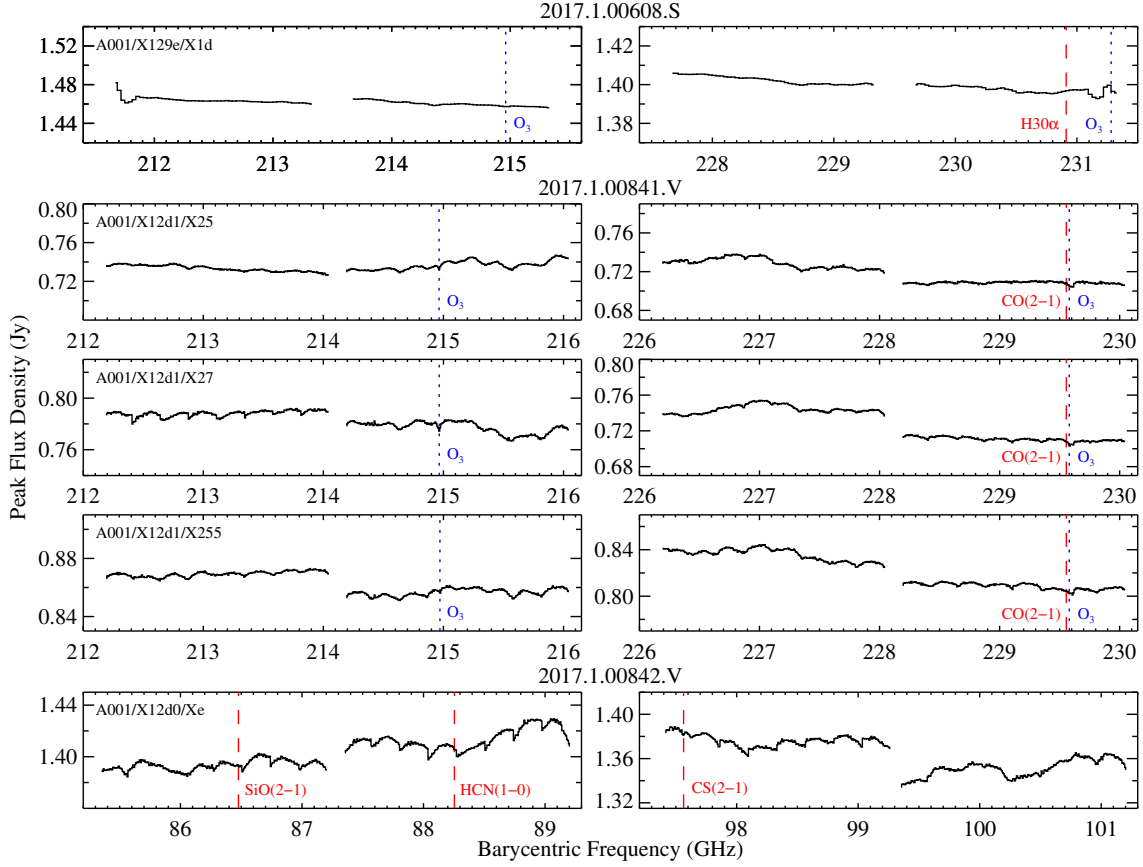


Figure C2. cont.

Figure C2. We note that the *am* model results are close to those from the Atmospheric Transmission at Microwaves model (ATM; J. Pardo et al. 2001; J. R. Pardo 2019), especially after additional minor lines were included and tuned for observed seasonal and diurnal O₃ concentration and altitude changes (S. M. Frith et al. 2020; J. Pardo 2024).

These ozone features are typically distinct from major molecular transitions at a barycentric $z_{\text{obs}} = 0.004283$, although one O₃ transition [23(5,19)–24(4,20); $\nu_{\text{sky}} = 229.575$ GHz] lies close to the CO(2–1) frequency at low redshifts. For the X20f data set, the archival calibration script manually flagged a narrow range of channels for the bandpass calibrator (J1229+0203; 3C 273), misidentifying an atmospheric ozone line as extragalactic in origin. The result was a sharp, moderately deep ($\sim 6\%$ of the continuum level; see Figure D3), spurious absorption feature in the corresponding calibrated M87 spectral window near redshifted $\nu_{\text{CO}(2-1)}$. During pipeline calibration, the wings of this ozone feature remain apparent as slight excesses due to T_{sys} calculations being carried out in TDM mode with default ATM ozone model parameters (T. Hunter et al. 2018). After inspecting the relevant frequency range when this calibrator was a science target in project 2019.1.00807.S, we could not identify a line feature or possible molecular gas candidate at the calibrator’s redshift ($z_{\text{obs}} = 0.15834$). We removed these flags before re-calibrating and re-imaging the X20f MS, which removed nearly all of the ozone line contamination and revealed the faint CO(2–1) absorption feature. None of the other data sets appear to have similar flagging issues.

Atmospheric phase differences between baselines vary with characteristic timescales of minutes. While many studies of water vapor or O₃ column densities tend to track differences on hour timescales or longer (e.g., B. Rappenglück et al. 2014; Q. Zhang et al. 2018; L. T. Maud et al. 2023), rapid changes decrease the coherence time for high-frequency observations (S. Matsushita et al. 2017) and increase phase fluctuations, especially for extended ALMA configurations (G. Privon et al. 2024). Regular WVR measurements correct for smaller-scale, more rapidly-varying PWV changes, and phase self-calibration works to remove residual path length discrepancies. Due to the bright mm/sub-mm continuum source at the center of M87, clean phase solutions can generally be obtained through iterative self-calibration by using the *CASA* `gaincal` task on timescales as short as the scan length. We find that these phase self-calibration loops mitigate nearly all path length fluctuations that arise due to tropospheric turbulence, even on the longest ALMA baselines. However, for two exceptions (the X20d data set and the first EB of X1b0), the self-calibration process never produced sufficiently clean phase solutions regardless of the choice of `refant` or `solint`. The resulting spectra were less reliable due to poorer rms sensitivity or much lower flux scaling and high CLEAN residuals.

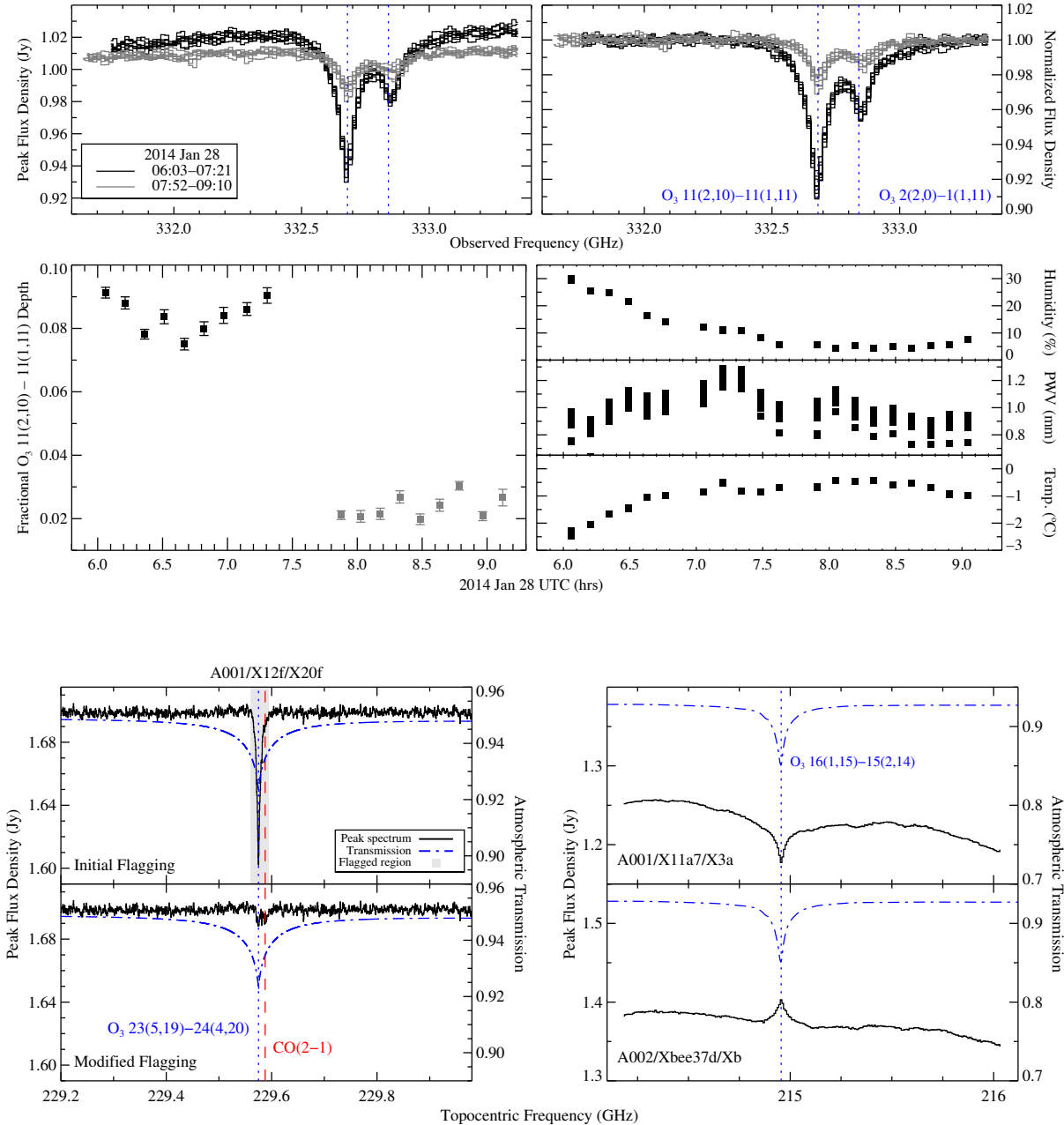


Figure D3. M87 peak continuum spectra showing the residual impact of ozone after pipeline and self-calibration processes. In the Band 7 data (*top panels*), peak spectra imaged by scan show a decrease in residual O_3 line depth (*middle left*) after changing to a more local bandpass calibrator between EBs. Moderate changes in relative humidity and PWV (about the average; dashed line) were detected while the ground temperature was largely stable (*middle right*). For the X20f data set (*bottom left*), pipeline calibration using an earlier ATM version showed a narrow absorption feature coincident with an O_3 line whose core was manually flagged (shaded region) in the bandpass calibrator as an extragalactic line while the broad wings were largely corrected. After removing these flags, the standard calibration script corrected for nearly all the narrow O_3 impact and reveals the faint, narrow $CO(2-1)$ absorption. Some residual O_3 wing excess remains due to calculating T_{sys} with TDM binning. For peak spectra from program 2016.1.01154.V covering a prominent O_3 line (*bottom right*), two EBs observed nearly a week apart show telluric line undercorrection (*top*) and overcorrection (*bottom*) at the 25–50% level during pipeline calibration. In both cases, the an atmospheric transmission model (S. Paine 2018) is overlain for comparison.

Good bandpass calibrators are not always found close to the science target on the sky, but those that are significantly removed in time or obtained along a far-removed line of sight have the potential to leave imprints of atmospheric lines on calibrated science data (G. S. Meena 2010; S. M. Frith et al. 2020). Figure D3 plots the peak $S_{\nu, \text{Band}7}$ spectra obtained in the X1b4 data set during Cycle 1, showing residual O_3 absorption [in the 11(2,10)–11(1,11) and 2(2,0)–1(1,1) transitions; $\nu_{\text{sky}} = 332.705$ and 332.882 GHz, respectively]. The `am` model with matching observing conditions shows a fractional depth of ~ 0.18 for the deeper O_3 line compared to the neighboring continuum. In this member OUS, the bandpass calibrators for the first and second EB were separated by 25.3° and 10.3° from M87, respectively, and `ATM` models removed 55% and 90% of the expected ozone absorption towards M87. The second bandpass calibrator appears to have been observed through a more similar N_{O_3} , enabling a better telluric correction for the second EB. We note that PWV or relative humidity trends are not mirrored by the residual O_3 line strengths as the molecules originate from different altitudes (O_3 primarily at ~ 15 – 40 km while the H_2O scale height is 1–2 km). Variable N_{O_3} is suggested by other data sets, especially in projects 2013.1.00073.S, 2013.1.01022.S, and 2016.1.01154.V. Positive O_3 line features in the target spectral cube suggest a higher N_{O_3} towards the bandpass calibrator than towards the science target. Assuming that N_{O_3} scales linearly with the depth of unsaturated O_3 absorption lines, the residual depths shown in Figure D3 for a single EB suggest that either stratospheric or ground-layer N_{O_3} along the line of sight changed by up to $\sim 6\%$ over just 30 min.

E. CONSTRAINTS ON BROAD CO FEATURES

Here, we present anomalous spectral behavior when excluding wider channel ranges during continuum subtraction. Depending on the choice of fitting windows, some continuum-subtracted spectra of the M87 nucleus appear to show broad but very low-amplitude CO absorption or emission. After exploring possible implications of broad extragalactic CO absorption or emission detection at low S/N, we detail evidence that they arise naturally from the inherent limitations of ALMA bandpass calibration.

E.1. Broad CO Absorption

After excluding channels with $|\nu_{\text{LOS}} - \nu_{\text{sys}}| < 1000$ km s $^{-1}$ in the `uvcontsub` task, we imaged the deeper X1b0, X5, and Xa1 data sets (Band 3) as well as those from X20d and X20f (Band 6) covering redshifted CO(1–0) and CO(2–1) into spectral cubes with ~ 40 km s $^{-1}$ channel binning. For the X1b4 data set (Band 7), we excluded a more narrow channel range with $-1000 < \nu_{\text{LOS}} - \nu_{\text{sys}} < 400$ km s $^{-1}$ due to more limited frequency coverage. In Figure E4, we plot integrated spectra over their central beam areas after adding back the fitted peak continuum, revealing deficits in the $-1000 < \nu_{\text{LOS}} - \nu_{\text{sys}} < 100$ km s $^{-1}$ range. In Band 3, these broad spectral deficits have peak opacities $\tau_{0, \text{CO}(1-0)} \sim 0.002$ – 0.004 with S/N ~ 5 – 25 relative to the rms of the continuum-fitting channels. When integrated over that velocity range, we find $\tau_{\text{CO}(1-0)} \sim 0.1$ – 0.3 km s $^{-1}$ with S/N > 10 . In the higher-frequency Bands, the CO(1–0) opacity signature is not replicated in the same manner.

If real, these deficits would seem to trace a fast molecular outflow. Previously, a blueshifted atomic outflow has been suggested by emission (J. Osorno et al. 2023) and absorption against the bright nucleus (Z. I. Tsvetanov et al. 1999b; B. M. Sabra et al. 2003). However, the atomic gas absorption feature is narrow in comparison and neither reaches the same $\nu_{\text{LOS}} - \nu_{\text{sys}} \sim -1000$ km s $^{-1}$ terminal speeds. We note that such fast outflows have been detected in absorption against ultraluminous infrared galaxy nuclei and AGN, including several LINERs in far-IR OH absorption (albeit at much higher opacity; e.g., S. Veilleux et al. 2013; M. Stone et al. 2016; R. Herrera-Camus et al. 2020). Unfortunately, there is no far-IR spectroscopy covering the M87 nucleus that can probe dense gas to support a possible broad outflow seen in CO. In a closer analog, broad and shallow molecular absorption-line outflows reaching speeds of a few $\times 100$ km s $^{-1}$ are reported against the FR I/Seyfert nucleus of NGC 1275 in dense gas tracers (and likely CO; H. Nagai et al. 2019). In NGC 1275 and other AGN, molecular outflows are detected in emission with blueshifted speeds ranging from ~ 100 – 1000 km s $^{-1}$ (e.g., C. Ciccone et al. 2014; S. García-Burillo et al. 2014; R. A. Riffel et al. 2020; A. D. Bolatto et al. 2021). Evidence for outflows in LINERs is less distinct, with outflow signatures being confined to the wings of the integrated emission-line profiles.

Such a fast molecular outflow in M87 remains unlikely based on both physical and calibration considerations:

1. The M87 core luminosity is well below the expected threshold for an AGN to drive a broad outflow (S. Veilleux et al. 2013; M. A. Prieto et al. 2016).
2. Continuum-subtracted spectra are not fully consistent, even about the same CO transition. In Band 3, the deficits vary in velocity extremes by ~ 600 km s $^{-1}$. For those covering redshifted CO(2–1), the integrated X20d spectrum shows a broader deficit that favors higher recessional speeds while the X20f spectrum appears flat. For redshifted CO(3–2), the X1b4 spectrum is overly deep and abrupt due to narrower velocity coverage and a lack of overlapping spws to anchor the continuum subtraction. Sub-percent level flux mismatches between spws in the upper sideband may also result in a spurious (and relatively deep) deficit.
3. Peak fractional deficits $1 - \exp^{-\tau_0} \approx 0.00025$ are at or below the level of the bandpass stability. In Band 3, correcting for the deep transmission drop due to the adjacent O_2 line may leave residual fluctuations in the profile wings as a result of T_{sys} calculations in TDM mode (see Appendix D and Figure D3). A spurious excess around $115.2 < \nu_{\text{obs}} < 115.9$ GHz due to O_2 overcorrection in the wings could then create the impression of a blueshifted CO deficit after continuum subtraction.

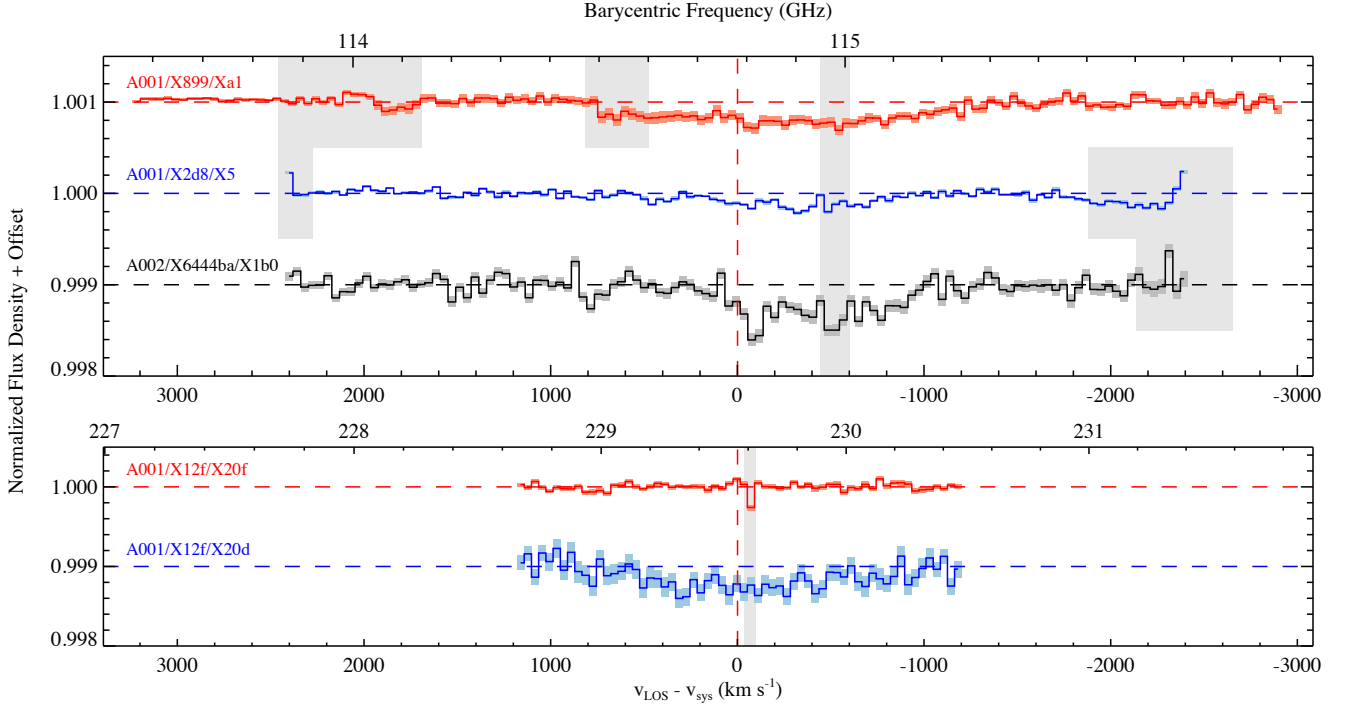


Figure E4. Continuum-subtracted spectra of the M87 nucleus that were integrated in a circular aperture with $R \sim \bar{\theta}_{\text{FWHM}}$. To these, we added in a smooth fit to the peak continuum outside of $|v_{\text{LOS}} - v_{\text{sys}}| < 1000 \text{ km s}^{-1}$ before normalizing. Spectra covering the CO(1–0) (*top panel*), CO(2–1) (*middle*), and CO(3–2) transitions (*bottom*) were imaged using coarse (40 km s^{-1}) binning. Shaded regions indicate uncertain flux densities, due to either residual contamination by narrow atmospheric lines or bandpass calibration issues at spw edges for overlapping spws. The apparent Band 3 spectral deficits between about $-1000 < v_{\text{LOS}} - v_{\text{sys}} < 100 \text{ km s}^{-1}$ could be interpreted as a very tenuous and fast molecular gas outflow traced by CO(1–0) absorption. However, inconsistent Band 6 and 7 results as well as bandpass calibration limitations (discussed in Appendix E.3) make the fast outflow scenario implausible.

E.2. Broad CO Emission

After excluding channels with $100 < |v_{\text{LOS}} - v_{\text{sys}}| < 2200 \text{ km s}^{-1}$ in the `uvcontsub` task (with `fitorder = 1`), we imaged redshifted CO(1–0) in the X5 and Xa1 data sets into cubes with 40 km s^{-1} bins to improve S/N. Care was taken to avoid channels at spw edges that showed poor response or whose flux densities were discrepant with those in overlapping spws. Unfortunately, higher- J transitions did not have sufficient frequency coverage (or spw overlap) to allow for reliable continuum subtraction, so we limited this analysis to the CO(1–0) transition. In Figure E5, we show CO(1–0) position-velocity diagrams (PVDs) extracted in a N–S direction with a width matching the beam average FWHM. The observed excess are roughly centered around $v_{\text{LOS}} - v_{\text{sys}} = -2200$ and $+1000 \text{ km s}^{-1}$, with spatial centroids separated by as little as $0''.015$ ($\sim 1 \text{ pc}$). Because this excess appears to be almost unresolved in either case¹², we constructed line profiles by integrating over the central region with a circular $R = \bar{\theta}_{\text{FWHM}}$ aperture.

From the more symmetrical Xa1 CO line profile, the excess would correspond to an integrated $S_{\text{CO}(1-0)} \Delta v = 4.5 \text{ Jy km s}^{-1}$. Assuming for the moment that the excess represents a dynamically cold disk rotating about the BH, the excess extreme at $2000 < |v_{\text{LOS}} - v_{\text{sys}}| \lesssim 2500 \text{ km s}^{-1}$ can be transformed into an estimate of the molecular gas distribution. Using an inclination angle $i \approx 25^\circ$ (J. Osorno et al. 2023) and an $M_{\text{BH}} \sim 6 \times 10^9 M_{\odot}$ (E. R. Liepold et al. 2023), these $|v_{\text{LOS}} - v_{\text{sys}}|$ extrema would originate ~ 1.7 – 2.7 pc ($0''.02$ – $0''.03$) from the BH while the bulk of the excess would appear to originate $\sim 9 \text{ pc}$ away. However, this is much smaller than $\bar{\theta}_{\text{FWHM}}$ for the Xa1 data set, so a putative rotating disk cannot explain the measured moment 1 map gradient in the N–S direction in Figures 4 and E5. Also, these velocity extrema would be inconsistent with the essentially unresolved excesses in the X5 data set.

Detection of a rotating CNB traced by CO(1–0) on such scales is improbable with the following counter arguments:

¹² We tentatively detect a similar small shift in continuum centroid (but not peak location) in both the X5 and Xa1 continuum cubes shown in Figure C2. We attribute this to residual frequency-dependent phase offsets that had not been fully removed during self-calibration, giving the appearance of a slight spatial shift of the continuum emission.

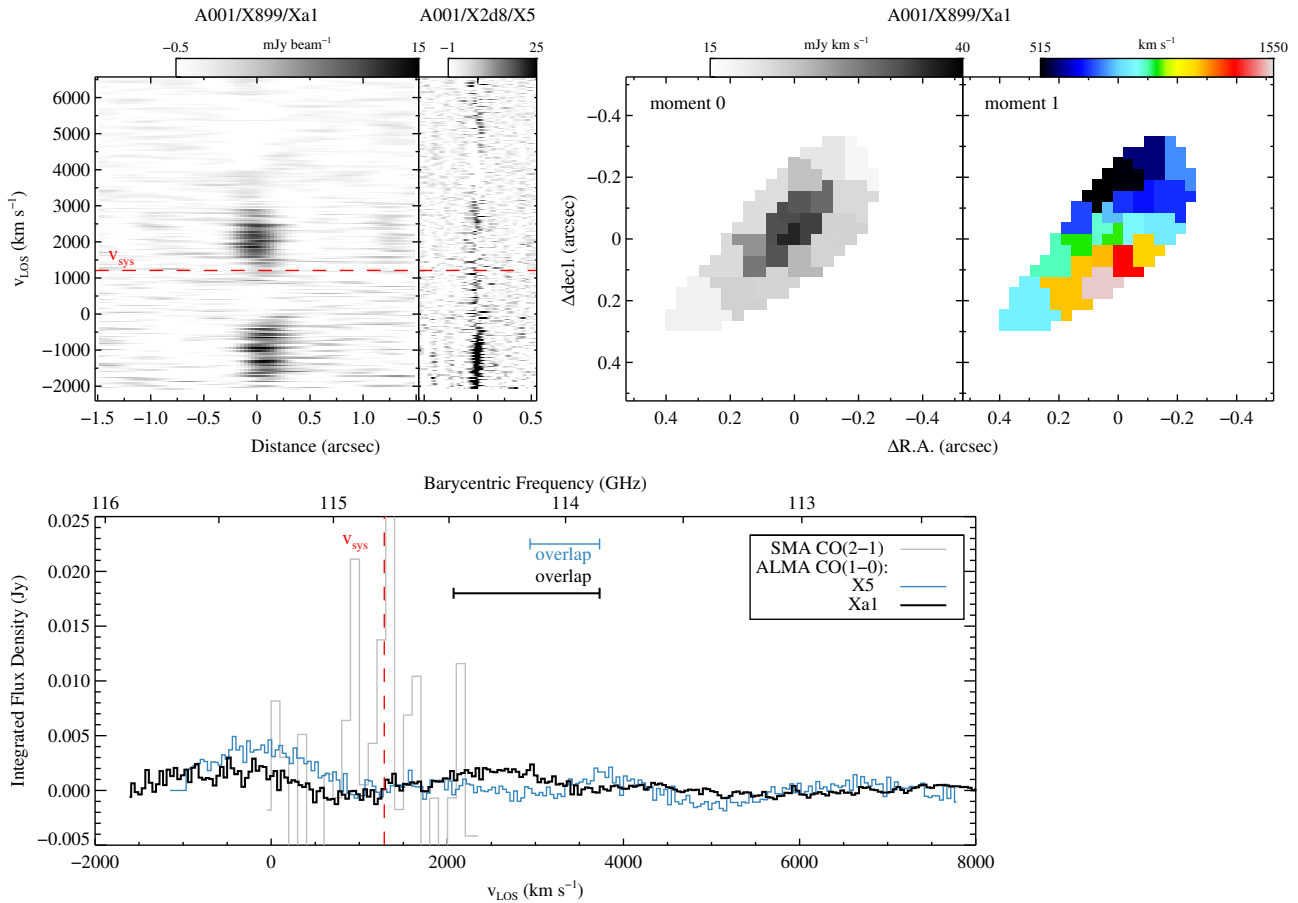


Figure E5. Spectral excess properties from continuum-subtracted M87 data sets containing the CO(1–0) transition redshifted by v_{sys} (dashed lines). The integrated line profiles (*bottom panel*) show larger spectral variation than the channel-to-channel noise. For comparison, we show the narrower SMA CO(2–1) line profile (extracted using PlotDigitizer from J. C. Tan et al. 2008). The primary spw overlap regions where discrepant flux densities could affect the composite line profile are indicated. In large part because of the choice of continuum window, the PVDs extracted along the N-S direction (*top left*) show essentially unresolved spectral excess between about $-2500 < v_{\text{LOS}} - v_{\text{sys}} < -500 \text{ km s}^{-1}$ in both cases and between $200 < v_{\text{LOS}} - v_{\text{sys}} < 2000 \text{ km s}^{-1}$ for the Xa1 data set. The zeroth and first moment maps (*top right*) are inconsistent with the atomic gas CND orientation and extent. The line profiles show distinct, asymmetrical spectral shapes for these two member OUS whose excess/continuum ratios match the bandpass stability level. We therefore consider these features to be residual structures not fully removed during calibration.

1. Based on the Xa1 $S_{\text{CO}}\Delta\nu$ excess, the total molecular mass of $3 \times 10^6 M_{\odot}$ would correspond to $\Sigma_{\text{H}_2} \sim 10^{5.5} - 10^6 M_{\odot} \text{ pc}^{-2}$, which far exceeds surface mass densities for ALMA CO-detected CNDs (e.g., B. D. Boizelle et al. 2017) and comes close to the *highest* constraints on M_{H_2} from thermal excess limits.
2. The excess profiles are not sufficiently consistent or symmetrical, and they are not well centered about v_{sys} . Also, the putative moment 0 (1) map in Figure E5 has a major-axis PA (PA of the velocity gradient) that is oriented $\sim 90^\circ$ ($\sim 45^\circ$) from that of the atomic gas CND. Warping of the inner disk (e.g., I. Ruffa et al. 2019) could not explain the discrepancy.
3. The maximum excess flux densities reach only $\sim 0.15\%$ of the integrated continuum level, matching the $\sim 0.1\%$ amplitude variation seen when testing bandpass stability (S. Kameno 2014).
4. The blueshifted peak at higher frequencies abuts the Band 3 edge. Any calibration residual from the strong O₂ feature may imprint a bump feature around $115.7 < \nu_{\text{obs}} < 115.9 \text{ GHz}$ (similar to that seen in the wings of an O₃ line after correction) due to T_{sys} calculations using TDM frequency binning.

E.3. Bandpass Calibration Accuracy

The maximum SDR ~ 2000 measured in individual channels for the Band 3 data sets corresponds to $\min(\tau_0) \sim 0.0002$, allowing for narrow CO absorption-line detection. For broad line signatures, however, the larger frequency response depends on

the accuracy of the bandpass calibration, effectively lowering the SDR. These spectral calibration solutions vary in frequency as well as in time. *S. Kameno (2014)* demonstrated that cross-correlation bandpass calibration remained stable at the 0.2% level over short time frames (~ 1 hr for Bands 3 and 6), producing a mostly flat spectral response with corresponding global SDR ~ 500 or $\min(\tau_0) \sim 0.002$. For much longer than the length of an EB, changes in atmospheric transmission begin to introduce more significant uncertainty in the bandpass amplitude correction. Imaging that combines multiple EBs, especially with partially overlapping spws, may result in inconsistent or discontinuous spectral behavior. For frequency separations $\Delta\nu \gtrsim 250$ MHz (100–200 MHz and $\gtrsim 500$ MHz) in Band 3 (Band 6), the bandpass amplitude calibration shows noticeable systematic variation above the white-noise prediction (*S. Kameno 2014*). This means that fully calibrated spectra may have very low-amplitude fluctuations imprinted on velocity scales of $\Delta v \gtrsim 650$ km s $^{-1}$ (130–160 km s $^{-1}$, $\gtrsim 650$ km s $^{-1}$).

In Figure E6, we compare the spectral behavior for individual spws in a single sideband from all standard ALMA programs covering redshifted CO(1–0) and CO(2–1) transitions. Especially for Band 3 peak spectra, both the CO-centered and adjacent spws show similar fluctuations at the 0.1–0.3% level relative to the spw channel center. In the lower sideband, adjacent spws also show similar spectral response (e.g., from the X5 and X2be data; see Figure C2.) In Band 3 spectra, the downward fluctuation between 0–0.5 GHz relative to the spw center coincides with the apparent spectral deficits seen in Figure E4. Such fluctuations arising from bandpass amplitude calibration may mimic faint, broad absorption for a fast outflow. For very low-amplitude, broad spectral features, we find a more appropriate SDR ~ 300 –1000 limit across a single Band 3 spw using the standard bandpass calibration. Because these Band 3 spectra about a strong O $_2$ absorption feature, they may also be negatively impacted by the T_{sys} correction as well as slight changes in N_{O_2} between the bandpass and science scans, either due to temporal variations or angular separation. In Band 6, the spectral shape appears more consistent with fluctuations at or below the 0.05% level, matching its native SDR. However, the small sample size of deep Band 6 imaging with fine FDM binning prevents any clear conclusions.

We find further support for a bandpass calibration origin for these low-amplitude spectral features in the peak S_ν spectrum in roughly contemporaneous observations. For example, the peak S_ν shape over 102–104 GHz in the X5 data set is inconsistent with those covering the same spectral range in Xbe and X135 data sets, which were obtained just weeks apart. While the latter two member OUS used a different bandpass calibrator (J1229+0203) than the former (J1256–0547), differences in the calibrated, intra-spw shape is still within the quoted limitations for bandpass calibration (*G. Privon et al. 2024*). For these reasons, we view the very low amplitude spectral deficits or excess features in Figures E4 and E5 as spurious and arising from a patterned response in the bandpass amplitude calibration for adjacent basebands. The mostly regular shape and extent of the seemingly broad CO(1–0) absorption in Figure E4 would then be a product of spw placement relative to the redshifted CO transition and proximity to the O $_2$ line that defines the end of the Band coverage.

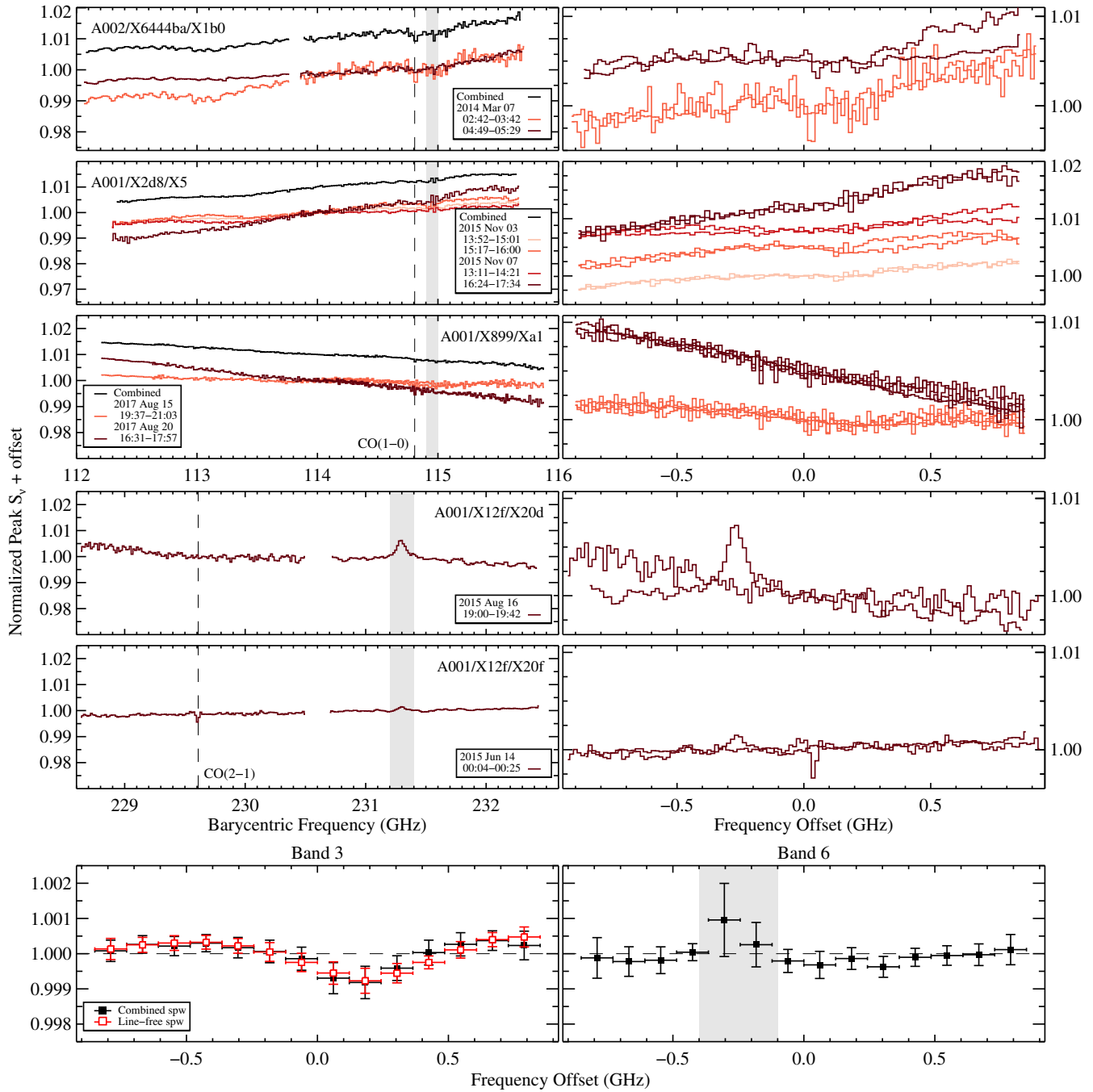


Figure E6. Bands 3 and 6 peak spectra of the M87 nucleus covering the redshifted CO(1–0) and CO(2–1) transitions in the upper sideband (*top and middle left panels*). Channels were averaged during `tclean` imaging to better determine broad spectral behavior, which appears to undulate well beyond the relative $-1000 < v_{\text{LOS}} - v_{\text{sys}} < 100$ km s $^{-1}$ range where the broad spectral deficit appears. Data were imaged within each UT time range and normalized at either 114 or 230 GHz. The combined peak spectra for each member OUS are offset slightly higher for clarity. Residual O₃ contaminated ranges are indicated (shaded regions). Comparing the spectral behavior for all spws in that sideband (*top and middle right*; grouped by UT date) reveals an apparent depression between 0–0.5 GHz at the 0.2–0.3% level, even when a spw does not cover CO(1–0). After dividing all these data by the corresponding full-spw or sideband continuum fit, the average Band 3 spectral response in the upper sideband shows a clear trend beyond the 1σ scatter of normalized intensities (*bottom left*). Bandpass-related fluctuations appear in correlated depressions at the 0.1% level. In Band 6, the normalized response appears flat (*bottom right*).

REFERENCES

Acciari, V. A., Aliu, E., Arlen, T., et al. 2009, *Science*, 325, 444,
doi: [10.1126/science.1175406](https://doi.org/10.1126/science.1175406)

André, P. J., Palmeirim, P., & Arzoumanian, D. 2022, *A&A*, 667,
L1, doi: [10.1051/0004-6361/202244541](https://doi.org/10.1051/0004-6361/202244541)

- Arzoumanian, D., Shimajiri, Y., Inutsuka, S.-i., Inoue, T., & Tachihara, K. 2018, PASJ, 70, 96, doi: [10.1093/pasj/psy095](https://doi.org/10.1093/pasj/psy095)
- Arzoumanian, D., André, P., Didelon, P., et al. 2011, A&A, 529, L6, doi: [10.1051/0004-6361/201116596](https://doi.org/10.1051/0004-6361/201116596)
- Babyk, I. V., McNamara, B. R., Tamhane, P. D., et al. 2019, ApJ, 887, 149, doi: [10.3847/1538-4357/ab54ce](https://doi.org/10.3847/1538-4357/ab54ce)
- Baek, J., Chung, A., Edge, A., et al. 2022, ApJ, 932, 64, doi: [10.3847/1538-4357/ac6de6](https://doi.org/10.3847/1538-4357/ac6de6)
- Baes, M., Clemens, M., Xilouris, E. M., et al. 2010, A&A, 518, L53, doi: [10.1051/0004-6361/201014555](https://doi.org/10.1051/0004-6361/201014555)
- Barth, A. J., Boizelle, B. D., Darling, J., et al. 2016, ApJL, 822, L28, doi: [10.3847/2041-8205/822/2/L28](https://doi.org/10.3847/2041-8205/822/2/L28)
- Bianchi, S., Maiolino, R., & Risaliti, G. 2012, Advances in Astronomy, 2012, 782030, doi: [10.1155/2012/782030](https://doi.org/10.1155/2012/782030)
- Bicknell, G. V., & Begelman, M. C. 1996, ApJ, 467, 597, doi: [10.1086/177636](https://doi.org/10.1086/177636)
- Bieging, J. H., Blitz, L., Lada, C. J., & Stark, A. A. 1981, ApJ, 247, 443, doi: [10.1086/159052](https://doi.org/10.1086/159052)
- Biretta, J. A., Sparks, W. B., & Macchetto, F. 1999, ApJ, 520, 621, doi: [10.1086/307499](https://doi.org/10.1086/307499)
- Biretta, J. A., Stern, C. P., & Harris, D. E. 1991, AJ, 101, 1632, doi: [10.1086/115793](https://doi.org/10.1086/115793)
- Blakeslee, J. P., Jordán, A., Mei, S., et al. 2009, ApJ, 694, 556, doi: [10.1088/0004-637X/694/1/556](https://doi.org/10.1088/0004-637X/694/1/556)
- Boizelle, B. D., Barth, A. J., Darling, J., et al. 2017, ApJ, 845, 170, doi: [10.3847/1538-4357/aa8266](https://doi.org/10.3847/1538-4357/aa8266)
- Boizelle, B. D., Barth, A. J., Walsh, J. L., et al. 2019, ApJ, 881, 10, doi: [10.3847/1538-4357/ab2a0a](https://doi.org/10.3847/1538-4357/ab2a0a)
- Boizelle, B. D., Walsh, J. L., Barth, A. J., et al. 2021, ApJ, 908, 19, doi: [10.3847/1538-4357/abd24d](https://doi.org/10.3847/1538-4357/abd24d)
- Bolatto, A. D., Wolfire, M., & Leroy, A. K. 2013, ARA&A, 51, 207, doi: [10.1146/annurev-astro-082812-140944](https://doi.org/10.1146/annurev-astro-082812-140944)
- Bolatto, A. D., Leroy, A. K., Levy, R. C., et al. 2021, ApJ, 923, 83, doi: [10.3847/1538-4357/ac2c08](https://doi.org/10.3847/1538-4357/ac2c08)
- Bonato, M., Liuzzo, E., Giannetti, A., et al. 2018, MNRAS, 478, 1512, doi: [10.1093/mnras/sty1173](https://doi.org/10.1093/mnras/sty1173)
- Bonato, M., Liuzzo, E., Herranz, D., et al. 2019, MNRAS, 485, 1188, doi: [10.1093/mnras/stz465](https://doi.org/10.1093/mnras/stz465)
- Boselli, A., Fossati, M., Longobardi, A., et al. 2019, A&A, 623, A52, doi: [10.1051/0004-6361/201834492](https://doi.org/10.1051/0004-6361/201834492)
- Bower, G. C., Dexter, J., Markoff, S., et al. 2015, ApJL, 811, L6, doi: [10.1088/2041-8205/811/1/L6](https://doi.org/10.1088/2041-8205/811/1/L6)
- Braine, J., & Wiklind, T. 1993, A&A, 267, L47
- Brauher, J. R., Dale, D. A., & Helou, G. 2008, ApJS, 178, 280, doi: [10.1086/590249](https://doi.org/10.1086/590249)
- Briggs, D. S. 1995, PhD thesis, New Mexico Institute of Mining and Technology
- Cappellari, M., & Copin, Y. 2003, MNRAS, 342, 345, doi: [10.1046/j.1365-8711.2003.06541.x](https://doi.org/10.1046/j.1365-8711.2003.06541.x)
- Cappellari, M., Emsellem, E., Krajnović, D., et al. 2011, MNRAS, 413, 813, doi: [10.1111/j.1365-2966.2010.18174.x](https://doi.org/10.1111/j.1365-2966.2010.18174.x)
- Cardelli, J. A., Clayton, G. C., & Mathis, J. S. 1989, ApJ, 345, 245, doi: [10.1086/167900](https://doi.org/10.1086/167900)
- Carter, D., & Jenkins, C. R. 1992, MNRAS, 257, 7P, doi: [10.1093/mnras/257.1.7P](https://doi.org/10.1093/mnras/257.1.7P)
- Carter, D., Johnstone, R. M., & Fabian, A. C. 1997, MNRAS, 285, L20, doi: [10.1093/mnras/285.3.L20](https://doi.org/10.1093/mnras/285.3.L20)
- Cashman, F. H., Fox, A. J., Savage, B. D., et al. 2021, ApJL, 923, L11, doi: [10.3847/2041-8213/ac3cbc](https://doi.org/10.3847/2041-8213/ac3cbc)
- Cheung, C. C., Harris, D. E., & Stawarz, Ł. 2007, ApJL, 663, L65, doi: [10.1086/520510](https://doi.org/10.1086/520510)
- Chiaberge, M., Capetti, A., & Celotti, A. 1999, A&A, 349, 77, <https://arxiv.org/abs/astro-ph/9907064>
- Cicone, C., Maiolino, R., Sturm, E., et al. 2014, A&A, 562, A21, doi: [10.1051/0004-6361/201322464](https://doi.org/10.1051/0004-6361/201322464)
- Combes, F., Young, L. M., & Bureau, M. 2007, MNRAS, 377, 1795, doi: [10.1111/j.1365-2966.2007.11759.x](https://doi.org/10.1111/j.1365-2966.2007.11759.x)
- Cortes, P. C., Vlahakis, C., Hales, A., et al. 2024, 11.3, Zenodo Zenodo, doi: [10.5281/zenodo.4511521](https://doi.org/10.5281/zenodo.4511521)
- Crocker, A., Krips, M., Bureau, M., et al. 2012, MNRAS, 421, 1298, doi: [10.1111/j.1365-2966.2011.20393.x](https://doi.org/10.1111/j.1365-2966.2011.20393.x)
- Csengeri, T., Bontemps, S., Wyrowski, F., et al. 2017, A&A, 600, L10, doi: [10.1051/0004-6361/201629754](https://doi.org/10.1051/0004-6361/201629754)
- Dasyra, K. M., Combes, F., Oosterloo, T., et al. 2016, A&A, 595, L7, doi: [10.1051/0004-6361/201629689](https://doi.org/10.1051/0004-6361/201629689)
- Davidson, J. R., Boizelle, B. D., Walsh, J. L., et al. 2024, ApJ, 972, 127, doi: [10.3847/1538-4357/ad5be4](https://doi.org/10.3847/1538-4357/ad5be4)
- Davies, R. D., & Cummings, E. R. 1975, MNRAS, 170, 95, doi: [10.1093/mnras/170.1.95](https://doi.org/10.1093/mnras/170.1.95)
- Davis, T. A., Bureau, M., Onishi, K., et al. 2017, MNRAS, 468, 4675, doi: [10.1093/mnras/stw3217](https://doi.org/10.1093/mnras/stw3217)
- de Blok, W. J. G., Keating, K. M., Pisano, D. J., et al. 2014, A&A, 569, A68, doi: [10.1051/0004-6361/201423880](https://doi.org/10.1051/0004-6361/201423880)
- de Koff, S., Best, P., Baum, S. A., et al. 2000, ApJS, 129, 33, doi: [10.1086/313402](https://doi.org/10.1086/313402)
- de Vaucouleurs, G., de Vaucouleurs, A., Corwin, Herold G., J., et al. 1991, Third Reference Catalogue of Bright Galaxies
- Di Matteo, T., Allen, S. W., Fabian, A. C., Wilson, A. S., & Young, A. J. 2003, ApJ, 582, 133, doi: [10.1086/344504](https://doi.org/10.1086/344504)
- Doi, A., Hada, K., Nagai, H., et al. 2013, in European Physical Journal Web of Conferences, Vol. 61, European Physical Journal Web of Conferences, 08008, doi: [10.1051/epjconf/20136108008](https://doi.org/10.1051/epjconf/20136108008)
- Dopita, M. A., Koratkar, A. P., Allen, M. G., et al. 1997, ApJ, 490, 202, doi: [10.1086/304862](https://doi.org/10.1086/304862)
- Draine, B. T. 2003, ARA&A, 41, 241, doi: [10.1146/annurev.astro.41.011802.094840](https://doi.org/10.1146/annurev.astro.41.011802.094840)
- Draine, B. T., Aniano, G., Krause, O., et al. 2014, ApJ, 780, 172, doi: [10.1088/0004-637X/780/2/172](https://doi.org/10.1088/0004-637X/780/2/172)

- Dressel, L. 2022, in *WFC3 Instrument Handbook for Cycle 30 v. 14*, Vol. 14, 14
- Edge, A. C. 2001, *MNRAS*, 328, 762, doi: [10.1046/j.1365-8711.2001.04802.x](https://doi.org/10.1046/j.1365-8711.2001.04802.x)
- EHT Collaboration, Akiyama, K., Alberdi, A., et al. 2019, *ApJL*, 875, L1, doi: [10.3847/2041-8213/ab0ec7](https://doi.org/10.3847/2041-8213/ab0ec7)
- EHT Collaboration, Akiyama, K., Algaba, J. C., et al. 2021a, *ApJL*, 910, L12, doi: [10.3847/2041-8213/abe71d](https://doi.org/10.3847/2041-8213/abe71d)
- EHT Collaboration, Akiyama, K., Algaba, J. C., et al. 2021b, *ApJL*, 910, L13, doi: [10.3847/2041-8213/abe4de](https://doi.org/10.3847/2041-8213/abe4de)
- EHT MWL Science Working Group, EHT Collaboration, The Fermi Large Area Telescope Collaboration, et al. 2024, arXiv e-prints, arXiv:2404.17623, doi: [10.48550/arXiv.2404.17623](https://doi.org/10.48550/arXiv.2404.17623)
- EHT MWL Science Working Group, Algaba, J. C., Anczarski, J., et al. 2021, *ApJL*, 911, L11, doi: [10.3847/2041-8213/abef71](https://doi.org/10.3847/2041-8213/abef71)
- Emmanoulopoulos, D., McHardy, I. M., & Papadakis, I. E. 2013, *MNRAS*, 433, 907, doi: [10.1093/mnras/st764](https://doi.org/10.1093/mnras/st764)
- Emsellem, E., Monnet, G., & Bacon, R. 1994, *A&A*, 285, 723
- Fanaroff, B. L., & Riley, J. M. 1974, *MNRAS*, 167, 31P, doi: [10.1093/mnras/167.1.31P](https://doi.org/10.1093/mnras/167.1.31P)
- Ferland, G. J., Korista, K. T., Verner, D. A., et al. 1998, *PASP*, 110, 761, doi: [10.1086/316190](https://doi.org/10.1086/316190)
- Ferrarese, L., Ford, H. C., & Jaffe, W. 1996, *ApJ*, 470, 444, doi: [10.1086/177876](https://doi.org/10.1086/177876)
- Ferrarese, L., Côté, P., Jordán, A., et al. 2006, *ApJS*, 164, 334, doi: [10.1086/501350](https://doi.org/10.1086/501350)
- Fomalont, E., van Kempen, T., Kneissl, R., et al. 2014, *The Messenger*, 155, 19
- Ford, H. C., & Butcher, H. 1979, *ApJS*, 41, 147, doi: [10.1086/190613](https://doi.org/10.1086/190613)
- Ford, H. C., Harms, R. J., Tsvetanov, Z. I., et al. 1994, *ApJL*, 435, L27, doi: [10.1086/187586](https://doi.org/10.1086/187586)
- Forman, W., Jones, C., Churazov, E., et al. 2007, *ApJ*, 665, 1057, doi: [10.1086/519480](https://doi.org/10.1086/519480)
- Fournier, M., Grete, P., Brüggem, M., Glines, F. W., & O'Shea, B. W. 2024, arXiv e-prints, arXiv:2406.05044, doi: [10.48550/arXiv.2406.05044](https://doi.org/10.48550/arXiv.2406.05044)
- Francis, L., Johnstone, D., Herczeg, G., Hunter, T. R., & Harsono, D. 2020a, in *Five Years After HL Tau: A New Era in Planet Formation (HLTAU2020)*, 23, doi: [10.5281/zenodo.4300195](https://doi.org/10.5281/zenodo.4300195)
- Francis, L., Johnstone, D., Herczeg, G., Hunter, T. R., & Harsono, D. 2020b, *AJ*, 160, 270, doi: [10.3847/1538-3881/abbe1a](https://doi.org/10.3847/1538-3881/abbe1a)
- Frith, S. M., Bhartia, P. K., Oman, L. D., et al. 2020, *Atmospheric Measurement Techniques*, 13, 2733, doi: [10.5194/amt-13-2733-2020](https://doi.org/10.5194/amt-13-2733-2020)
- Ganguly, S., Li, Y., Olivares, V., et al. 2023, *Frontiers in Astronomy and Space Sciences*, 10, 1138613, doi: [10.3389/fspas.2023.1138613](https://doi.org/10.3389/fspas.2023.1138613)
- García-Burillo, S., Combes, F., Usero, A., et al. 2014, *A&A*, 567, A125, doi: [10.1051/0004-6361/201423843](https://doi.org/10.1051/0004-6361/201423843)
- Gaspari, M., Ruszkowski, M., & Oh, S. P. 2013, *MNRAS*, 432, 3401, doi: [10.1093/mnras/stt692](https://doi.org/10.1093/mnras/stt692)
- Gaspari, M., Tombesi, F., & Cappi, M. 2020, *Nature Astronomy*, 4, 10, doi: [10.1038/s41550-019-0970-1](https://doi.org/10.1038/s41550-019-0970-1)
- Gebhardt, K., & Thomas, J. 2009, *ApJ*, 700, 1690, doi: [10.1088/0004-637X/700/2/1690](https://doi.org/10.1088/0004-637X/700/2/1690)
- Gerin, M., Liszt, H., Pety, J., & Faure, A. 2024, *A&A*, 686, A49, doi: [10.1051/0004-6361/202449152](https://doi.org/10.1051/0004-6361/202449152)
- Giroletti, M., Hada, K., Giovannini, G., et al. 2012, *A&A*, 538, L10, doi: [10.1051/0004-6361/201218794](https://doi.org/10.1051/0004-6361/201218794)
- Gnedin, N. Y., & Draine, B. T. 2014, *ApJ*, 795, 37, doi: [10.1088/0004-637X/795/1/37](https://doi.org/10.1088/0004-637X/795/1/37)
- Godard, B., Falgarone, E., Gerin, M., Hily-Blant, P., & de Luca, M. 2010, *A&A*, 520, A20, doi: [10.1051/0004-6361/201014283](https://doi.org/10.1051/0004-6361/201014283)
- Goddi, C., Martí-Vidal, I., Messias, H., et al. 2019, *PASP*, 131, 075003, doi: [10.1088/1538-3873/ab136a](https://doi.org/10.1088/1538-3873/ab136a)
- Goddi, C., Martí-Vidal, I., Messias, H., et al. 2021, *ApJL*, 910, L14, doi: [10.3847/2041-8213/abee6a](https://doi.org/10.3847/2041-8213/abee6a)
- Grier, C. J., Brandt, W. N., Hall, P. B., et al. 2016, *ApJ*, 824, 130, doi: [10.3847/0004-637X/824/2/130](https://doi.org/10.3847/0004-637X/824/2/130)
- H. E. S. S. Collaboration, Abramowski, A., Acero, F., et al. 2011, *A&A*, 528, A143, doi: [10.1051/0004-6361/201015381](https://doi.org/10.1051/0004-6361/201015381)
- Hada, K. 2017, *Galaxies*, 5, 2, doi: [10.3390/galaxies5010002](https://doi.org/10.3390/galaxies5010002)
- Hada, K., Giroletti, M., Kino, M., et al. 2014, *ApJ*, 788, 165, doi: [10.1088/0004-637X/788/2/165](https://doi.org/10.1088/0004-637X/788/2/165)
- Hada, K., Kino, M., Doi, A., et al. 2016, *ApJ*, 817, 131, doi: [10.3847/0004-637X/817/2/131](https://doi.org/10.3847/0004-637X/817/2/131)
- Hada, K., Park, J. H., Kino, M., et al. 2017, *PASJ*, 69, 71, doi: [10.1093/pasj/psx054](https://doi.org/10.1093/pasj/psx054)
- Harms, R. J., Ford, H. C., Tsvetanov, Z. I., et al. 1994, *ApJL*, 435, L35, doi: [10.1086/187588](https://doi.org/10.1086/187588)
- Heckman, T. M., Baum, S. A., van Breugel, W. J. M., & McCarthy, P. 1989, *ApJ*, 338, 48, doi: [10.1086/167181](https://doi.org/10.1086/167181)
- Hennebelle, P. 2013, *A&A*, 556, A153, doi: [10.1051/0004-6361/201321292](https://doi.org/10.1051/0004-6361/201321292)
- Herrera-Camus, R., Janssen, A., Sturm, E., et al. 2020, *A&A*, 635, A47, doi: [10.1051/0004-6361/201936434](https://doi.org/10.1051/0004-6361/201936434)
- Ho, L. C., Filippenko, A. V., & Sargent, W. L. W. 1997, *ApJS*, 112, 315, doi: [10.1086/313041](https://doi.org/10.1086/313041)
- Hunter, T., Phillips, N., Broguière, D., & Gonzalez, J. 2018, *NRAO Immer*, K., et al. 2024,
- Inayoshi, K., Ichikawa, K., & Ho, L. C. 2020, *ApJ*, 894, 141, doi: [10.3847/1538-4357/ab8569](https://doi.org/10.3847/1538-4357/ab8569)
- Indebetouw, R., Wong, T., Chen, C. H. R., et al. 2020, *ApJ*, 888, 56, doi: [10.3847/1538-4357/ab5db7](https://doi.org/10.3847/1538-4357/ab5db7)
- Israel, F. P. 1992, *A&A*, 265, 487
- Jaffe, W. 1987, *A&A*, 171, 378
- Kaasra, J. S., Kriss, G. A., Cappi, M., et al. 2014, *Science*, 345, 64, doi: [10.1126/science.1253787](https://doi.org/10.1126/science.1253787)
- Kameno, S. 2014., *Tech. rep.*, JAO/NAOJ

- Kameno, S., Sawada-Satoh, S., Impellizzeri, C. M. V., et al. 2020, *ApJ*, 895, 73, doi: [10.3847/1538-4357/ab8bd6](https://doi.org/10.3847/1538-4357/ab8bd6)
- Kim, J. Y., Krichbaum, T. P., Lu, R. S., et al. 2018, *A&A*, 616, A188, doi: [10.1051/0004-6361/201832921](https://doi.org/10.1051/0004-6361/201832921)
- Klitsch, A., Péroux, C., Zwaan, M. A., et al. 2019, *MNRAS*, 490, 1220, doi: [10.1093/mnras/stz2660](https://doi.org/10.1093/mnras/stz2660)
- Koch, E. W., & Rosolowsky, E. W. 2015, *MNRAS*, 452, 3435, doi: [10.1093/mnras/stv1521](https://doi.org/10.1093/mnras/stv1521)
- Kokusho, T., Kaneda, H., Bureau, M., et al. 2019, *A&A*, 622, A87, doi: [10.1051/0004-6361/201833911](https://doi.org/10.1051/0004-6361/201833911)
- Komugi, S., Toba, Y., Matsuoka, Y., Saito, T., & Yamashita, T. 2022, *ApJ*, 930, 3, doi: [10.3847/1538-4357/ac616e](https://doi.org/10.3847/1538-4357/ac616e)
- Könyves, V., André, P., Arzoumanian, D., et al. 2020, *A&A*, 635, A34, doi: [10.1051/0004-6361/201834753](https://doi.org/10.1051/0004-6361/201834753)
- Kuo, C. Y., Asada, K., Rao, R., et al. 2014, *ApJL*, 783, L33, doi: [10.1088/2041-8205/783/2/L33](https://doi.org/10.1088/2041-8205/783/2/L33)
- Leroy, A. K., Hughes, A., Liu, D., et al. 2021, *ApJS*, 255, 19, doi: [10.3847/1538-4365/abec80](https://doi.org/10.3847/1538-4365/abec80)
- Liepold, E. R., Ma, C.-P., & Walsh, J. L. 2023, *ApJL*, 945, L35, doi: [10.3847/2041-8213/acbbcf](https://doi.org/10.3847/2041-8213/acbbcf)
- Lim, J., Dinh-V-Trung, V., Vrtilek, J., David, L. P., & Forman, W. 2017, *ApJ*, 850, 31, doi: [10.3847/1538-4357/aa9275](https://doi.org/10.3847/1538-4357/aa9275)
- Liszt, H., Gerin, M., & Grenier, I. 2019, *A&A*, 627, A95, doi: [10.1051/0004-6361/201935436](https://doi.org/10.1051/0004-6361/201935436)
- Liszt, H., & Lucas, R. 2004, *A&A*, 428, 445, doi: [10.1051/0004-6361:20041650](https://doi.org/10.1051/0004-6361:20041650)
- Liszt, H. S., & Lucas, R. 1998, *A&A*, 339, 561
- Liszt, H. S., & Pety, J. 2012, *A&A*, 541, A58, doi: [10.1051/0004-6361/201218771](https://doi.org/10.1051/0004-6361/201218771)
- Longobardi, A., Arnaboldi, M., Gerhard, O., & Mihos, J. C. 2015, *A&A*, 579, L3, doi: [10.1051/0004-6361/201526282](https://doi.org/10.1051/0004-6361/201526282)
- Lu, R.-S., Asada, K., Krichbaum, T. P., et al. 2023, *Nature*, 616, 686, doi: [10.1038/s41586-023-05843-w](https://doi.org/10.1038/s41586-023-05843-w)
- Macchetto, F., Marconi, A., Axon, D. J., et al. 1997, *ApJ*, 489, 579, doi: [10.1086/304823](https://doi.org/10.1086/304823)
- Madrid, J. P., Sparks, W. B., Harris, D. E., et al. 2007, *Ap&SS*, 311, 329, doi: [10.1007/s10509-007-9528-2](https://doi.org/10.1007/s10509-007-9528-2)
- Mangum, J., & Shirley, Y. 2015, *Publications of the Astronomical Society of the Pacific*, 127, doi: [10.1086/680323](https://doi.org/10.1086/680323)
- Margulis, M., & Snell, R. L. 1989, *ApJ*, 343, 779, doi: [10.1086/167749](https://doi.org/10.1086/167749)
- Marshall, H. L., Miller, B. P., Davis, D. S., et al. 2002, *ApJ*, 564, 683, doi: [10.1086/324396](https://doi.org/10.1086/324396)
- Mathews, W. G., & Brighenti, F. 2003, *ARA&A*, 41, 191, doi: [10.1146/annurev.astro.41.090401.094542](https://doi.org/10.1146/annurev.astro.41.090401.094542)
- Matsushita, S., Asaki, Y., Fomalont, E. B., et al. 2017, *PASP*, 129, 035004, doi: [10.1088/1538-3873/aa5787](https://doi.org/10.1088/1538-3873/aa5787)
- Maud, L. T., Pérez-Sánchez, A. F., Asaki, Y., et al. 2023, *arXiv e-prints*, arXiv:2304.08318, doi: [10.48550/arXiv.2304.08318](https://doi.org/10.48550/arXiv.2304.08318)
- McMullin, J. P., Waters, B., Schiebel, D., Young, W., & Golap, K. 2007, in *Astronomical Society of the Pacific Conference Series*, Vol. 376, *Astronomical Data Analysis Software and Systems XVI*, ed. R. A. Shaw, F. Hill, & D. J. Bell, 127
- Meena, G. S. 2010, *Journal of Earth System Science*, 119, 249, doi: [10.1007/s12040-010-0024-7](https://doi.org/10.1007/s12040-010-0024-7)
- Misawa, T., Charlton, J. C., & Eracleous, M. 2014, *ApJ*, 792, 77, doi: [10.1088/0004-637X/792/1/77](https://doi.org/10.1088/0004-637X/792/1/77)
- Misawa, T., Eracleous, M., Charlton, J. C., & Kashikawa, N. 2019, *ApJ*, 870, 68, doi: [10.3847/1538-4357/aaf0fe](https://doi.org/10.3847/1538-4357/aaf0fe)
- Mould, J. R., Huchra, J. P., Freedman, W. L., et al. 2000, *ApJ*, 529, 786, doi: [10.1086/308304](https://doi.org/10.1086/308304)
- Müller, H. S. P., Schlöder, F., Stutzki, J., & Winnewisser, G. 2005, *Journal of Molecular Structure*, 742, 215, doi: [10.1016/j.molstruc.2005.01.027](https://doi.org/10.1016/j.molstruc.2005.01.027)
- Nagai, H., Onishi, K., Kawakatu, N., et al. 2019, *ApJ*, 883, 193, doi: [10.3847/1538-4357/ab3e6e](https://doi.org/10.3847/1538-4357/ab3e6e)
- North, E. V., Davis, T. A., Bureau, M., et al. 2019, *MNRAS*, 490, 319, doi: [10.1093/mnras/stz2598](https://doi.org/10.1093/mnras/stz2598)
- Ocaña Flaquer, B., Leon, S., Combes, F., & Lim, J. 2010, *A&A*, 518, A9, doi: [10.1051/0004-6361/200913392](https://doi.org/10.1051/0004-6361/200913392)
- Olivares, V., Salome, P., Combes, F., et al. 2019, *A&A*, 631, A22, doi: [10.1051/0004-6361/201935350](https://doi.org/10.1051/0004-6361/201935350)
- Osorno, J., Nagar, N., Richtler, T., et al. 2023, *A&A*, 679, A37, doi: [10.1051/0004-6361/202346549](https://doi.org/10.1051/0004-6361/202346549)
- Paine, S. 2018,, 10.0, Zenodo Zenodo, doi: [10.5281/zenodo.1193771](https://doi.org/10.5281/zenodo.1193771)
- Panopoulou, G. V., Psaradaki, I., & Tassis, K. 2016, *MNRAS*, 462, 1517, doi: [10.1093/mnras/stw1678](https://doi.org/10.1093/mnras/stw1678)
- Pardo, J. 2024,, https://www.eso.org/sci/facilities/alma/developmentstudies/20240703154158_20240703_FINAL_ESO_19-25417-HNE_REPORT-merged-1.pdf ESO
- Pardo, J., Cernicharo, J., & Serabyn, E. 2001, *IEEE Transactions on Antennas and Propagation*, 49, 1683, doi: [10.1109/8.982447](https://doi.org/10.1109/8.982447)
- Pardo, J. R. 2019, in *ALMA Development Workshop*, 36, doi: [10.5281/zenodo.3240379](https://doi.org/10.5281/zenodo.3240379)
- Park, J., Hada, K., Kino, M., et al. 2019, *ApJ*, 887, 147, doi: [10.3847/1538-4357/ab5584](https://doi.org/10.3847/1538-4357/ab5584)
- Pasetto, A., Carrasco-González, C., Gómez, J. L., et al. 2021, *ApJL*, 923, L5, doi: [10.3847/2041-8213/ac3a88](https://doi.org/10.3847/2041-8213/ac3a88)
- Pasini, T., Finoguenov, A., Brügggen, M., et al. 2021, *MNRAS*, 505, 2628, doi: [10.1093/mnras/stab1451](https://doi.org/10.1093/mnras/stab1451)
- Peng, C. Y., Ho, L. C., Impey, C. D., & Rix, H.-W. 2002, *AJ*, 124, 266, doi: [10.1086/340952](https://doi.org/10.1086/340952)
- Perlman, E. S., Sparks, W. B., Radomski, J., et al. 2001, *ApJL*, 561, L51, doi: [10.1086/324515](https://doi.org/10.1086/324515)
- Perlman, E. S., Mason, R. E., Packham, C., et al. 2007, *ApJ*, 663, 808, doi: [10.1086/518781](https://doi.org/10.1086/518781)

- Pickett, H. M., Poynter, R. L., Cohen, E. A., et al. 1998, *JQSRT*, 60, 883, doi: [10.1016/S0022-4073\(98\)00091-0](https://doi.org/10.1016/S0022-4073(98)00091-0)
- Pineda, J. L., Goldsmith, P. F., Chapman, N., et al. 2010, *ApJ*, 721, 686, doi: [10.1088/0004-637X/721/1/686](https://doi.org/10.1088/0004-637X/721/1/686)
- Planck Collaboration, Ade, P. A. R., Aghanim, N., et al. 2016, *A&A*, 594, A13, doi: [10.1051/0004-6361/201525830](https://doi.org/10.1051/0004-6361/201525830)
- Pogge, R. W., Maoz, D., Ho, L. C., & Eracleous, M. 2000, *ApJ*, 532, 323, doi: [10.1086/308567](https://doi.org/10.1086/308567)
- Porbital. 2024, <https://plotdigitizer.com>
- Prandoni, I., Laing, R. A., de Rutter, H. R., & Parma, P. 2010, *A&A*, 523, A38, doi: [10.1051/0004-6361/201015456](https://doi.org/10.1051/0004-6361/201015456)
- Prieto, M. A., Fernández-Ontiveros, J. A., Markoff, S., Espada, D., & González-Martín, O. 2016, *MNRAS*, 457, 3801, doi: [10.1093/mnras/stw166](https://doi.org/10.1093/mnras/stw166)
- Privon, G., et al. 2024, ALMA Proposer's Guide, ALMA Doc. 11.2, ver. 1.0, doi: [10.5281/zenodo.4511961](https://doi.org/10.5281/zenodo.4511961)
- Pulido, F. A., McNamara, B. R., Edge, A. C., et al. 2018, *ApJ*, 853, 177, doi: [10.3847/1538-4357/aaa54b](https://doi.org/10.3847/1538-4357/aaa54b)
- Rappenglück, B., Ackermann, L., Alvarez, S., et al. 2014, *Atmospheric Chemistry and Physics*, 14, 4909, doi: [10.5194/acp-14-4909-2014](https://doi.org/10.5194/acp-14-4909-2014)
- Reid, M. J., Biretta, J. A., Junor, W., Muxlow, T. W. B., & Spencer, R. E. 1989, *ApJ*, 336, 112, doi: [10.1086/166998](https://doi.org/10.1086/166998)
- Richards, A. M. S., Moravec, E., Etoke, S., et al. 2022, arXiv e-prints, arXiv:2207.05591, doi: [10.48550/arXiv.2207.05591](https://doi.org/10.48550/arXiv.2207.05591)
- Riffel, R. A., Storchi-Bergmann, T., Zakamska, N. L., & Riffel, R. 2020, *MNRAS*, 496, 4857, doi: [10.1093/mnras/staa1922](https://doi.org/10.1093/mnras/staa1922)
- Rivera-Ingraham, A., Ristorcelli, I., Juvela, M., et al. 2016, *A&A*, 591, A90, doi: [10.1051/0004-6361/201526263](https://doi.org/10.1051/0004-6361/201526263)
- Roman-Duval, J., Jackson, J. M., Heyer, M., Rathborne, J., & Simon, R. 2010, *ApJ*, 723, 492, doi: [10.1088/0004-637X/723/1/492](https://doi.org/10.1088/0004-637X/723/1/492)
- Rose, T., Edge, A. C., Combes, F., et al. 2019a, *MNRAS*, 489, 349, doi: [10.1093/mnras/stz2138](https://doi.org/10.1093/mnras/stz2138)
- Rose, T., Edge, A. C., Combes, F., et al. 2019b, *MNRAS*, 485, 229, doi: [10.1093/mnras/stz406](https://doi.org/10.1093/mnras/stz406)
- Rose, T., Edge, A. C., Combes, F., et al. 2020, *MNRAS*, 496, 364, doi: [10.1093/mnras/staa1474](https://doi.org/10.1093/mnras/staa1474)
- Rosolowsky, E., Hughes, A., Leroy, A. K., et al. 2021, *MNRAS*, 502, 1218, doi: [10.1093/mnras/stab085](https://doi.org/10.1093/mnras/stab085)
- Ruffa, I., Prandoni, I., Davis, T. A., et al. 2022, *MNRAS*, 510, 4485, doi: [10.1093/mnras/stab3541](https://doi.org/10.1093/mnras/stab3541)
- Ruffa, I., Prandoni, I., Laing, R. A., et al. 2019, *MNRAS*, 484, 4239, doi: [10.1093/mnras/stz255](https://doi.org/10.1093/mnras/stz255)
- Rugel, M. R., Beuther, H., Bühr, S., et al. 2018, *A&A*, 618, A159, doi: [10.1051/0004-6361/201731872](https://doi.org/10.1051/0004-6361/201731872)
- Ryon, J. E. 2022, in *ACS Instrument Handbook for Cycle 30 v. 21.0*, Vol. 21, 21
- Sabra, B. M., Shields, J. C., Ho, L. C., Barth, A. J., & Filippenko, A. V. 2003, *ApJ*, 584, 164, doi: [10.1086/345664](https://doi.org/10.1086/345664)
- Sadler, E. M., Ricci, R., Ekers, R. D., et al. 2008, *MNRAS*, 385, 1656, doi: [10.1111/j.1365-2966.2008.12955.x](https://doi.org/10.1111/j.1365-2966.2008.12955.x)
- Safraneck-Shrader, C., Krumholz, M. R., Kim, C.-G., et al. 2017, *MNRAS*, 465, 885, doi: [10.1093/mnras/stw2647](https://doi.org/10.1093/mnras/stw2647)
- Salomé, P., & Combes, F. 2003, *A&A*, 412, 657, doi: [10.1051/0004-6361:20031438](https://doi.org/10.1051/0004-6361:20031438)
- Salomé, P., & Combes, F. 2008, *A&A*, 489, 101, doi: [10.1051/0004-6361:200810262](https://doi.org/10.1051/0004-6361:200810262)
- Sancisi, R., Fraternali, F., Oosterloo, T., & van der Hulst, T. 2008, *A&A Rv*, 15, 189, doi: [10.1007/s00159-008-0010-0](https://doi.org/10.1007/s00159-008-0010-0)
- Sandstrom, K. M., Leroy, A. K., Walter, F., et al. 2013, *ApJ*, 777, 5, doi: [10.1088/0004-637X/777/1/5](https://doi.org/10.1088/0004-637X/777/1/5)
- Sankrit, R., Sembach, K. R., & Canizares, C. R. 1999, *ApJ*, 527, 733, doi: [10.1086/308115](https://doi.org/10.1086/308115)
- Saripalli, L. 2012, *AJ*, 144, 85, doi: [10.1088/0004-6256/144/3/85](https://doi.org/10.1088/0004-6256/144/3/85)
- Scoville, N. Z. 2013, in *Secular Evolution of Galaxies*, ed. J. Falcón-Barroso & J. H. Knapen (Cambridge University Press), 491, doi: [10.48550/arXiv.1210.6990](https://doi.org/10.48550/arXiv.1210.6990)
- Shangguan, J., Ho, L. C., Bauer, F. E., Wang, R., & Treister, E. 2020, *ApJS*, 247, 15, doi: [10.3847/1538-4365/ab5db2](https://doi.org/10.3847/1538-4365/ab5db2)
- Shetty, R., Beaumont, C. N., Burton, M. G., Kelly, B. C., & Klessen, R. S. 2012, *MNRAS*, 425, 720, doi: [10.1111/j.1365-2966.2012.21588.x](https://doi.org/10.1111/j.1365-2966.2012.21588.x)
- Shibata, R., Matsushita, K., Yamasaki, N. Y., et al. 2001, *ApJ*, 549, 228, doi: [10.1086/319075](https://doi.org/10.1086/319075)
- Simionescu, A., Tremblay, G., Werner, N., et al. 2018, *MNRAS*, 475, 3004, doi: [10.1093/mnras/sty047](https://doi.org/10.1093/mnras/sty047)
- Simon, D. A., Cappellari, M., & Hartke, J. 2024, *MNRAS*, 527, 2341, doi: [10.1093/mnras/stad3309](https://doi.org/10.1093/mnras/stad3309)
- Smith, M. D., Bureau, M., Davis, T. A., et al. 2021, *MNRAS*, 500, 1933, doi: [10.1093/mnras/staa3274](https://doi.org/10.1093/mnras/staa3274)
- Snow, T. P., & McCall, B. J. 2006, *ARA&A*, 44, 367, doi: [10.1146/annurev.astro.43.072103.150624](https://doi.org/10.1146/annurev.astro.43.072103.150624)
- Sofia, U. J., Lauroesch, J. T., Meyer, D. M., & Cartledge, S. I. B. 2004, *ApJ*, 605, 272, doi: [10.1086/382592](https://doi.org/10.1086/382592)
- Solomon, P. M., Rivolo, A. R., Barrett, J., & Yahil, A. 1987, *ApJ*, 319, 730, doi: [10.1086/165493](https://doi.org/10.1086/165493)
- Sparks, W. B., Donahue, M., Jordán, A., Ferrarese, L., & Côté, P. 2004, *ApJ*, 607, 294, doi: [10.1086/383189](https://doi.org/10.1086/383189)
- Sparks, W. B., Ford, H. C., & Kinney, A. L. 1993, *ApJ*, 413, 531, doi: [10.1086/173022](https://doi.org/10.1086/173022)
- Stone, M., Veilleux, S., Meléndez, M., et al. 2016, *ApJ*, 826, 111, doi: [10.3847/0004-637X/826/2/111](https://doi.org/10.3847/0004-637X/826/2/111)
- Tadhunter, C. 2008, *NewAR*, 52, 227, doi: [10.1016/j.newar.2008.06.004](https://doi.org/10.1016/j.newar.2008.06.004)
- Tan, J. C., Beuther, H., Walter, F., & Blackman, E. G. 2008, *ApJ*, 689, 775, doi: [10.1086/592592](https://doi.org/10.1086/592592)
- Taylor, T. R., Chao, C.-T., & Chiou, J.-S. 2020, *Applied Sciences*, 10, doi: [10.3390/app10113952](https://doi.org/10.3390/app10113952)

- Temì, P., Amblard, A., Gitti, M., et al. 2018, *ApJ*, 858, 17, doi: [10.3847/1538-4357/aab9b0](https://doi.org/10.3847/1538-4357/aab9b0)
- Tremblay, G. R., Combes, F., Oonk, J. B. R., et al. 2018, *ApJ*, 865, 13, doi: [10.3847/1538-4357/aad6dd](https://doi.org/10.3847/1538-4357/aad6dd)
- Trump, J. R., Impey, C. D., Kelly, B. C., et al. 2011, *ApJ*, 733, 60, doi: [10.1088/0004-637X/733/1/60](https://doi.org/10.1088/0004-637X/733/1/60)
- Tsukui, T., Iguchi, S., Mitsuhashi, I., & Tadaki, K. 2023, *Journal of Astronomical Telescopes, Instruments, and Systems*, 9, 018001, doi: [10.1117/1.JATIS.9.1.018001](https://doi.org/10.1117/1.JATIS.9.1.018001)
- Tsvetanov, Z. I., Allen, M. G., Ford, H. C., & Harms, R. J. 1999a, in *The Radio Galaxy Messier 87*, ed. H.-J. Röser & K. Meisenheimer, Vol. 530, 301, doi: [10.1007/BFb0106441](https://doi.org/10.1007/BFb0106441)
- Tsvetanov, Z. I., Hartig, G. F., Ford, H. C., et al. 1999b, in *The Radio Galaxy Messier 87*, ed. H.-J. Röser & K. Meisenheimer, Vol. 530, 307, doi: [10.1007/BFb0106442](https://doi.org/10.1007/BFb0106442)
- Usero, A., et al. 2019,
- Utomo, D., Blitz, L., Davis, T., et al. 2015, *ApJ*, 803, 16, doi: [10.1088/0004-637X/803/1/16](https://doi.org/10.1088/0004-637X/803/1/16)
- van der Tak, F. F. S., Black, J. H., Schöier, F. L., Jansen, D. J., & van Dishoeck, E. F. 2007, *A&A*, 468, 627, doi: [10.1051/0004-6361:20066820](https://doi.org/10.1051/0004-6361:20066820)
- Veilleux, S., Meléndez, M., Sturm, E., et al. 2013, *ApJ*, 776, 27, doi: [10.1088/0004-637X/776/1/27](https://doi.org/10.1088/0004-637X/776/1/27)
- Viaene, S., Sarzi, M., Baes, M., Fritz, J., & Puerari, I. 2017, *MNRAS*, 472, 1286, doi: [10.1093/mnras/stx1781](https://doi.org/10.1093/mnras/stx1781)
- Walker, R. C., Hardee, P. E., Davies, F. B., Ly, C., & Junor, W. 2018, *ApJ*, 855, 128, doi: [10.3847/1538-4357/aaafcc](https://doi.org/10.3847/1538-4357/aaafcc)
- Walsh, J. L., Barth, A. J., Ho, L. C., & Sarzi, M. 2013, *ApJ*, 770, 86, doi: [10.1088/0004-637X/770/2/86](https://doi.org/10.1088/0004-637X/770/2/86)
- Wilson, A. S., & Yang, Y. 2002, *ApJ*, 568, 133, doi: [10.1086/338887](https://doi.org/10.1086/338887)
- Wong, T., Oudshoorn, L., Sofovich, E., et al. 2022, *ApJ*, 932, 47, doi: [10.3847/1538-4357/ac723a](https://doi.org/10.3847/1538-4357/ac723a)
- Yuan, F., & Narayan, R. 2014, *ARA&A*, 52, 529, doi: [10.1146/annurev-astro-082812-141003](https://doi.org/10.1146/annurev-astro-082812-141003)
- Yusef-Zadeh, F., Arendt, R. G., Wardle, M., et al. 2022, *ApJL*, 925, L18, doi: [10.3847/2041-8213/ac4802](https://doi.org/10.3847/2041-8213/ac4802)
- Zhang, H.-M., Wang, Z.-J., Zhang, J., et al. 2020, *PASJ*, 72, 44, doi: [10.1093/pasj/psaa029](https://doi.org/10.1093/pasj/psaa029)
- Zhang, Q., Ye, J., Zhang, S., & Han, F. 2018, *Journal of Sensors*, 2018, 4909, doi: [10.1155/2018/3428303](https://doi.org/10.1155/2018/3428303)